

Development and Characterization of Graphene-based Microporous Layers for Proton Exchange Membrane Fuel Cells

by

Adnan Ozden

A thesis
presented to the University of Waterloo
in fulfillment of the
thesis requirement for the degree of
Master of Applied Science
in
Mechanical and Mechatronics Engineering

Waterloo, Ontario, Canada, 2018

© Adnan Ozden 2018

I hereby declare that I am the sole author of this thesis. This is a true copy of the thesis, including any required final revisions, as accepted by my examiners.

I understand that my thesis may be made electronically available to the public.

Abstract

Proton exchange membrane (PEM) fuel cell is an energy-conversion device that converts the chemical energy of hydrogen and oxygen into electricity directly through electrochemical reactions with only water and heat as reaction by-products. Over the last decade, PEM fuel cell technology has been considerably advanced, with remaining technical and scientific challenges to be overcome for further improvements in performance, durability, stability, and cost. For example, specifically for end-use applications, fuel cell system is equipped with an external humidifier to ensure an adequate level of humidification for the membrane-electrode assembly (MEA). However, such a humidification methodology not only increases the weight, complexity, and manufacturing cost of the fuel cell system, but also substantially reduces its overall energy-conversion efficiency through increased parasitic power consumption. Thus, if an adequate level of humidification could be met without using an external humidifier, then the eventual system cost, weight, and complexity could be reduced substantially, and such an improvement would certainly pave the way towards the widespread commercialization of this technology.

Such a target could be achieved through a well-designed MEA architecture, which can maintain sufficient humidification, regardless of operating conditions. In this context, as a key component in the management of water (and to a lesser degree, heat) for improved performance, stability, and durability of PEM fuel cells under a wide range of operating conditions, microporous layer (MPL) should be designed to ensure self-humidification for the MEA. In recent years, the criticality of MPLs to water management has

been progressively recognized, which further confirmed through promising cell performance characteristics obtained from the laboratory-scale investigations. However, further improvement requires further breakthroughs, particularly in the development and implementation of alternative MPL materials. The performance of MPLs depends to a large extent on their morphological, microstructural, physical, and electrochemical characteristics, which are, in turn, governed by the specifications of their materials, typically a carbon or carbon-derived powder and a polymeric binder. Owing to their favorable features, i.e., high electrical and thermal conductivity, high corrosion resistance, and wide availability and hence affordability, various types of carbon-based materials, such as Vulcan[®] XC-72R, Ketjenblack[®] EC-300J, Ketjenblack[®] EC-600JD, Black Pearls[®] 2000, and Hicon Black[®], have been employed as primary MPL materials, albeit with their widely known drawbacks in terms of morphological degradation during continuous cell operation. In addition, MPLs made of these conventional carbon powders can only provide promising performance under a very limited range of operating conditions, which is not fully satisfactory for practical applications.

As an alternative to conventional carbon/carbon-derived materials, graphene, a monolayer of carbon atoms arranged in a two-dimensional (2D) lattice, would be an appealing material, due to its unique characteristics, including extremely high single-particle electrical conductivity, high thermal conductivity, high surface area, and high mechanical stiffness and elasticity, and many others. Graphene flakes are also prone to stack horizontally and built up a well-connected and smooth layer. Thus, placement of such a compact and smooth layer between the catalyst layer (CL) and the gas

diffusion layer (GDL) could reasonably boost the catalyst utilization (by preventing migration of precious catalyst nanoparticles into the GDL), improve interfacial characteristics, and facilitate heat transport in the in- and through-plane directions. In this thesis, graphene is therefore considered to be an alternative MPL material. Accordingly, graphene-based MPLs are prepared and characterized through morphological, microstructural, physical, and electrochemical characterizations to reveal many of their unexplored characteristics. Cell performances of the graphene-based MPLs are also investigated for the first time in a scaled-up PEM fuel cell. Comparison studies are conducted with an MPL made of an extensively used commercial carbon-based material, Ketjenblack.

The results indicate that the graphene-based MPL has a unique morphology composed of firmly and horizontally packaged graphene flakes that substantially improves water management, electron transport, catalyst activity and catalyst utilization. Due to such a desirable morphology, the graphene-based MPL demonstrates comparable performance to the one made of Ketjenblack under high-humidity operation, while exhibits excellent performance superiorities (up to a peak power density of about 53% better than the conventional carbon-based MPL (Ketjenblack)), specifically under low- and intermediate-humidity operation. Overall, the graphene-based MPL is found to have a significant potential to meet the performance demand under low-, intermediate-, and high-humidity conditions, thereby potentially eliminating the dependence of PEM fuel cells on external humidifiers.

Acknowledgements

I would like to express my gratitude to my co-supervisors, Dr. Feridun Hamdullahpur and Dr. Xianguo Li, for their excellent guidance, encouragement, and support throughout my MAsc degree. I would like to also thank my committee members, Dr. John Wen and Dr. Zhongchao Tan, for taking their time to review my thesis and for providing constructive comments. Their comments are highly appreciated.

A sincere thank to Dr. Samaneh Shahgaldi for the countless hours we spent discussing possible solutions to problems arising from fabrication and characterization of microporous layers. Further, I would like to thank Jian Zhao for making himself available to discuss issues, particularly arising from pore size distribution and gas permeability measurements.

Furthermore, I would like to gratefully acknowledge the financial support of the Ontario-China Research and Innovation Fund (OCRIF Round 3) and the Natural Sciences and Engineering Research Council of Canada (NSERC) through a Discovery Grant. Lastly, I would like to express my gratitude to Group NanoXplore Inc. for the supply of graphene investigated in this thesis.

List of Contents

List of Tables	x
List of Figures	xi
Nomenclature	xvi
1. Introduction	1
1.1. PEM Fuel Cell Components and Working Principle	2
1.2. PEM Fuel Cell Performance.....	6
1.3. Structure of the Gas Diffusion Layer	9
1.3.1. The Macroporous Substrate	10
1.3.2. The Microporous Layer.....	13
1.4. Scope and Outline of Thesis	18
2. Characteristics of the Gas Diffusion Layers	22
2.1. Characteristics of GDLs.....	23
2.1.1. Porosity and Pore Size Distribution.....	24
2.1.2. Electrical Conductivity.....	28

2.1.3. Gas Permeability	32
2.1.4. Surface Wettability	33
3. Literature Review	37
3.1. Design parameters of GDLs	38
3.1.1. Effect of type and loading of carbon black powder.....	41
3.1.2. Effect of microporous layer thickness.....	44
3.1.3. Effect of hydrophobic and hydrophilic treatment	44
3.1.4. Effect of microstructure modification	45
3.1.5. Microporous layer fabrication process	46
4. Characterization Techniques	48
4.1. Ex-situ Characterization of GDLs.....	48
4.1.1. Porosity and Pore Size Distribution	49
4.1.2. Electrical Conductivity.....	54
4.1.3. Gas Permeability	59
4.1.4. Surface Wettability	61
4.2. In-situ Characterization of GDLs.....	62
4.2.1. PEM Fuel Cell Performance Analysis	63
4.2.2. Electrochemical analysis	65
5. Results and Discussion	67
5.1. Physical analysis of carbon powders	67
5.2. Morphological and microstructural analyses of double-layer GDLs.....	70

5.2.1. Scanning electron microscopy analysis	70
5.2.2. Porosimetry analysis	72
5.3. Physical analysis of double-layer GDLs	78
5.3.1. Air permeability	78
5.3.2. Surface Wettability	79
5.3.3. In-plane electrical resistivity	81
5.4. Electrochemical analysis of double-layer GDLs.....	83
5.4.1. Cyclic Voltammetry	83
5.5. Single-cell performance analyses of double-layer GDLs	85
6. Conclusions and Recommendations	93
6.1. Conclusions.....	93
6.2. Recommendations.....	96
7. References	98

List of Tables

3.1	A summary of main characteristics of GDLs, design parameters affecting GDL characteristics, and the potential effects of GDL characteristics on fuel cell performance	40
3.2	A summary of specifications for both the different carbon powders and the double-layer GDLs having these carbon powders in their MPLs	43
5.1	Pore characteristics of the macroporous substrate (MPS, Avcarb EP 40, without MPL) and double-layer GDLs based on either graphene or Ketjenblack MPL	77
5.2	Physical characteristics of the double-layer GDLs based on either graphene or Ketjenblack MPL	82

List of Figures

1.1 A schematic of a proton exchange membrane (PEM) fuel cell and its operating principle, as adopted from [4]. CFFP: cathode flow-field plate; CFF: cathode flow field; CGDL: cathode gas diffusion layer; CMPL: cathode microporous layer; CCL: cathode catalyst layer; EM: electrolyte membrane; ACL: anode catalyst layer; AMPL: anode microporous layer; AGDL: anode gas diffusion layer; AFF: anode flow field; AFFP: anode flow-field plate	5
1.2 A typical polarization curve for a proton exchange membrane (PEM) fuel cell	8
1.3 Scanning electron microscopy (SEM) images of the macroporous substrate (MPS) with and without hydrophobic agent treatment: (a) surface morphology of the MPS without hydrophobic agent treatment, the image showing the macro-scale open pores and orientation of the carbon fibres; (b) surface morphology of the MPS with hydrophobic agent treatment, the image showing the macro-scale open pores and the network built up by the hydrophobic agent, specifically in the regions near the surface	13
1.4 A schematic of water transport in a proton exchange membrane (PEM) fuel cell.....	14

1.5 Scanning electron microscopy (SEM) image of the gas diffusion layer (GDL) (macroporous substrate (MPS) + microporous layer (MPL)): surface morphology of the double-layer GDL, the image showing the homogeneous, smooth, compact, and porous surface characteristics of the double-layer GDL	15
1.6 Illustrations of (a) wrapping up of graphene into a zero-dimensional (0D) buckyball, (b) rolling of graphene into a one-dimensional (1D) nanotube, and (c) stacking of graphene into three-dimensional (3D) graphite	19
2.1 Cumulative pore size distribution in the macroporous substrate (MPS) and GDL (MPS + microporous layer (MPL)). r: pore radius; MPS: Avcarb EP40 carbon paper without hydrophobic treatment; GDL (MPS + MPL): Vulcan based MPL deposited onto the MPS (Avcarb EP40); Micropores: pores smaller than 0.07 μm ; Mesopores: pores in the range of 0.07-5 μm ; Macropores: pores larger than 5 μm	26
2.2 Schematics of (a) static contact angle (θ_c) measurements on hydrophilic ($\theta_c < 90^\circ$) and hydrophobic ($\theta_c > 90^\circ$) surfaces and (b) sliding contact angle (θ_s)	35
3.1 A procedure followed to deposit the graphene-based MPL onto the macroporous substrate (MPS)	47
4.1 A schematic of the procedure to determine the capillary pressure curve of the gas diffusion layers (GDLs) through the method of standard porosimetry (MSP).....	52
4.2 A schematic of the experimental setup employed to determine the in-plane electrical conductivity of gas diffusion layers (GDLs)	56

4.3 A schematic of the experimental setup employed to determine the through-plane electrical conductivity of gas diffusion layers (GDLs).....	58
4.4 A schematic of the experimental setup employed to determine the through-plane gas permeability of gas diffusion layers (GDLs)	60
4.5 A schematic of the fuel cell test station and its components	64
5.1 Pore size distribution of graphene and Ketjenblack® EC-600JD powders: (a) Cumulative pore volume distributions and (b) Differential pore volume distributions	69
5.2 Scanning electron microscopy (SEM) images of gas diffusion layers (GDLs): (a) top view of the macroporous substrate (MPS) (EP 40 Raw GDL, without microporous layer (MPL)), the image showing the macro-scale pores and interconnected network built up by the carbon fibers; (b) cross-sectional view of the MPS (EP 40 Raw GDL, without MPL); (c) top view of the double-layer GDL based on graphene MPL, the image showing the firmly and horizontally packaged graphene flakes; (d) cross-sectional view of the double-layer GDL based on graphene MPL, the image showing the graphene flakes penetrated into the MPS (EP 40 Raw GDL); (e) top view of the double-layer GDL based on Ketjenblack EC-600JD MPL, the image showing the interconnected and macro-scale surface cracks; (f) cross-sectional view of the double-layer GDL based on Ketjenblack EC-600JD MPL, the image showing the highly compact and composite-like cross-sectional morphology	71
5.3 (a) Cumulative and (b) Differential pore size distribution in the macroporous substrate (MPS) (EP 40 Raw GDL, without microporous layer (MPL)) and double-layer GDLs based on either graphene or Ketjenblack MPL.	

V_p denotes the pore volume; V_b represents the bulk volume; d is the pore diameter in nm; and r is the pore radius in nm	75
5.4 Static contact angles measured from the surfaces of (a) graphene microporous layer (MPL) and (b) Ketjenblack MPL	79
5.5 Cyclic voltammograms (CVs) for the membrane-electrode assemblies (MEAs) based on either graphene microporous layer (MPL) or Ketjenblack MPL. Operating temperature: 75°C; nitrogen and hydrogen back pressures: 35 kPag; and nitrogen and hydrogen relative humidity of 100%	84
5.6 Polarization curves obtained from the membrane-electrode assemblies (MEAs) either with the (a) graphene MPL or (b) Ketjenblack MPL under various relative humidities of air and hydrogen streams. Operating temperature: 75°C, hydrogen and air back pressures: 35 kPag, and hydrogen and air flow rates: 4.45 and 9.00 l/min	87
5.7 Peak power densities obtained from the membrane-electrode assemblies (MEAs) either with the graphene microporous layer (MPL) or Ketjenblack MPL under various relative humidities (RHs) of air and hydrogen streams. Operating temperature: 75°C, hydrogen and air back pressures: 35 kPag, and hydrogen and air flow rates: 4.45 and 9.00 l/min	88
5.8 Polarization curve obtained from the membrane-electrode assemblies (MEAs) either with the (a) graphene microporous layer (MPL) or (b) Ketjenblack MPL under various back pressures of air and hydrogen streams. Operating temperature: 75°C, relative humidities (RHs) of air and hydrogen streams: 100%, and flow rates of hydrogen and air streams: 4.45 and 9.00 l/min	90

5.9 Peak power densities obtained from the membrane-electrode assemblies (MEAs) either with the graphene microporous layer (MPL) or Ketjenblack MPL under various back pressures of air and hydrogen air streams. Operating temperature: 75°C, air and hydrogen relative humidities of 100%, and hydrogen and air flow rates of 4.45 and 9.00 l/min 92

Nomenclature

<i>A</i>	Area (m^2)
<i>b</i>	Bulk properties
<i>C</i>	Concentration
<i>D</i>	Diffusion coefficient of species (m^2/s)
<i>d</i>	Diameter (m)
<i>E</i>	Voltage (<i>Volt</i>)
<i>J</i>	Electrical current density (A/cm^2)
<i>j</i>	Mass rate of diffusion
<i>k</i>	Boltzmann's constant = $1,3807 \times 10^{-23}$ (J/K)
<i>l</i>	Thickness
<i>m</i>	Mass (g)
N_A	Avogadro number = $6,022 \times 10^{23}$ (/mol)
<i>p</i>	Pressure (<i>Pa</i>)
<i>R</i>	Resistance
R_u	The universal gas constant = 8.314×10^{-3} kJ/(mol.K)
<i>r</i>	Radius (m)
<i>RH</i>	Relative humidity
<i>T</i>	Temperature (K)
<i>t</i>	Time (s)
<i>u</i>	Uncertainty
<i>V</i>	Volume (m^3)

Abbreviation

ACL	Anode catalyst layer
AFC	Alkaline fuel cell
AFF	Anode flow field
AFFP	Anode flow-field plate
AFM	Atomic force microscopy
CCL	Cathode catalyst layer
CCM	Catalyst coated on membrane
CCS	Catalyst coated on substrate (i.e. GDL)
CFF	Cathode flow field
CFFP	Cathode flow-field plate
CL	Catalyst layer
DMFC	Direct methanol fuel cell
DOE	U.S. Department of Energy
DTM	Decal transfer method
ECSA	Electrochemical surface area
ERR	Electrochemical reaction region
FEP	Fluorinated ethylene propylene
FFP	Flow-field plate
GDL	Gas diffusion layer
HOR	Hydrogen oxidation reaction
IPA	Isopropyl alcohol
MCFC	Molten carbonate fuel cell
MEA	Membrane-electrode assembly
MPL	Microporous layer
MPS	Macroporous substrate
MSP	Method of Standard Porosimetry
OCV	Open circuit voltage
ORR	Oxygen reduction reaction

PAFC	Phosphoric acid fuel cell
PDMS	Polydimethylsiloxane
PEM	Polymer electrolyte membrane
PEMFC	Proton exchange membrane fuel cell
PFPE	Perfluoropolyether
PSD	Pore size distribution
PTFE	Polytetrafluoroethylene
PVA	Polyvinyl alcohol
PVDF	Polyvinylidene fluoride
RH	Relative humidity
RMS	Root mean square
RSS	Root sum square
SEM	Scanning electron microscopy
TPB	Three phase boundary

Greek letter

ρ	Density
Φ	Porosity
ϕ	Capillary potential
ε	Diffusibility
σ	Surface tension
τ	Tortuosity
η	Efficiency
θ	Contact angle
δ	Thickness

Subscript and superscript

eff	Effective property
-----	--------------------

bulk	Bulk property
Kn	Knudsen
eq	Equivalent
r	Reversible condition
th	Thermo-neutral
sub	Substrate property

Chapter 1

Introduction

The over-consumption and limited availability of conventional energy sources, ever-growing supply-demand gap with the increase in human population, and technological inventions and emerging concerns on environmental issues (i.e., global warming and air and water pollution) have made development and successful implementation of eco-friendly alternative technologies more critical than ever [1,2]. Thus, a large variety of fossil fuel independent energy sources, such as solar, wind, geothermal, biomass and hydro-based technologies and fuel cells, have been developed and introduced successfully into the market to address these critical concerns in an economically efficient and socially acceptable manner [3]. Among these technologies, fuel cells, as the energy-conversion devices for direct and efficient conversion of the chemical energy of hydrogen and oxygen into electricity, are now on the verge of becoming a promising candidate for transportation, stationary, and portable applications [4,5].

Fuel cells are categorized primarily according to the features of their employed electrolyte and consumed fuel. The primary fuel cell types are proton exchange membrane (PEM) fuel cells, solid oxide fuel cells (SOFCs), alkaline fuel cells (AFCs), molten carbonate fuel cells (MCFCs), and phosphoric acid fuel cells (PAFCs) [4,6]. Of these types, in particular PEM fuel cells have received significant attention and considered as an up-and-coming power source. This popularity arises from their favorable characteristics, such as high energy-conversion efficiency, rapid start-up capability, the ability to operate without moving constituents, simple design, quiet operation, relatively low operating temperatures, fast response to dynamic loads, and minimal to zero emissions [7].

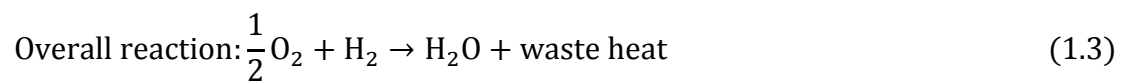
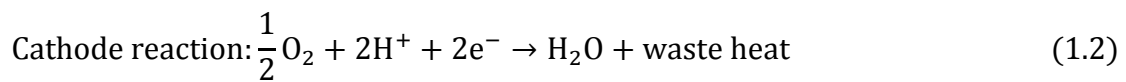
Currently, PEM fuel cells have reached the early stage of commercialization, along with certain technical and scientific technical barriers to be overcome for further improvements in performance, durability, stability, reliability, and cost reduction, and these challenges are the main motivation of the current research efforts in the fuel cell community [5].

1.1. PEM Fuel Cell Components and Working Principle

A PEM fuel cell is an electrochemical device that generates electrical energy through direct conversion of the chemical energy of hydrogen and oxygen into electricity [8]. A fuel cell has a multi-layered architecture and is composed of anode and cathode flow-field plates (AFFP and CFFP, respectively) and a membrane-electrode assembly (MEA), as schematically presented in Fig. 1.1 [9]. The AFFP and CFFP are mainly responsible for distributing hydrogen and oxygen over the respective surfaces of the gas diffusion layers (GDLs) through flow channels. The MEA is the core

component of a fuel cell system and mainly comprised of anode and cathode GDLs as well as catalyst layers (CLs), and the anode and cathode electrodes are being separated by a proton-conducting (and electron insulator) layer, known as “membrane” [10]. The membrane is mainly responsible for transport of protons from the anode to the cathode, in addition to acting as a barrier that inhibits reactant and by-product species other than protons from reaching the cathode electrode. The CL is composed of electrochemically active nanoparticles (typically platinum (Pt)) supported on relatively larger carbon or graphite particles [11], all surrounded by ionomer films to create an environment, in which electrons, protons, reactants, as well as by-products are effectively transported [12].

In fuel cell operation, hydrogen and oxygen with certain level of humidification are distributed throughout the anode and cathode GDLs via the anode and cathode flow fields (AFF and CFF, respectively). With the joint effect of diffusion and relatively a lesser degree of convection, hydrogen and oxygen gases are transported through the anode and cathode GDLs, respectively, then diffuse into the anode and cathode catalyst layers (ACL and CCL, respectively) where the hydrogen oxidation reaction (HOR) and oxygen reduction reaction (ORR) take place [10]. The anode, cathode and overall reactions are given below [13]:



The electrons produced consecutively travel through the catalyst nanoparticles existing in the ACL, anode GDL, and AFFP to reach the external circuit. Then, the electrons flow back to the cell through the CFFP and the cathode GDL, and finally reaching the catalyst nanoparticles in the CCL [10]. On the other hand, the protons successively travel through the ionomer embedded in the ACL, electrolyte membrane, and the ionomer surrounding the catalyst nanoparticles in the CCL [10]. While the protons travel through the electrolyte membrane, they also carry water molecules along with them – a mechanism referred to as electro-osmotic drag [14]. The water, either formed as a by-product of the ORR or carried by the protons, is then consecutively absorbed into the ionomer, diffused through the pores available in the CCL, transported through the void region of the cathode GDL, and finally removed from the cell via cathode flow channels [10]. However, a certain portion of the water existing at the membrane/CCL interface is likely to diffuse from the cathode to the anode, due to the hydraulic pressure built up at the interface – a phenomenon known as “back diffusion” [15]. This phenomenon occurs because of the presence of microporous layer (MPL).

Heat is another by-product generated as a result of continuous electrochemical reactions and associated irreversibilities [10]. The heat generated spreads through the cell components under the dominant effect of conduction, alongside slight contribution coming from convection and radiation, in particular through the void regions; such a heat transport mechanism unavoidably leads to a considerable temperature gradient across the cell [16,17]. The heat built up within the cell is primarily removed via the humidified reactant supplied from the flow channels. The current state-of-the-art fuel cells are typically made of perfluorosulfonic acid membranes, through

which proton transport is governed by “Vehicular” and “Grotthus” mechanisms – which function well in the presence of adequate water [14,18]. The availability of adequate water inside the cell is therefore of paramount importance. However, excess water accumulating inside the cell leads to severe deterioration in performance by preventing transport of reactants and by-products to the electrochemical reaction regions (ERRs) [19]. Establishing an effective balance between the rate of water generation and water removal is therefore quite critical [20].

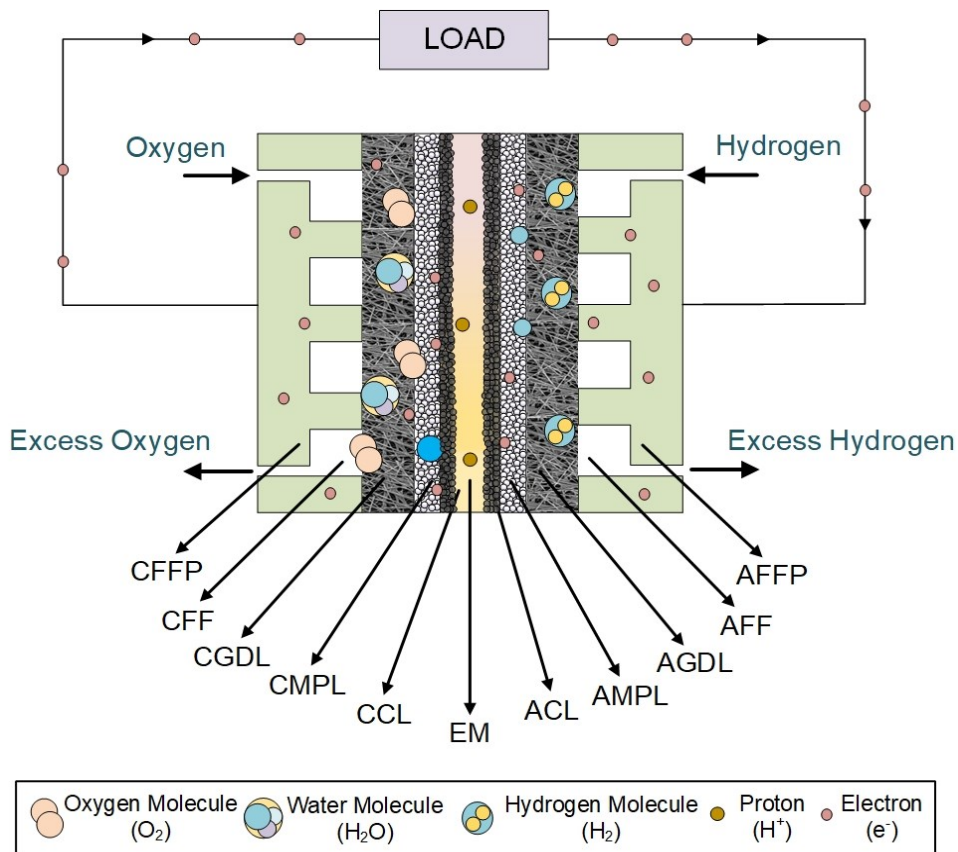


Figure 1.1: A schematic of a proton exchange membrane (PEM) fuel cell and its operating principle, as adopted from [9]. CFFP: cathode flow-field plate; CFF: cathode flow field; CGDL: cathode gas diffusion layer; CMPL: cathode

microporous layer; CCL: cathode catalyst layer; EM: electrolyte membrane; ACL: anode catalyst layer; AMPL: anode microporous layer; AGDL: anode gas diffusion layer; AFF: anode flow field; AFFP: anode flow-field plate.

1.2. PEM Fuel Cell Performance

In an operating PEM fuel cell, the cathode electrode is known to have a higher potential than the anode electrode, and the electrical potential difference between the anode and cathode electrodes is referred to as actual cell potential [21]. For a PEM fuel cell operating under standard conditions and fed with pure hydrogen and oxygen from its anode and cathode electrodes, respectively, the best possible cell potential is 1.22 V – which is also known as reversible cell voltage, because the best possible cell potential can only be achieved, if the cell is operated under thermodynamically reversible conditions [21]. However, under actual operation conditions, as a result of continuous electrochemical reactions and related irreversibilities, a fuel cell always faces energy losses, reflecting as electric potential losses [21]. These potential losses are generally referred to as “overpotential” and induce a noticeable reduction in cell potential, such that the cell potential can reduce down to 0.70 V for the case, at which the potential difference between the anode and cathode is maximum [21].

As current is started to drawn from the cell, the potential difference tends to gradually further decrease, due to the antagonistic relationship between the energy-conversion efficiency and high-current density operation [21]. A better understanding of this phenomenon can be gained by taking a close look at a typical polarization curve – a plot of the correlation between the cell voltage and current density [21]. As illustrated in Fig. 1.2, the polarization curve can

be categorized into three different regions, namely: activation overpotential, ohmic overpotential, and concentration overpotential [21]. These regions are basically identified according to the dominant transport phenomenon in a certain voltage range, although all the transport mechanisms are virtually active in a wide range of cell voltages [10].

As clearly seen from Fig. 1.2, as the cell current density increases, the cell voltage significantly decreases, which is largely related to the increasing contributions coming from the ohmic and concentration overpotentials. The activation, ohmic, and concentration overpotentials represent the voltage losses arising, respectively, from the resistance to the proceeding of the electrochemical reactions, to the transport of protons through the ionomer and membrane and electrons through the anode and cathode electrodes and other cell constituents, i.e., AFFP and CFFP, and to the mass transport of the reactants to the platforms where the electrochemical reactions take place [21].

The research interests in the field are therefore focusing on developing sound strategies to minimize these three polarizations through (i) development of highly active catalyst to accelerate the sluggish electrochemical reactions (hence reduce the activation polarization), (ii) development of alternative materials and cell architectures to minimize ionic and electrical resistance (hence reduce the ohmic polarization), and (iii) development of materials and designs for fuel cells to achieve more effective mass transport [21]. Even though minimizing the activation and ohmic polarizations is critical for further performance improvements, the largest voltage loss, as is clear from Fig. 1.2, is seen in the concentration polarization dominated region of the polarization curve, implying that the sluggish rate of

the ORR and mass transport is the major contributing factor to the overall voltage losses [21].

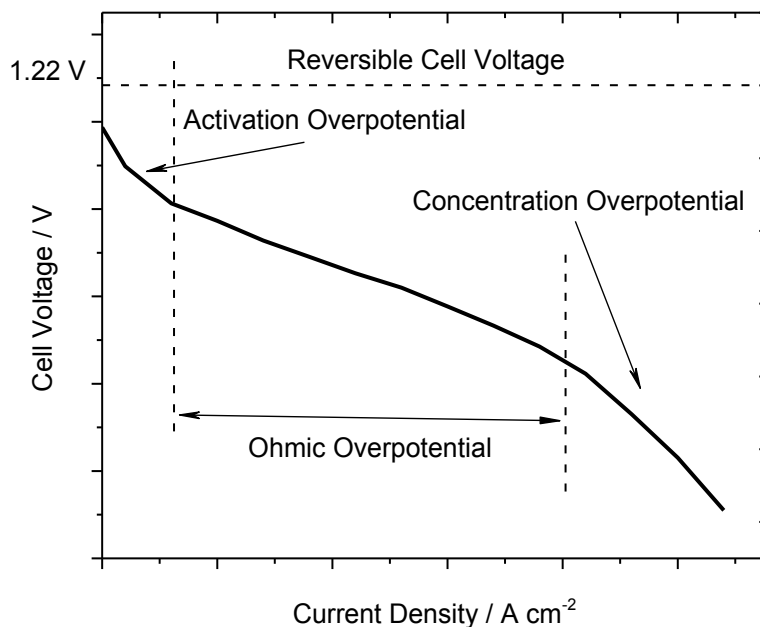


Figure 1.2: A typical polarization curve for a proton exchange membrane (PEM) fuel cell [21].

In particular, in recent years, the center of the many research interests is therefore optimization of the transport properties in the cell constituents, to mitigate the performance losses arising from the mass transport limitations, which certainly requires optimization of the transport properties of the porous cell constituents [8]. Making fuel cells completely suitable for high-current density operation is difficult task, but essential one to manufacture more cost-effective, smaller, and lighter ones for a given power requirement or for a particular application [21]. In this context, the importance of the GDL, as a key constituent that plays multifaceted roles in mass, heat, and electricity transport, has been increasingly recognized [22,23].

1.3. Structure of the Gas Diffusion Layer

The GDL is typically a carbon-based and water-proofed product and employed between the CLs and flow-field plates (FFPs), and hence it plays crucial roles in cell operation by (i) controlling both the transport of the reactants and by-products to and from the CLs, (ii) providing pathways between the CLs and FFPs for electron conduction, (iii) maintaining a delicate balance between membrane hydration and water removal, thus offering an acceptable heat and water management, and (iv) reinforcing the mechanically sensitive CL [24,25]. During cell operation, the liquid and gas species travel through the void region of the GDL, while the electrons, which are generated in the ACL and transported to the cathode by the means of an external circuit, are carried through the solid region [25]. In particular, the solid region serves as a bridge by providing pathways for electrons and heat [25]. An ideal GDL should fulfill the following requirements to be able to function properly during cell operation [26–28]:

- Have adequate porosity to allow the transport of both the reactant gases and by-products that transport in the opposite directions.
- Guarantee balanced hydrophobicity (water expulsion) and hydrophilicity (water retention).
- Ensure acceptable electrical and thermal conductivities in the in- and through-plane directions.
- Maintain a crack-free morphology over long-term operation.
- Provide optimum mechanical integrity to support delicate CL during cell operation.

- Ensure smooth transition between the CLs and FFPs, and hence provide as small as possible thermal and electrical resistance.
- Offer acceptable thermal and chemical resistance along with adequate durability.

Up to now, unfortunately, no single material has successfully satisfied all these requirements, thereby the GDL is typically made of two separate layers: a macroporous substrate (MPS) and an MPL [29]. The GDLs composed of two sub-layers, MPS and MPL, are generally referred to as “double- or dual-layer GDLs” [29,30]. Likewise, in this thesis, the MPL deposited MPS is referred to as “double-layer GDL” henceforth.

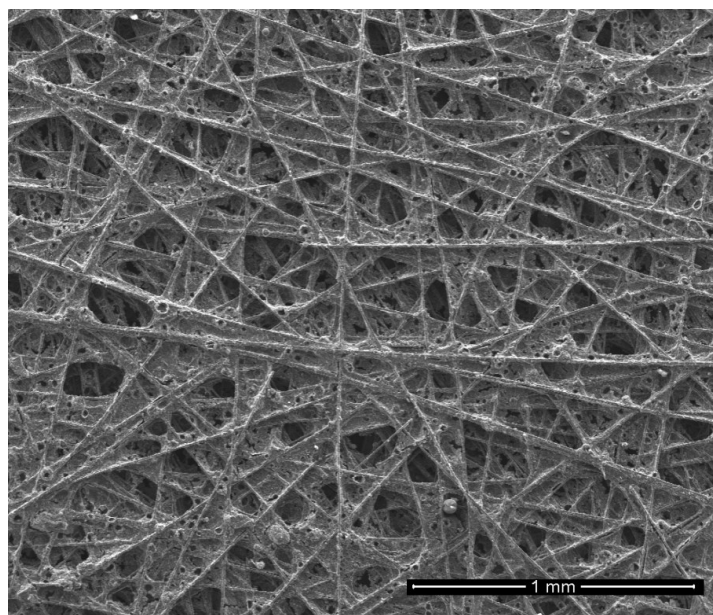
1.3.1. The Macroporous Substrate

The MPSs play multifaceted roles in the mass, heat, and electron transports, and their optimization for effective and concurrent mass, heat, and electron transport depends to a large extent on the development of ideal materials. Aside from the properties required for its primary functions against these three transport mechanisms, the MPS materials are also expected to fulfill some other expectations, such as high mechanical strength, high thermal and electrical resistance, and high stability and durability [31]. At least three decades of intense investigation and development have identified the expectations about MPS materials for effective cell operation. Even though a large variety of materials have been investigated as potential MPSs, for the virtue of brevity, they are classified into two main categories: metal- and carbon-based materials [31].

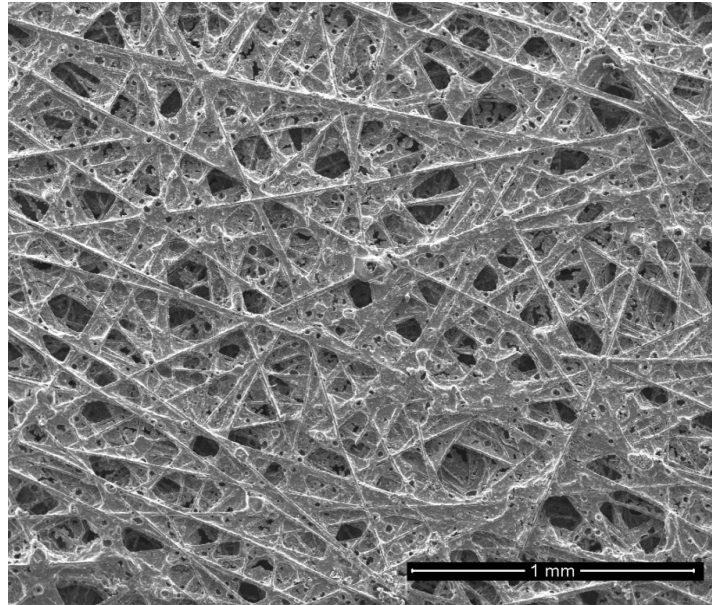
The metal-based MPSs, i.e., stainless steel fiber felts, metal foams, and machined metal substrates, are relatively newly introduced products and still under vehement investigation, due to their promising features, such as high electrical thermal and electrical conductivity, mechanical strength, along with easily adjustable pore characteristics, and hence physical characteristics [32–34]. However, the practical viability of these materials has not been confirmed yet, and so the current state-of-the-art fuel cells are typically assembled with MPSs made of carbon or carbon-based materials, such as carbon papers, carbon cloths, carbon foams, and carbon felts [35,36]. Among these products, in particular, carbon papers have conventionally been employed for both the anode and cathode sides, owing to their desirable features, which include but are not limited to high gas permeability, high electron conductivity, high chemical stability, high elasticity, and adjustable pore characteristics [37]. In addition, carbon papers possess relatively less intricate (or tortuous) microstructures, and thus they are much more suitable for partially humidified cell operation at moderate current densities [38].

A carbon paper, as shown in Fig. 1.3, may be described as a simple carbon-carbon composite, in which carbon fibers with the diameters of about 8 μm are bound to each other by a polymeric material in a web-like matrix [25]. Such a distinctive morphology and microstructure originates mainly from its fabrication process, through which the carbon sheets stacked undergo sequential carbonization and graphitization stages over 2000°C in specifically designed furnaces [10]. On completion of these steps, the carbon fibers acquire graphite-like properties, whereas the polymeric binder remains as amorphous carbon; therefore, its final morphology and microstructure is highly porous (>70%) and comprised of randomly aligned carbon fibers in

both the in- and through-plane directions [39]. Following the temperature-treatment processes, the MPS is generally immersed in a suspension based on a polymeric binder for stabilization. On completion of the stabilization step, the MPSs are usually undergone hydrophobic agent treatment to impart sufficient hydrophobicity to them; this step is crucial to make them sufficiently hydrophobic [40]. The hydrophobic treatment of MPSs can be applied via very different types of hydrophobic agents, such as polytetrafluoroethylene (PTFE) [41], fluorinated ethylene propylene (PVDF) [42], and fluorinated ethylene propylene (FEP) [43], polydimethylsiloxane (PDMS) [44], polyvinyl alcohol (PVA) [45], and perfluoropolyether (PFPE) [46]. After the hydrophobic treatment, the resulting MPS thickness is typically between 180-400 μm , while the pores in them are typically in the range of 10-30 μm according to [47], but in the range of 20-100 μm according to [48].



(a)



(b)

Figure 1.3: Scanning electron microscopy (SEM) images of the macroporous substrate (MPS) with and without hydrophobic agent treatment: (a) surface morphology of the MPS without hydrophobic agent treatment, the image showing the macro-scale open pores and orientation of the carbon fibres; (b) surface morphology of the MPS with hydrophobic agent treatment, the image showing the macro-scale open pores and the network built up by the hydrophobic agent, specifically in the regions near the surface.

1.3.2. The Microporous Layer

In PEM fuel cells, water management is a key problem, because it has a major influence on the ORR. Thus, water management has received a great deal of attention and become the center of research efforts in the fuel cell community. The existence of excess water inside the cell is the main limitation for mass transport – a phenomenon especially critical for the cathode electrode [7,49]. In cell operation, as mentioned earlier, water is produced at the membrane/CCL interface as a by-product of the ORR, besides being carried

via the protons from the anode electrode [10]. On the other hand, a certain portion of the water can also be transported from the cathode to the anode, if sufficient hydraulic pressure is built up at the CCL/membrane interface – the transport of the water in this way known as “back diffusion”[10]. The movement of the liquid water inside the fuel cell is schematically presented in Fig. 1.4 [50]. The back diffusion phenomenon can become effective, especially in the presence of sufficient pressure barrier that needs to be reached at the CCL/membrane interface.

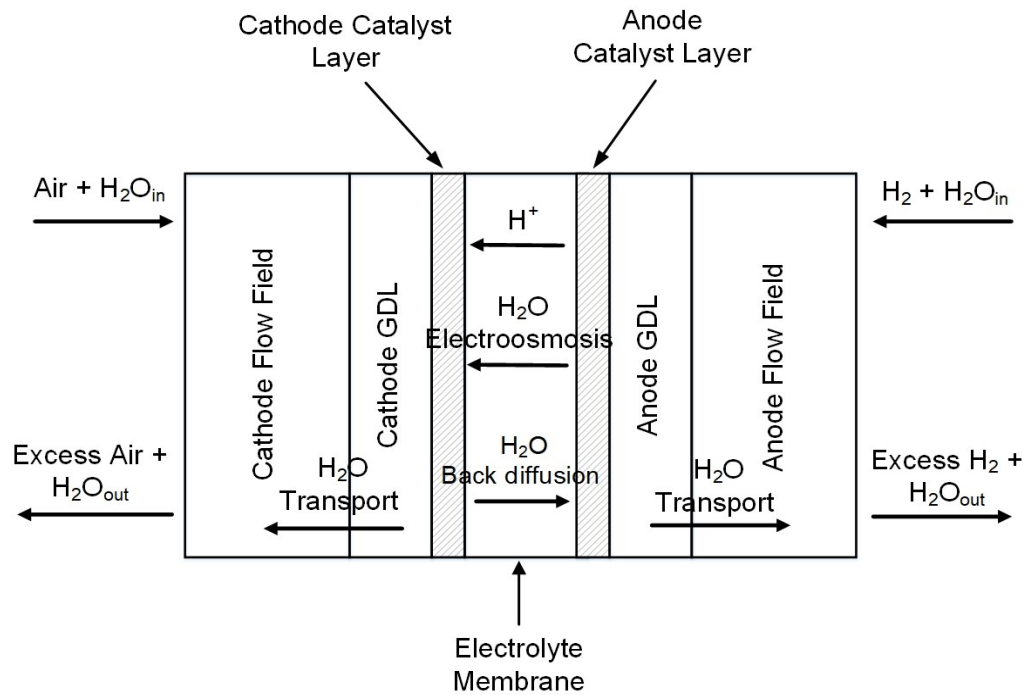


Figure 1.4: A schematic of water transport in a proton exchange membrane (PEM) fuel cell [50].

Herein, placement of a layer, i.e., an MPL, with relatively small pores can act as a pressure valve that keeps the water at the three-phase boundary, until a critical breakthrough pressure is achieved [31]. The MPL is therefore a key

component in the management of water (and to a lesser degree, heat) for enhanced performance, reliability, durability of fuel cells at high current densities for a broad range of practical applications [51,52].

The MPL is a simple composite of a carbon powder and a polymeric binder, as seen in Fig. 1.5. Owing to its unique morphology and microstructure, the MPL serves as a pressure valve with two functions: pushing water from the cathode to the anode (facilitating the water transport through back diffusion mechanism) and allowing pressure to build up, and hence expel the water across the less-hydrophobic pores of the GDL [50]. In the former case, the water droplets are forced to pass through the available pores inside the membrane by high liquid water pressure arising from the ORR and electro-osmotic drag, while in the latter case, the droplets generated at the CCL/membrane interface are transported through the GDL, and then expelled from the cell via the CFF [31].

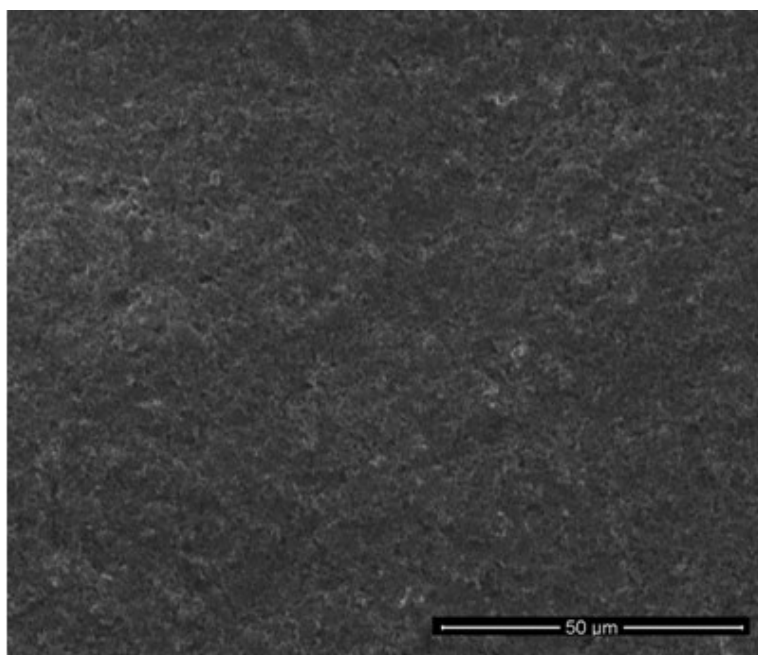


Figure 1.5: Scanning electron microscopy (SEM) image of the gas diffusion layer (GDL) (macroporous substrate (MPS) + microporous layer (MPL)): surface morphology of the double-layer GDL, the image showing the homogeneous, smooth, compact, and porous surface characteristics of the double-layer GDL.

As stressed, equilibrium between the former and latter cases is necessary for effective water removal and adequate membrane hydration, and the porosity and pore size distribution play key roles in this context. As the critical microstructural characteristics, porosity and pore size distribution are indeed of paramount importance, since they significantly influence several performance-affecting phenomena, including transport of reactants and by-products, electron transport, and formation of liquid water saturation profiles [53].

Aside from serving as a pressure valve, the MPL can also provide other benefits. An ideal MPL, for example, should enhance cell performance by (i) assisting in the distribution of oxygen over the CCL, (ii) reducing liquid water saturation from the CCL to the CFF by increasing capillary pressure due to its hydrophobicity and small pores (1-10 μm) compared to the GDL (10-100 μm), but larger pores compared to the CCL (0.001-5 μm), (iii) decreasing the electrical interfacial resistance between the CCL and GDL, (iv) enhancing the mechanical compatibility between the GDL and CCL, (v) providing mechanical support for the delicate CL, and lastly (vi) increasing catalyst utilization by preventing the precious metal catalyst from penetrating deeply into the GDL [54,55].

The fabrication of the double-layer GDLs (MPL deposited MPSs), in principle, involves three simple-to-perform steps, namely: MPL slurry preparation, deposition, and sintering. In the slurry preparation and deposition steps, carbon or graphite powder is mixed consecutively with hydrophobic agent dispersed deionized water, organic solvents, and additives, and then the resulting ink is deposited onto the MPS. The deposition can be made in several different techniques, including brushing, blading, spraying, and dipping/floating. As the last step, the double-layer GDL is first dried at $\sim 80^{\circ}\text{C}$ for 1 or 2 h to evaporate the surfactants, and then sintered at $\sim 340^{\circ}\text{C}$ for 30 min to distribute the hydrophobic agent homogeneously throughout the GDL [56].

As the morphological, microstructural, physical characteristics of the double-layer GDLs are greatly affected by the engineering parameters of the MPLs, i.e., the type and loading of the MPL powder, type and loading of the hydrophobic agent, pore modifications, and the conditions of the MPL deposition, sintering, and drying, extensive research efforts have been directed towards investigation and optimization of these parameters; for example, see [57–62]. Among them, the types and hence specifications of carbon powder have attracted great deal of attention, due to their significant impacts on cell performance.

Thus far, due to their alluring properties, i.e., high electrical and thermal conductivity, high corrosion resistance, affordable cost, wide availability (hence easy accessibility), and environmental acceptability, various types of carbon-based products – ranging from Vulcan XC-72R [63], Ketjenblack EC-300 J [64], Ketjenblack EC-600JD [65], to Black Pearls 2000 [57] and Hicon

Black [66] – have been investigated as potential MPL materials. Since different carbon-based materials have their own distinctive characteristics, their potential as MPL materials must be confirmed [56]. However, it is also known that PEM fuel cells with MPLs comprised of these carbon materials exhibit promising performance under only a very limited range of operating condition (see [56,67], for example), which is not fully satisfactory for large-scale commercialization, and more specifically, for the goal of achieving long-term operation under low-humidity conditions [68].

In addition, by their very nature, these carbon-based materials are highly susceptible to oxidation, particularly when they are exposed to a highly oxidative environment, limiting their practical viability – for instance, long-term functionality, along with suboptimal thermo-chemical stability [69]. All these are significant barriers to their potential use for next-generation MPLs. Considering these facts, there is currently a significant room for development and successful implementation of new materials that can completely overcome or at least mitigate the performance-limiting affects of the aforementioned drawbacks.

1.4. Scope and Outline of Thesis

In this thesis, graphene, “a monolayer of carbon atoms arranged in a two-dimensional honeycomb lattice” [70,71], is considered as an alternative to conventional MPL materials, owing to its appealing characteristics, such as excellent electrical and thermal conductivity, alongside favorable mechanical stiffness and elasticity [72,73]. By their very nature, graphene flakes are also prone to stack horizontally to construct a smooth layer [70]. Thus, placement of such a compact and smooth layer between the CL and MPS could

reasonably improve interfacial characteristics, and hence minimize interfacial electrical and thermal resistances and improve catalyst utilization.

As a two-dimensional (2D) main building block for carbon materials with all other dimensionalities (as schematically presented in Fig. 1.6) [74], graphene has emerged as a promising alternative to conventional carbon-based materials in various fields of energy and environmental studies; for instance, see [75,76]. Despite graphene's significant potential as an alternative MPL material, until now, only a very limited attention has been paid to its potential use for MPL preparation. Previous research on graphene-based MPLs seems to be encouraging, particularly when considering the operational flexibility targets established by the United States Department of Energy (DOE) for 2020 [72].

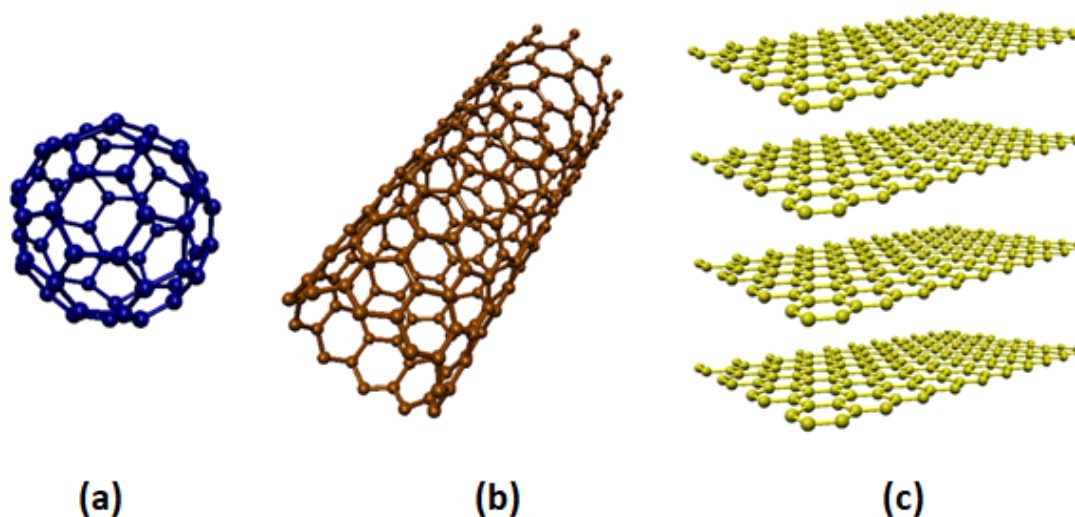


Figure 1.6: Illustrations of (a) wrapping up of graphene into a zero-dimensional (0D) buckyball, (b) rolling of graphene into a one-dimensional (1D) nanotube, and (c) stacking of graphene into three-dimensional (3D) graphite [8,74].

These research efforts have established an excellent background for further studies by revealing the positive effects of graphene-based MPLs, especially under low-humidity conditions, along with several open questions that call for further investigation. For instance, the morphological, microstructural, physical and electrochemical characteristics of graphene-based MPLs have not been fully understood yet. Equally important, the performance characteristics of graphene-based MPLs in scaled-up PEM fuel cells have not been studied or at least not reported in the open literature so far. Thus, these investigations as reported in this thesis will significantly contribute to finding an answer to the pertinent question of will the introduction of graphene into MPLs can break the PEM fuel cell' dependence on external humidifiers for membrane humidification, or will next-generation PEM fuel cells be assembled with graphene-based MPLs. The scope of this thesis is therefore to address these open questions by (i) assessing graphene-based MPL's morphological, microstructural, physical characteristics, (ii) scrutinizing its performance in a scaled-up fuel cell under different operating conditions, and (iii) investigating its potential influences on catalyst activity and catalyst utilization.

This thesis is comprised of six chapters. In chapter one, the importance of mass, heat, and electricity transport for a fuel cell is discussed, and the multifaceted roles of the GDL (MPS + MPL) in these three transport mechanisms are described. In chapter two, the main GDL characteristics, as indicators of GDL's capability in dealing with mass, heat, and electron transport, are presented in terms of effective transport properties for these physical quantities. In chapter three, a literature review of engineering/design parameters that have a decisive impact on the main characteristics of GDLs

are provided. In chapter four, a detailed discussion on *ex-* and *in-situ* experimental techniques that have been developed to estimate these main characteristics, is provided. In chapter five, the results of the *ex-* and *in-situ* experimental investigations conducted for the graphene-based MPL deposited MPS are presented, and the main advantages of the graphene-based MPL over a conventional MPL deposited MPS are revealed. Lastly, chapter six presents a summary of the main conclusions derived from the investigations conducted for the graphene-based MPL and provides recommendations for future studies.

Chapter 2

Characteristics of the Gas Diffusion

Layers

The operation and design characteristics, hence the efficiency of PEM fuel cells, are directly related to multiphase transport of mass, heat (or energy), and electrons in the porous cell components, namely the MPS, MPL, and CL. The inherently complex microstructures of these components present a significant challenge for the modelling of transport phenomena in fuel cells. Consequently, the transport of conserved quantity, i.e., mass, heat (or energy), momentum, and electric charge, are described via continuum equations by means of effective transport properties of porous medium. That is, the porous cell components' capability in dealing with mass, heat, and electricity transport is represented by their effective transport properties: an effective diffusion coefficient for the mass transport, effective thermal conductivity for the heat transport, and effective electron conductivity for the electricity

transport. For multiple-phase flow, absolute and relative permeabilities are the indicatives of fluid transport. The criticality of the GDL, as a key component that plays multifaceted roles in mass, heat, and electron transport through their concurrent management, has been increasingly recognized. These transport properties are a strong function of the characteristics of GDLs, whereupon this chapter provides a detailed discussion on the main characteristics of GDLs.

2.1. Characteristics of GDLs

An ideal GDL, typically a carbon-based product (e.g., woven carbon cloth, carbon foam, and non-woven carbon paper) sandwiched between the CLs and FFPs, should be designed to satisfy the expectations during cell operation. These expectations can be listed as follows [26–28]:

- (i) Desirable surface and cross-sectional morphological characteristics;
- (ii) Adequate porosity and pore size distribution to provide pathways for the reactants and products that flow in the reverse directions;
- (iii) Acceptably high electrical and thermal conductivity both in the in- and through-plane directions for effective electron and heat transport;
- (iv) Optimum gas permeability for effective liquid water transport;
- (v) Well balanced wettability (hydrophobicity/hydrophilicity) characteristics;
- (vi) Acceptable mechanical characteristics.

Because some of these expectations conflict with each other, they need to be carefully balanced to achieve performance improvement. This balance can

only be achieved through overall understanding of the main characteristics of GDLs. This section provides a review of the main characteristics of GDLs.

2.1.1. Porosity and Pore Size Distribution

A GDL (or a double-layer GDL) is an electrically conductive porous medium and typically composed of two sub-layers: MPS and MPL. The structure of a GDL (MPS + MPL) is presented in the previous chapter (Fig. 1.5). As a favorable MPS material, as presented in Fig. 1.4, carbon-fiber products, i.e., carbon paper, have been extensively employed due to their highly porous structures. However, as mentioned earlier, the MPL, which is mainly responsible for managing water transport, improving the catalyst utilization, and reducing the electrical interfacial resistance between the CL and the GDL, is basically composed of a carbon black powder and a hydrophobic agent (Fig. 1.5).

The pore size in an MPS (20-100 μm) is distinguishably higher than that in a double-layer GDL (1-10 μm) [48]. This difference is also clearly seen from the previously presented SEM images that show the surface morphologies of the MPS and double-layer GDL (Fig. 1.4 and Fig. 1.5). Small pore sizes within a double-layer GDL improves its water expulsion characteristics and makes it hydrophobic. However, large pores are important for reactant transport. In general, pores within the GDLs are categorized based on their size [22]:

1. Pores smaller than 0.07 μm are categorized as micropores
2. Pores in the range of 0.07-5 μm are categorized as mesopores
3. Pores larger than 5 μm are categorized as macropores

For micropores ($<0.01\ \mu\text{m}$), a diffusion mechanism, primarily referred to as Knudsen diffusion, is dominant. However, the diffusion through the macropores ($>5\ \mu\text{m}$) is basically controlled by another diffusion mechanism, generally referred to as bulk diffusion [22]. In macropores, therefore, the gas molecules principally diffuse based on molecular collisions, which further confirms the importance of macropores in effective mass transport. These conflicting effects make the optimization of these pore types inside GDLs inevitable, because optimized pore size distribution facilitates both reactant distribution and water removal [77]. Here, the pores categorized in the range of $0.01\text{-}5\ \mu\text{m}$ represent a transition between micro- and macropores. Thus, mesopores are practically preferred, since they balance these aforementioned effects.

To provide effective insights into the microstructural differences between the MPS and double-layer GDL, a comparison of their pore size distributions is shown in Fig. 2.1. Herein, for a proper comparison between the pore characteristics, the pores in both the MPS and double-layer GDL are divided according to their size into three categories: those smaller than $0.07\ \mu\text{m}$ are micropores, those between $0.07\text{-}5\ \mu\text{m}$ are mesopores, and those larger than $5\ \mu\text{m}$ are macropores. This classification is based on the gas-phase transport mechanism discussed above and may show differences with any other criteria determined for micro-, meso-, and macropores identification.

As evident from Fig. 2.1, the pore characteristics of the MPS and double-layer GDL are quite dissimilar. The porosity – a ratio between the total pore volume and bulk volume – of the MPS is around 75%, while it is around 68% for the double-layer GDL. In the MPS, about 7% of the total pore volume is

taken up by micropores, while approximately 42% and 51% of the total pore volume are in the meso- and macro-pore ranges, respectively. However, in the double-layer GDL, approximately 33% of the total pore volume is in the micro-pore range, 39% is in the meso-pore range, and 28% is in the macro-pore range.

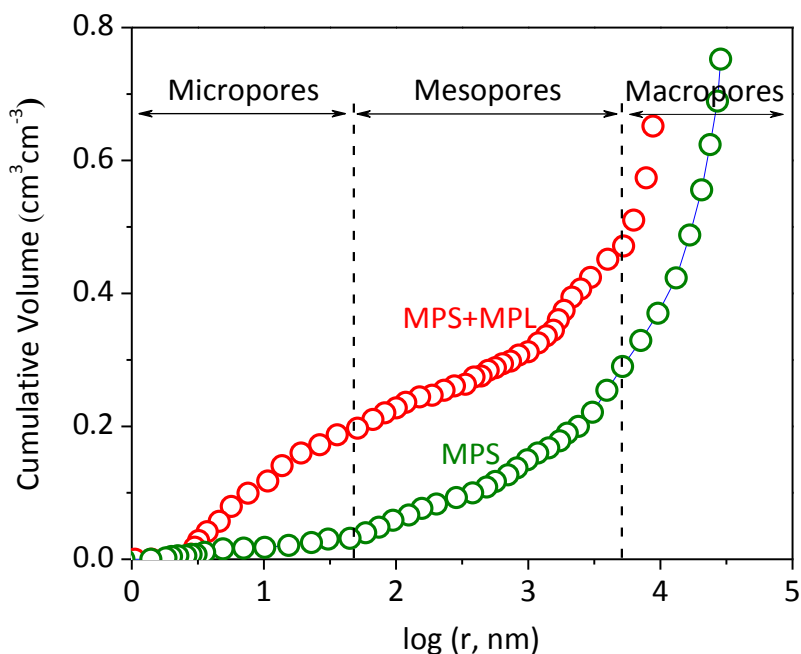


Figure 2.1: Cumulative pore size distribution in the macroporous substrate (MPS) and GDL (MPS + microporous layer (MPL)). r : pore radius; MPS: Avcarb EP40 carbon paper without hydrophobic treatment; GDL (MPS + MPL): Vulcan based MPL deposited onto the MPS (Avcarb EP40); Micropores: pores smaller than $0.07 \mu\text{m}$; Mesopores: pores in the range of $0.07\text{-}5 \mu\text{m}$; Macropores: pores larger than $5 \mu\text{m}$.

It is seen that the presence of the MPL in the structure causes a noticeable increase in the micro-pore volume and a significant decrease in the macro-

pore volume, but a slight drop in the meso-pore volume. The increase in the micro-pore volume indicates that the deposition of the MPL onto the MPS forms new and relatively small-scale pores; these pores could be ascribed to the formation of new pores at the interfaces of carbon particle-hydrophobic agent agglomerates and carbon fibers. The noticeable drop in the macro-pore volume, however, could be related to filling of pre-existing macropores with the carbon particle-hydrophobic agent agglomerates. The same phenomenon can also be used to explain the slight drop in the meso-pore volume. In general, the GDL has a relatively more uniform pore size distribution, as compared to the MPS, because it contains almost similar volumes of micro-, meso-, and macropores. Such a unique pore structure has been demonstrated to (i) minimize the water flooding in the cathode electrode (and hence mitigate the mass transport limitations), (ii) provide a more uniform water distribution profile in the cathode electrode, (iii) decrease the water saturation in the regions near the CL [68,78].

Recently developed physical models based on either X-ray radiographic visualizations or environmental scanning electron microscopy (ESEM) observations supported with water-transport pore-network analyses have provided more effective insights into the role of the MPL in the water transport [79,80]. According to these models [79,80], water saturation starts within the CCL, as it provides sufficient solid-liquid interfaces, and the water saturated at these interfaces starts to fill the available pores at the CCL/MPL interface, and then gradually spreads throughout the CCL/MPL interface. On accumulation of adequate water at this interface and achievement of a critical breakthrough pressure, the liquid water penetrates progressively into the MPL. Here, the presence of the MPL in the structure has been shown to cause

formation of relatively more breakthrough points, from which liquid water percolates in a more effective manner. More specifically, water passes through the breakthrough locations initially forms small water droplets, and then their number significantly increases, and finally in some regions, these small water droplets coalesce into larger water droplets. However, these coalesced water droplets are still small enough not to invade all the pores, and thus there are still available pathways, through which gas-phase reactants can be effectively supplied to the ERRs. On the contrary, the MPS itself is highly susceptible to water flooding, since there are relatively less breakthrough locations, and hence the water droplets are tend to fill the macropores close to the CCL and coalesce into larger connected water cluster, before percolating through the breakthrough points. Such a water movement profile makes the MPS highly susceptible to water flooding. Interested readers may also refer to [79,80] for further information about this phenomenon.

All in all, deposition of the MPL onto the MPS results in significant changes in its pore characteristics, which in turn tailor its microstructure for effective mass transport during cell operation.

2.1.2. Electrical Conductivity

In a PEM fuel cell, electrons produced in the ACL are transported through each individual cell component, except the electron insulator membrane and ionomer within the CLs. However, protons produced in the ACL are transported through the membrane and ionomers within the CLs. As mentioned earlier, during the transport of electrons and protons through the

cell components, voltage loss (ohmic polarization) occurs, and cell performance deteriorates correspondingly.

In a well-designed fuel cell, ohmic losses, which mainly result from the internal (bulk) resistances of the cell components (i.e., CL, MPL, MPS, AAFP, CAFP), as well as from the interfacial resistances between these components, should be minimized. Internal resistances are primarily attributed to the characteristics of the CL (i.e., thickness, tortuosity, uniformity, porosity, surface roughness, and ionomer content), GDL (i.e., porosity, tortuosity, thickness, and hydrophobic agent content), MPL (i.e., type and loading of carbon powder, hydrophobic agent, and uniformity), and AAFP and CAFP (i.e., material properties, flow-field geometry, and thickness) [81,82]. Interfacial resistances are, however, mainly related to the interfacial characteristics of these components.

Among these components, GDL is one of the critical ones that significantly contributes to the ohmic losses, as it is mainly responsible for the transport of electrons from/to FFPs and the electrical contact between the GDL and FFPs are not continuous, rather periodic, because of the geometrical characteristics of the FFPs. Therefore, electrons travel both in the in-plane and through-plane directions in the different parts of the GDL. In cell operation, the GDL does not entirely contact the FFPs due to the geometry of the FFPs. Thus, electrical conductivity in the in-plane direction becomes very important in compensating for the ohmic losses arising from the places where the through-plane electrical conduction is relatively poor, such as underneath the flow channels [83]. Depending on the morphological characteristics of the MPS and MPL, the transport properties of the GDL, i.e., electrical conductivity,

demonstrate significant differences in both the in- and through-plane directions [10].

Nevertheless, in many developed computational fluid dynamics models, the transport characteristics of GDLs have customarily been assumed to be isotropic; for example, see [84–86]. This assumption is considered “questionable”, since GDLs are comprised of fibers, which are anisotropically oriented in both the in-plane and through-plane directions (see Fig. 1.3 and Fig. 1.5, for example). Thus, the main transport characteristics, such as electrical conductivity, are reported to be completely different in the in- and through-plane directions. For instance, electrical conductivity in the through-plane direction is reported to be at least one order of magnitude smaller than that in the in-plane direction [87,88]. The anisotropic orientation of the carbon fibers in the in-plane direction makes the overall structure even more anisotropic, and hence the electron transport capability of the GDL also shows differences in the in-plane direction, such that the electrical resistance measured from a specific direction, say a reference direction, can vary by a factor of about two in any other direction in the in-plane axis [87,89].

The differences in the in- and through-plane electrical conductivities are mainly associated with the interfacial resistance, such that the through-plane electrical conductivity measurements are carried out as the porous medium is under mechanical compression, hence the resistance measured captures the contributions coming from both the bulk and contact resistances [90,91]. Because the interfacial resistance takes up a substantial portion of the overall through-plane resistance, the electrical resistance in the through-plane direction is correspondingly higher than that in the in-plane direction.

The interfacial resistance, and hence electrical resistance in the through-plane direction, is also known to increase with raising amount of electronically insulator hydrophobic agent in the carbon matrix. However, because the measurements in the in-plane direction are independent of interfacial resistance and the electronically conductive carbon matrix remains unaltered upon hydrophobic treatment, the in-plane electrical conductivity is not affected by the hydrophobic agent content in the carbon matrix. That is, the presence of the hydrophobic agent in the carbon matrix negatively affects the electrical conductivity in the through-plane direction, while does not have a noticeable impact on the electrical conductivity in the in-plane direction. The presence of the MPL in the structure is also known to positively affect the electron transport capability of the GDL, particularly in the through-plane direction, because the MPL's highly compressible structure facilitates filling of the macro-scale spaces between the MPS and FFPs [87]. The effect of the MPL on the GDL's electron transport capability in the in-plane direction depends to a large extent on the MPL's engineering parameters, as well as the resulting morphological and microstructural characteristics achieved upon MPL deposition.

Building on this, the electron transport capability of the GDL is a strong function of its morphological and microstructural characteristics, and any direction-dependent differences in these characteristics are known to significantly affect its electrical conductivity capability in these directions. One essential step towards optimization of the electron transport in a fuel cell is minimizing the internal and interfacial electrical resistances of the GDL, which requires explicit determination, and hence optimization, of its electron transport capability in both the in- and through-plane directions.

2.1.3. Gas Permeability

In PEM fuel cell operation, the generated or transported water at the CCL/membrane interface is absorbed into the ionomer embedded in the CL and then transported through the void regions of the CL and GDL, under the influence of convection with both in- and through-plane velocity components. Such a form of water transport occurs only in cases where the negative-pressure gradient of the gas phase is overcome by the capillary pressure gradient – a mechanism largely affected by the gas permeability of GDLs [92].

A high resistance to flow (or alternatively low gas permeability of the GDL) causes a high negative-pressure gradient, resulting in high saturation levels in the GDL. The high level water saturation in the GDL in turn induces water flooding, because of which the available pores of the GDL are filled with water, and correspondingly the pathways, through which the reactants are supplied to the ERR, are largely blocked. Thus, gas permeability is a critical parameter and is an indicator of the GDL's capability in convection-driven mass transport.

As mentioned earlier, GDLs typically undergo numerous mechanical, chemical, and thermal processes as well as treatments, and their microstructural and morphological characteristics (and hence physical and transport properties, particularly gas permeability), are largely affected by the specifications of these processes and treatments [93]. In addition to the manufacturing process, GDLs are commonly treated with hydrophobic agents (see Fig. 1.3), which usually makes them relatively condenser and changes their microstructural characteristics, and correspondingly reduces their through-plane gas permeability [10]. The presence of the MPL in the GDL

structure also changes its morphology and microstructure, and most of the time results in a drop in its gas-permeability.

In consequence, gas permeability, especially in the through-plane direction, is one of the important characteristics of GDLs, because it directly influences the reactant transport, by-products removal, and water saturation in cell operation. Thus, particularly through-plane gas permeability should be accurately measured to help optimize the design and manufacturing parameters affecting it [40].

2.1.4. Surface Wettability

In an operating fuel cell, particularly at high current densities, the water production rate becomes greater, leading to increased liquid water formation, and eventually becomes problematic by blocking the ERR within the CCL. The hydrophobic (water expelling) or hydrophilic (water retaining) characteristics of GDLs are paramount in water management [94,95]. The level of hydrophobicity or hydrophilicity is practically evaluated by measuring the static contact angle from the surface of the test-of-interest GDL. The static contact angle is, in principle, described as the angle measured from the solid, liquid, and gas interface.

As schematically presented in Fig. 2.2, a surface with a static contact angle higher than 90° is characterized as hydrophobic, whereas the one with a static contact angle lower than 90° as hydrophilic [96]. The static contact angle on an ideally flat surface is theoretically defined by the Young's Equation given in Eq. (2.1), and is basically an indicator of the surface free energies of materials

(a GDL in the present case), because it merely depends on the intrinsic properties of materials [97].

$$\cos(\theta_c) = \frac{(\gamma_{s-g} - \gamma_{s-l})}{(\gamma_{l-g})} \quad (2.1)$$

where γ_{s-g} , γ_{s-l} , and γ_{l-g} are the surface free energies of solid-gas, solid-liquid, and liquid-gas interfaces, respectively, and θ_c represents the static contact angle. It is important to note that Eq. (2.1) is only valid for the thoroughly smooth surfaces, since surface roughness plays a critical role in the wettability characteristics of materials.

Even though static contact angle measurement can give a general understanding of materials' hydrophobicity and hydrophilicity, it is not sufficient for evaluating the mobility of liquid on the surface of the material [97]. Thus, as an alternative approach to the static contact angle, a method, which is referred to as sliding contact angle, has been employed to evaluate the dynamic wettability characteristics of solid surfaces [98]. The sliding angle, as seen from Fig. 2.2, demonstrates the critical angle at which a droplet with a certain weight begins to slide down from the inclined surface. In this context, a lower sliding angle is the indicator of a more-hydrophobic surface characteristic, whereas a higher one is the indicator of a more hydrophilic surface characteristic [97]. The correlation derived by Furmidge [99], as given in Eq. (2.2), describes the relationship between the sliding angle and the surface and liquid properties.

$$\sin(\theta_s)mg = \sigma Rk(\cos(\theta_r) - \cos(\theta_a)) \quad (2.2)$$

where θ_s , θ_r , and θ_a represent the sliding angle, the receding contact angle, and the advancing contact angle, respectively (see also Fig. 2.2), and m is the mass of liquid droplet, g is the gravity, σ is the surface tension coefficient, R is the length scale, and k is the shape constant. Further information on the sliding contact angle measurements can be found in [97,100].

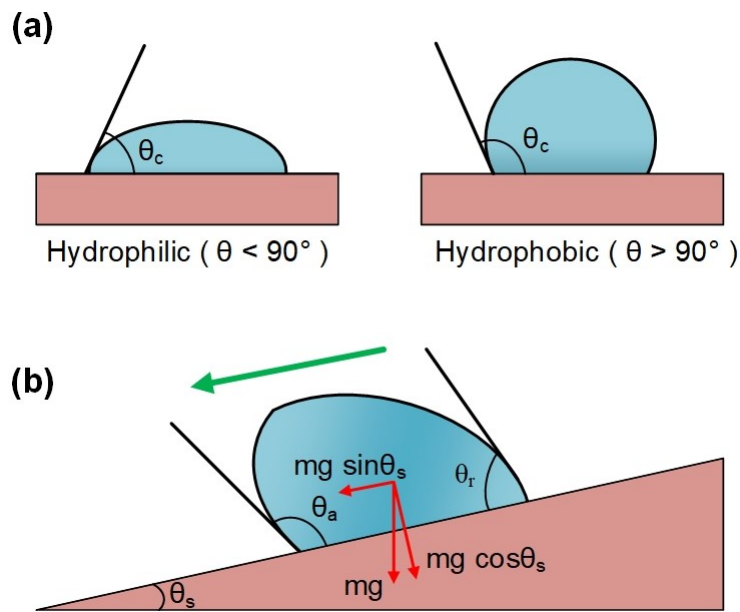


Figure 2.2: Schematics of (a) static contact angle (θ_c) measurements on hydrophilic ($\theta_c < 90^\circ$) and hydrophobic ($\theta_c > 90^\circ$) surfaces and (b) sliding contact angle (θ_s) [97].

The approaches discussed in this section are solely applicable for determining the qualitative wettability characteristics of GDLs via measuring the external contact angles. However, specifically in cell operation, the specifications of the chemical compositions (e.g., carbon powder loading and content of hydrophobic agent in the MPL) of GDLs become more dominant and affect performance differently. Consequently, the external contact angle

measurements have some restrictions in reference to providing quantitative information for design or calculation purposes [101].

Chapter 3

Literature Review

The operational characteristics of a fuel cell depend to a large extent on multiphase transport of mass, heat, and electricity in the porous cell constituents, such as the MPS, MPL, and CL. In particular, the importance of the GDL (MPS + MPL), as a key component that plays multifaceted roles in mass, heat, and electron transport through their concurrent management, has been increasingly appreciated. As mentioned earlier, the GDL's capability in dealing with these three transport mechanisms is represented by its effective transport properties, and all these transport properties depend to a large extent on the GDLs' main characteristics, such as morphology, microstructure (porosity and pore size distribution), gas permeability, and surface wettability. These GDL characteristics are in turn a strong function of the specifications of the materials, design parameters, and procedures followed in their manufacturing. Thus, this chapter provides a detailed discussion on the GDLs'

main materials, design parameters, and manufacturing procedure, as well as their potential effects on the GDL characteristics, and hence fuel performance.

3.1. Design parameters of GDLs

The design parameters of MPLs, i.e., type and loading of carbon black powder and hydrophobic agent and application of microstructure modification, greatly affect the microstructural and physical characteristics of double-layer GDLs, as summarized in Table 3.1. However, it is crucial to note that GDLs demonstrate different behaviors under different operating conditions depending on their microstructural (i.e., porosity and pore size distribution) and physical (i.e., electrical and thermal conductivity, gas permeability, and surface wettability) characteristics.

Thus, a PEM fuel cell constructed with a more-hydrophobic GDL may exhibit performance deterioration due to membrane dehydration under low-humidity conditions, but may demonstrate more-promising performance under high-humidity conditions. However, a fuel cell assembled with a more-hydrophilic GDL may perform better under low-humidity conditions due to its capability of retaining water, whereas it can show performance deterioration under high-humidity conditions because of water flooding [102]. Therefore, specifically to improve fuel cells' viability for the large-scale commercialization, the optimization of GDLs should be undertaken while simultaneously considering various operation conditions to satisfy the ever-changing loading demand during operation [68].

Characteristics of the GDL	Design parameters impacting the GDL characteristics	Potential effects on fuel cell operation	References
Gas permeability	<p>Material properties of raw GDL (e.g., pore size, pore shape, thickness, and compressibility)</p> <p>Hydrophobic agent content both in the MPS and MPL</p> <p>Type and loading of carbon black powder</p> <p>The thickness of the MPS and MPL</p>	<p>Impacts the transportation of gas species</p> <p>Critical for water management properties</p> <p>Important for limiting current density due to its influence on mass transfer limitations</p>	[103–105]
Electrical conductivity	<p>Material properties of the MPS</p> <p>Adhesion properties of the MPL</p> <p>Type and loading of carbon black powder in the MPL</p> <p>Hydrophobic agent content in the MPL</p> <p>The thickness of the MPS and MPL</p>	<p>Critical for reducing the ohmic losses</p> <p>Affect performance, notably at intermediate current densities</p>	[27,50,89]

Porosity and pore size distribution	<p>Hydrophobic agent content in the MPS and MPL</p> <p>Average pore size of carbon black powder used in the MPL</p>	<p>Critical for water management and reactant and by-product transport</p> <p>Influences heat management</p> <p>Important for ohmic losses</p>	[104,106,107]
Surface wettability	<p>Material properties of the MPS</p> <p>Hydrophobic agent content in the MPS and MPL</p> <p>Type and loading of carbon black powder in the MPL</p> <p>Arrangement of the MPL (Symmetric/Only on the cathode/Only on the anode)</p>	<p>Crucial for water management</p> <p>Critical for reactant and by-product distribution</p> <p>Impacts start-up performance</p> <p>Critical for degradation of components of membrane-electrode assembly (e.g., membrane degradation)</p>	[104,107,108]

Table 3.1: A summary of main characteristics of GDLs, design parameters affecting GDL characteristics, and the potential effects of GDL characteristics on fuel cell performance.

Tremendous research has focused on investigating the effects of the aforementioned design parameters of MPLs, e.g., type and loading of carbon black powder and hydrophobic agent and microstructure modification, on the microstructural and physical characteristics of GDLs as well as on cell performance. Thus, the following subsections are devoted to review the effects of critical MPL design parameters on GDL characteristics, with a particular interest in their potential influences on cell performance.

3.1.1. Effect of type and loading of carbon black powder

Because of their suitable characteristics, including wide availability, high corrosion resistance, environmental acceptability, high electrical and thermal conductivity, and unique surface features, carbon-based nanomaterials have been commonly employed in the fuel cell industry [77]. For instance, numerous carbon-based nanomaterials, such as Vulcan XC-72R [108], Ketjenblack EC-300J [109], Black Pearls 2000 [57], Ketjenblack EC-600JD [110], and Acetylene Black [57], have been introduced into the MPL to tailor the microstructural and physical characteristics of GDLs.

By modifying the microstructural and physical characteristics, it has been targeted to alleviate the performance losses associated with the mass transport limitations and provide better water management. As stressed, microstructural characteristics (i.e., pore characteristics) are indeed of paramount importance, since it simultaneously impacts the gas permeability and surface wettability characteristics. For instance, small pore sizes within a GDL improve its water expelling characteristics and make it hydrophobic. However, large pores are specifically important for reactant transport.

In an attempt to optimize the pore-size distribution inside GDLs, Chen et al. [57] manufactured cathode MPLs with different carbon black powders (i.e., Acetylene Black, Black Pearls 2000, and composite carbon black based on Acetylene Black and Black Pearls 2000) and different loadings (0.50, 1.00, 1.50, and 2.00 mg/cm²) and carried out electrochemical performance studies for the MEAs based on these MPLs at different air relative humidity (RH) conditions in a single PEM fuel cell. Their results demonstrated that it is possible to improve cell performance, particularly at low RHs (e.g., 40%) by using composite carbon black (made of 30 wt.% Black Pearls 2000 and 70 wt.% Acetylene Black) with an optimum loading (which is reported to be 1.50 mg/cm²). In their study, Black Pearls 2000 is found to be more hydrophilic, because it contains the relatively more micro- and macro-pores and fewer meso-pores.

Such a pore size distribution makes this carbon black more prone to water flooding, thus deteriorating its mass transport properties. However, in the same study, Acetylene Black is reported to be relatively hydrophobic, because it includes relatively more meso-pore volume and relatively less hydrophilic micro-pore volume. Thus, the combination of these two carbon black powders with different specifications is found to be promising in terms of cell performance, since such a composite carbon powder include sufficient micro-, meso-, and macro-pore volumes for effective reactant distribution and water management.

In another study, Passalacqua et al. [111] fabricated different MPLs made of different carbon black powders, such as Vulcan XC-72R, Asbury graphite 850, Shawinigan acetylene black, and Mogul L. The physical properties of

these carbon blacks as well as those of GDLs coated with these carbon black powders are summarized in Table 3.2. Results obtained from the polarization behaviors of the cells assembled with those MPLs confirmed that the type and specifications of carbon black powder considerably affects cell performance. Results obtained in these study are also in good agreement with those reported by Chen et al. [57]. In summary, the physical properties of the carbon-based materials employed inside the MPLs are found to substantially affect the mass transport and water removal characteristics of fuel cells.

Carbon powder type	Surface area (m ² /g)	Pore volume (cm ³ /g)	V _P (cm ³ /g)	V _S (cm ³ /g)	APR (μm)	APR _P (μm)	APR _S (μm)
Vulcan XC-72	250	0.489	0.319	0.170	1.80	0.24	4.90
Asbury 850	13	0.346	0.212	0.134	3.50	0.29	8.60
Acetylene Black	70	0.594	0.368	0.226	1.70	0.27	4.30
Mogul L	140	0.276	0.157	0.119	6.00	0.20	13.60

V represents the pore volume; APR represents the average pore volume; Subscripts P and S represent the primary and secondary pores, respectively.

Table 3.2: A summary of specifications for both the different carbon powders and the double-layer GDLs having these carbon powders in their MPLs, as reorganized from [111].

3.1.2. Effect of microporous layer thickness

For MPL thickness, the general consensus is that a very thick MPL causes high mass transfer limitations as well as electrical resistance, due to a lengthened diffusion path between the CL and FFP, whereas a very thin MPL does not provide sufficient reactant distribution and interfacial characteristics, and thus both increases the interfacial electrical and thermal resistances and mass transport limitations. In addition, with increasing MPL thickness, the water saturation level at the CCL and MPL interface is found to slightly increase, whereas it decreases in the pores of MPS [112]. These changes are considered to be beneficial for the transport of reactants. Overall, an ideal MPL thickness should be high enough to keep the water management and interfacial characteristics at an optimum level and low enough to facilitate oxygen transport [31].

3.1.3. Effect of hydrophobic and hydrophilic treatment

A proper hydrophobic agent content in a GDL, on both the anode and cathode sides, not only prevents the membrane drying up under low-humidity conditions but also offers effective water management under high humidity conditions [113]. Hence, the content of the hydrophobic agent inside a GDL determines its hydrophobic and hydrophilic characteristics. These characteristics further influence the water transport mechanism inside the GDL. In principle, within the GDL, as the pressure of water vapor exceeds the saturation level, water condensation occurs. The condensed water droplets are then driven from the CL to the FF by the difference between the gas and liquid phases, primarily referred to as capillary pressure. The capillary

pressure is reported to be as positive and negative for hydrophilic and hydrophobic GDLs, respectively [114]. However, the force subjected to water droplets inside GDLs demonstrates significant differences, depending on their hydrophobicity and hydrophilicity. Namely, the water removal becomes more effective in hydrophobic GDLs; thus, both MPS and MPL, are generally treated with different hydrophobic agents (i.e., PTFE, PVDF, FEP, PDSM, PVA, and PFPE) with various contents. The optimal PTFE loadings in the MPSs and MPLs are reported to be in the ranges of 10-20 wt.% and 5-35 wt.% depending on the operation conditions, respectively, to achieve effective water management and reactant distribution [115,116].

3.1.4. Effect of microstructure modification

The literature review presented in the previous sections indicates that the performance deteriorations associated with water management and mass transport limitations are mainly influenced by the architecture of GDLs. Further, it is emphasized that a delicate balance between the water management and reactant distribution can be constructed through an appropriate pore-size distribution within the GDL.

In this context, several research groups have modified the pore structures of double-layer GDLs by introducing various pore-forming agents, including Li_2CO_3 and NH_4Cl into the MPL. For example, Tang et al. [117] prepared MPLs with graded porosity by introducing NH_4Cl pore-former into MPLs with different contents and assessed their performance in a single cell. Results show that manufacturing MPLs with graded porosities facilitates the transport of liquid water while allowing effective reactant distribution, due to the presence of both small pores (which offer pathways for reactant

distribution) and large pores (which facilitate liquid water removal). Chun et al. [118] also prepared MPLs with graded porosities by introducing NH_4Cl into MPL inks with different contents and assessed their performances in a single fuel cell. Results demonstrate that MPLs having the greatest macro- and least micro-pore volume perform better under high-humidity conditions, while MPLs having the least macro- and greatest micro-pore volumes exhibit more-promising performance under dry conditions.

Building on this, it may be understood that bi-modal porosity distribution (the presence of large pores along with small pores) improves both reactant distribution and water management.

3.1.5. Microporous layer fabrication process

In general, the MPLs are fabricated by following a three-step procedure that involves sequential pretreatment steps, as schematically illustrated in Fig. 3.1. The first step is the preparation of MPL ink, through which graphene powder, 2-propanol, deionized (DI) water and hydrophobic agent (PTFE) are mechanically mixed and continuously stirred in an ultrasonic bath for 2 h at room temperature. Thereafter, the resulting slurry is spray-deposited onto one side of the MPS at 80°C , followed by heat treatment at 240°C for 1 h to evaporate any remaining solvent. Finally, the fully dried double-layer GDL is sintered at 350°C for 40 min to homogeneously distribute hydrophobic agent throughout the MPL. In general, the carbon powder (i.e., graphene powder) and hydrophobic agent loadings are held constant in the ranges of $0.5\text{-}5.0\text{ mg/cm}^2$ and $10\text{-}40\text{ wt.}\%$, respectively [57,119].

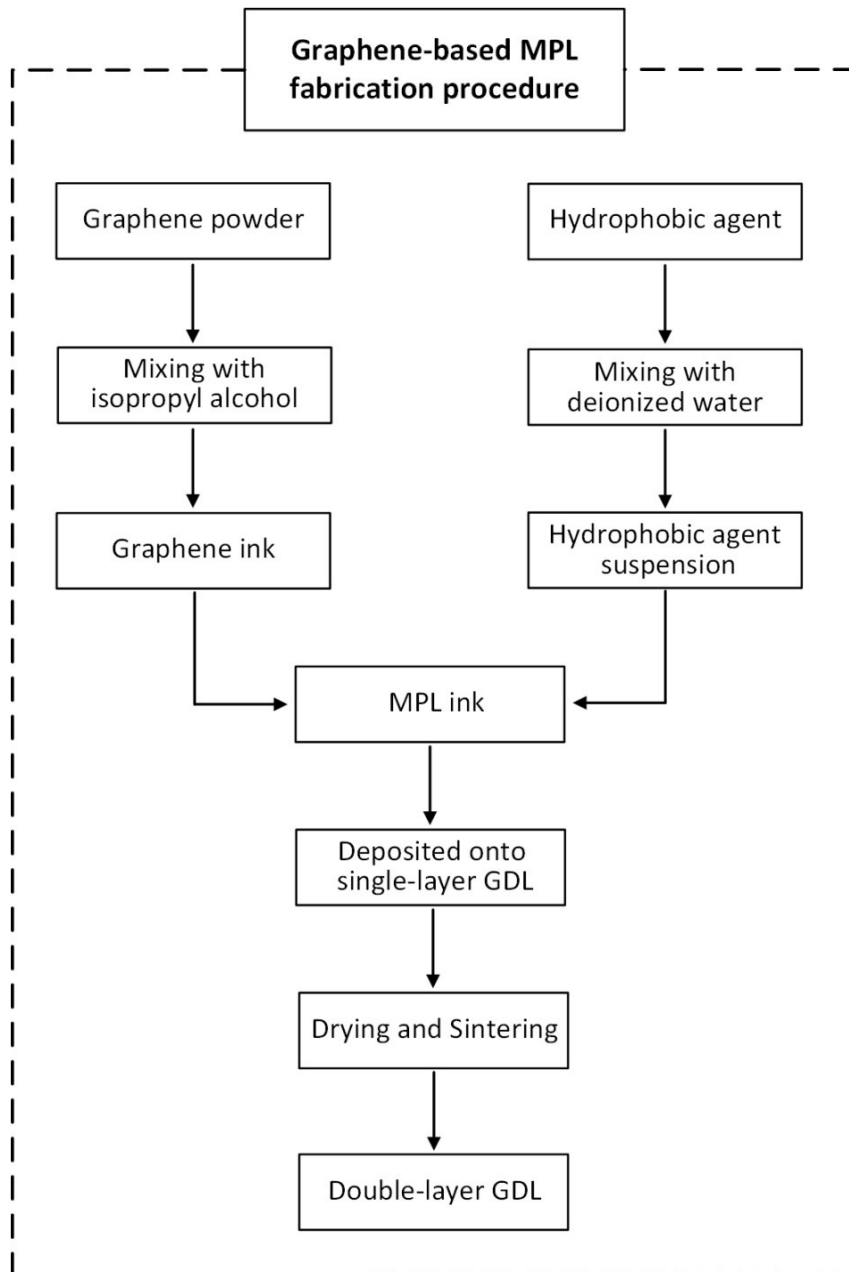


Figure 3.1: A procedure followed to deposit the graphene-based MPL onto the macroporous substrate (MPS).

Chapter 4

Characterization Techniques

The GDL, composed of a MPS and an (MPL), possesses a rather anisotropic microstructure, and so the transport properties are directionally dependent. For successful simulation and a better understanding of the transport phenomena in a GDL, the information pertaining to porosity and pore size distribution, electrical conductivity, gas permeability, and surface wettability is needed. This chapter therefore provides a review of *ex-* and *in-situ* characterization techniques developed to understand the microstructural and physical characteristics of GDLs.

4.1. Ex-situ Characterization of GDLs

The microstructural and physical characteristics of GDLs, such as porosity, electrical conductivity, gas permeability, and surface wettability, can be investigated by *ex-situ* characterization methods. These characterizations can be performed for both *pristine* and *post-mortem* GDLs, which enables fuel cell

researchers to obtain secondary information about the possible failures modes of GDLs. Therefore, the following sub-sections focus on the recent and most common *ex-situ* characterization techniques that have been employed to determine GDL's structural and physical characteristics.

4.1.1. Porosity and Pore Size Distribution

The microstructures and the surface characteristics of GDLs, i.e., porosity and pore size distribution, have been successfully determined through several techniques, such as mercury- [40,120], water- [121] or kerosene- [122] based intrusion techniques, capillary-flow porometry [83], and standard porosimetry [39]. However, among these techniques, the method of mercury porosimetry (MIP), standard porosimetry (MSP), and capillary flow porometry (CFP) have been extensively used due to the wide range of spectrum of measurable pore radii, typically from 2 to 10^5 nm [39], which is practically sufficient for the range of pore sizes commonly encountered in PEM fuel cell GDLs. However, it is worth noting that all these techniques principally hinge on general assumptions. For example, in these techniques, the capillary structure of the sample is basically represented by a bunch of tubes with a certain range of radii. Thus, it is suggested that the inferences about the internal microstructures of the samples under investigation should be made with specific consideration [83].

4.1.1.1. Mercury Intrusion Porosimetry (MIP)

Mercury intrusion porosimetry (MIP) basically relies on employing a high pressure to force mercury into the pore spaces within a porous medium in an attempt to determine its porosity and pore size distribution [10]. In this

technique, the sample extracted from the GDL is situated inside a vacuumed glass tube to guarantee that the only liquid inside the tube is mercury. Assuming that the mercury will only penetrate the porous medium only as a result of externally applied pressure, the initial volume of mercury is measured after it is put inside the glass tube. External pressure is then applied to help the small amount of mercury permeate the largest pores of the porous medium (because the higher the pore size, the less resistance to penetration the mercury experiences). The volume of the mercury that has penetrated is recorded. The pressure is then increased gradually until the small pores also fill with the mercury. The data on the volumes of mercury intrusion at specific pressure values are used to generate a capillary pressure versus saturation curve. Overall, this method enables determination of the hydrophobic and hydrophilic pore volume. However, accurate detection of overall pore volume is not always possible, especially for porous medium samples with smaller pore volume [123]. Therefore, the same analysis may be performed with different working fluids, such as water and kerosene, to achieve more accurate results.

4.1.1.2. Method of Standard Porosimetry (MSP)

The fundamental concept behind the method of standard porosimetry (MSP) is that changes in the weight of a working fluid in a GDL can be used to determine the capillary pressure and wettability characteristics of the test samples [124]. The type of working fluid is practically determined according to the specifications of the test-of-interest material, specifically to determine the pore size distribution in the GDL, ethanol and octane are preferentially employed, meanwhile larger pores are more easily measured when water is

employed as the working fluid. This method employs three disk-like samples (23 mm in diameter); two of them standard and the other is the GDL sample under investigation. These samples are stacked (the GDL sample is mounted between the standard samples, see Fig. 4.1), and it is known that they are in capillary equilibrium. Thus, the capillary pressure of the standard samples is equal to that of sample under test. Any change in their capillary pressure will affect both the standard and test samples equally; thus, the capillary pressure of the GDL sample can be obtained from the capillary pressure curve generated for the standard samples [10].

Prior to experiments, the standard and the GDL samples are situated inside a glass tube and vacuumed at a temperature of 180°C for 2 h to minimize the number of pores filled with air. Thereafter, the samples are immersed in the working fluid and stacked as described earlier. The samples are weighed at intervals and their weights are recorded while they are still stacked to determine the amount of working fluid saturation. Since the capillary pressure changes with the saturation of working fluid, it is possible to determine the capillary pressure of the GDL sample through comparison with the known capillary pressure curve of the standard sample. Generating the capillary pressure versus saturation curve for the test sample involves the steps shown in Fig. 4.1. These steps can also be summarized as follows:

Step #1: Determination of the sample's respective saturation levels from the data obtained for each individual sample from the intermittently measured weight of each sample, since their capillary pressure can be found from the saturation of working fluid – which is the information obtained from the intermittent measurements.

Step #2: Determination of the capillary pressure of the test sample under the assumption that the test and standard samples are in capillary equilibrium. That is, the capillary pressure of the test sample is equal to that of the standard samples.

Step #3: Repetition of the first two steps for each individual saturation measurement.

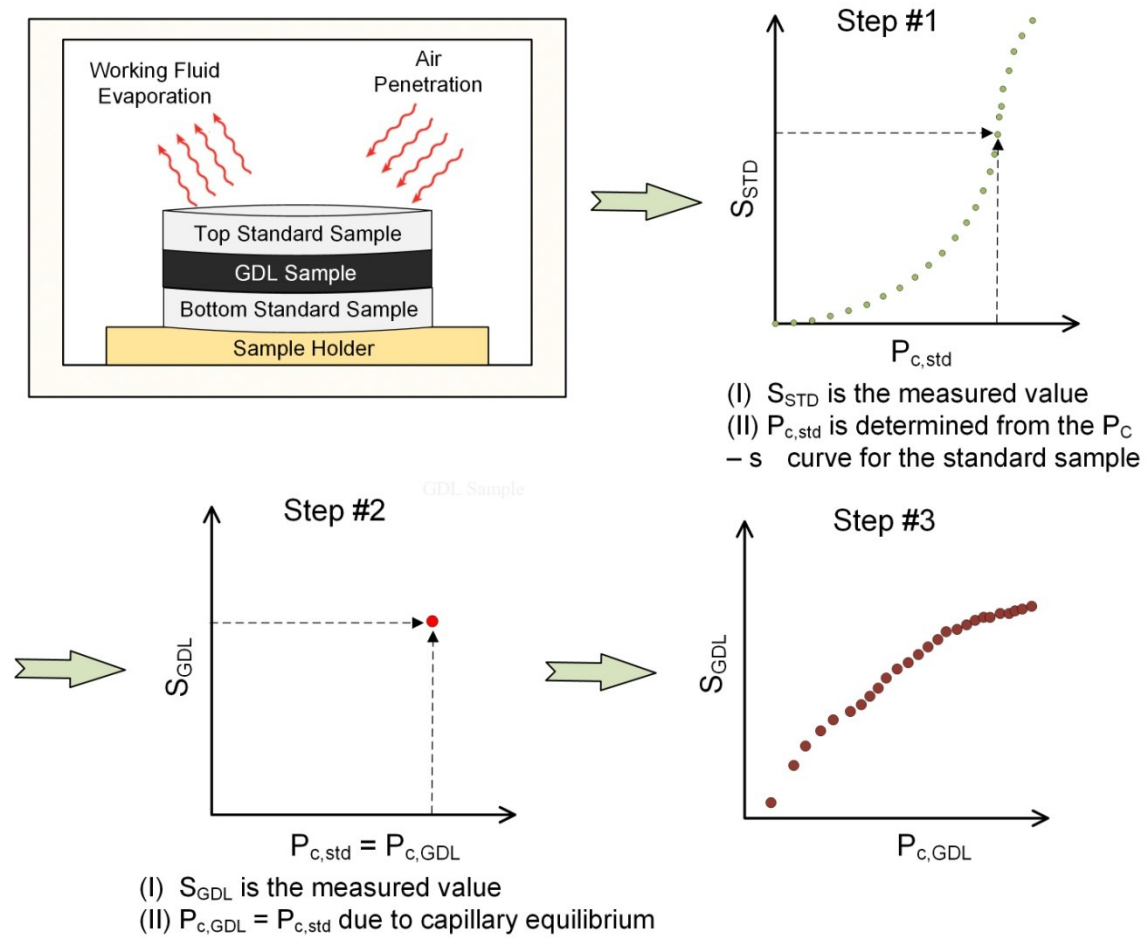


Figure 4.1: A schematic of the procedure to determine the capillary pressure curve of the gas diffusion layers (GDLs) through the method of standard porosimetry (MSP) [10,25].

4.1.1.3. Capillary Flow Porometry (CFP)

Capillary flow porometry (CFP) is very similar to the intrusion methods based on different working fluids [125]. However, as the potential working fluids, instead of non-wetting fluids, i.e., mercury, wetting fluids, such as octane and water, are commonly employed. Hence, the method of CFP is considered to be advantageous compared to MIP, since it is relatively faster and non-destructive [83]. In addition, owing to the highly wetting features of octane, this method enables the determination of both hydrophobic and hydrophilic pores (however, water is preferentially employed to determine the hydrophilic pores).

In this method, firstly, gas pressure and flow rates through the tested GDL sample are recorded, and then the wetting liquid is soaked into the pores of the sample, and the bulk material porosity of the sample is measured [126]. Once the pores of test sample are completely filled with the wetting liquid, a pressurized and non-reacting gas is applied to the surface of porous medium to remove the wetting liquid from the pores. The pressure required to remove the wetting liquid from the pores can be identified, as the function of pore diameter (D), the surface tension of the wetting fluid (γ), and the contact angle of the wetting liquid (θ) [83]:

$$P = \frac{4\gamma\cos\theta}{D} \quad (4.1)$$

Using the pressure difference between the wetting liquid and gas, the function of pores size distribution can be expressed, as follows [83]:

$$f = -\frac{\left(\Delta \frac{F_w}{F_d}\right)}{\Delta D} \times 100(\%) \quad (4.2)$$

where F_w and F_d are the flow rates of wet and dry gas, respectively. That is, in this technique, the pore size distribution throughout the porous medium can be determined from the difference between the flow rates of wet and dry gases using the small pressure difference for through-plane flow [127].

4.1.2. Electrical Conductivity

This section presents two extensively employed techniques for the determination of electrical conductivity characteristics of GDLs in the in- and through-plane directions.

4.1.2.1. In-plane Electrical Conductivity

The in-plane electrical conductivity of GDLs is commonly measured by the method, primarily referred to as the method of four-probe, as described in detail in [128]. In this technique, the GDL sample, as seen in Fig. 4.2, is mounted between the copper electrodes and an insulating plate. A direct current is applied from each end of the GDL sample through the copper electrodes by a four-probe device, as illustrated in Fig. 4.2. The voltage difference between the two selected points, which are located at the middle of the GDL, is measured via two gold-plated probes and the four-probe device. Then, the resistance between these selected points can be simply calculated by Ohm's Law. Here, the distance between the probes should be kept constant to achieve explicit measurements. In this technique, as reported in [128], a general mathematical formula, which involves a geometry-dependent correction factor, is described as the function of the dimensions of the GDL

sample and the space between the probes [87]. Here, the geometry-dependent correction term is the function of the ratio between the length and width of a GDL and the width and distance between the probes. These ratios were found to be 5 and 1, respectively (see [87]). To calculate the electrical resistivity of the GDL sample (ρ_{GDL}), the linear correlation given in Eq. (4.3) can be used [128]:

$$\rho_{GDL} = CtR \quad (4.3)$$

where C is the geometry-dependent correction factor, t is the thickness of the GDL, and R is the measured electrical resistance between the probes. The calculated resistivity of the GDL (ρ_{GDL}) can also be used to determine the electrical conductivity of the GDL in the in-plane direction. Equation (4.4) gives the correlation between the in-plane electrical conductivity and the electrical resistivity of the GDL.

$$\sigma_{GDL} = \frac{1}{\rho_{GDL}} \quad (4.4)$$

The electrical resistivity of the sample is determined in a manner similar to that reported in [87], as follows:

$$\rho_{GDL} = R \frac{dt}{L} \quad (4.5)$$

where ρ is the resistivity of the sample ($m\Omega \text{ cm}$), R is the resistance measured between the two inner probes ($m\Omega$), d is the diameter of the tungsten tip (cm), t is the embedded length of the tungsten tip (cm), and L is the distance between the inner probes (cm). In general, for each sample, at least 20 resistance values are collected for each pair of the fixed inner probe locations, and the measurements are repeated for three different pairs of the inner probe

locations with multiple samples, which have been cut off from the GDL sheet in different directions to keep the error range associated with the anisotropy of the GDL at minimum.

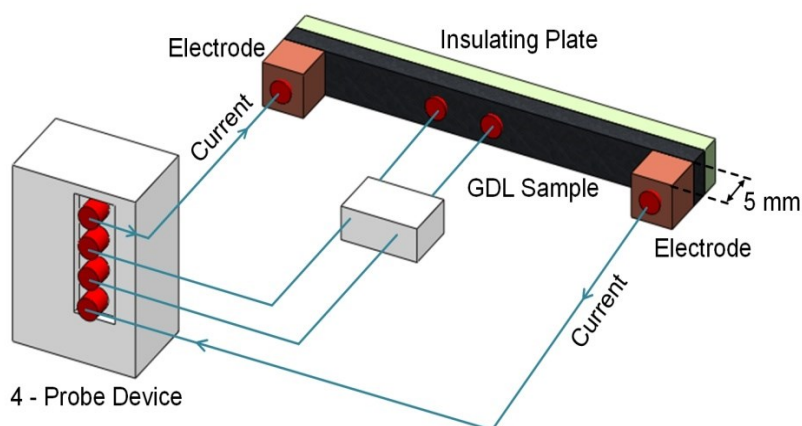


Figure 4.2: A schematic of the experimental setup employed to determine the in-plane electrical conductivity of gas diffusion layers (GDLs) [87].

4.1.2.2. Through-plane Electrical Conductivity

Through-plane electrical conductivity measurement in its simplest form, as discussed in detail in [89], involves (i) sandwiching a disk shape GDL sample (10 mm in diameter) between two highly conductive steel disks (with the diameter and thickness of 10 mm and 1.5 mm, respectively), (ii) placing the obtained stack between the highly conductive electrodes (usually gold-plated electrodes), (iii) situating the GDL-electrode between two insulator plates, and (iv) applying a gradually increasing compression force through the bolts of the setup together with direct current, as illustrated in Fig. 4.3. Furthermore, it

includes measuring the resistance of the electrodes together with the metal disks, including the contributions from the interfacial resistances between the tested GDL and metal disks, as well as the bulk resistance of the GDL, by using the voltage drop. The contributions to the measured resistance can be expressed as follows:

$$R_{\text{total}} = 2R_{\text{el}} + 2R_{\text{st}} + R_{\text{GDL}} + 2R_{\text{GDL-st}} + 2R_{\text{st-el}} \quad (4.6)$$

where R_{el} , R_{st} , and R_{GDL} are the bulk resistances of the electrode, steel disk, and GDL, respectively. However, $R_{\text{GDL-st}}$ and $R_{\text{st-el}}$ represent the contact resistances between the couples of GDL-steel disk and steel disk-electrode, respectively. For the resistance of the setup (in a case when no GDL is situated between the steel disks), the correlation expressed, as follows:

$$R_{\text{setup}} = 2R_{\text{el}} + R_{\text{st}} + 2R_{\text{st-el}} \quad (4.7)$$

where R_{setup} is the total resistance of the setup schematically displayed in Fig. 4.3. The contact resistance between the GDL and steel plate can be found by subtracting Eq. (4.7) from Eq. (4.6).

$$R_{\text{st-GDL}} = \frac{1}{2}(R_{\text{total}} - R_{\text{setup}} - R_{\text{st}} - R_{\text{GDL}}) \quad (4.8)$$

The bulk resistance of the steel disk can be calculated by multiplying its resistivity and thickness, whereas that of the GDL can be obtained following the similar procedure reported in [10,83]. Because of the porous structure of the GDL, the bulk resistivity of the GDL (ρ_{GDL}) can be calculated considering the volume fraction weighted harmonic mean of the resistivity of the carbon fibre and air, as follows:

$$\rho_f = (1 - \varepsilon)\rho_{\text{GDL}} \quad (4.9)$$

where ρ_f is the resistivity of the carbon fiber and estimated to be $4.02 \times 10^{-5} \Omega \cdot \text{m}$ [10]. In light of this equation, the porosity of the GDL can be calculated, as mentioned in [129], by using the correlation in Eq. (4.10). In this correlation, the bulk density is suggested to be taken as $1.80 \text{ g} \cdot \text{cm}^{-3}$ [130].

$$\varepsilon = 1 - \left(\frac{\text{Areal weight (kg} \cdot \text{m}^{-2})}{\text{Thickness of the GDL (m)} \times \text{Bulk density of the GDL (kg} \cdot \text{m}^{-3})} \right) \quad (4.10)$$

The calculated porosity of the GDL via Eq. (4.10) can also be used to determine the resistivity of the GDL through Eq. (4.9). The calculated resistivity of the GDL can then be converted into its bulk resistance by multiplying it with the thickness.

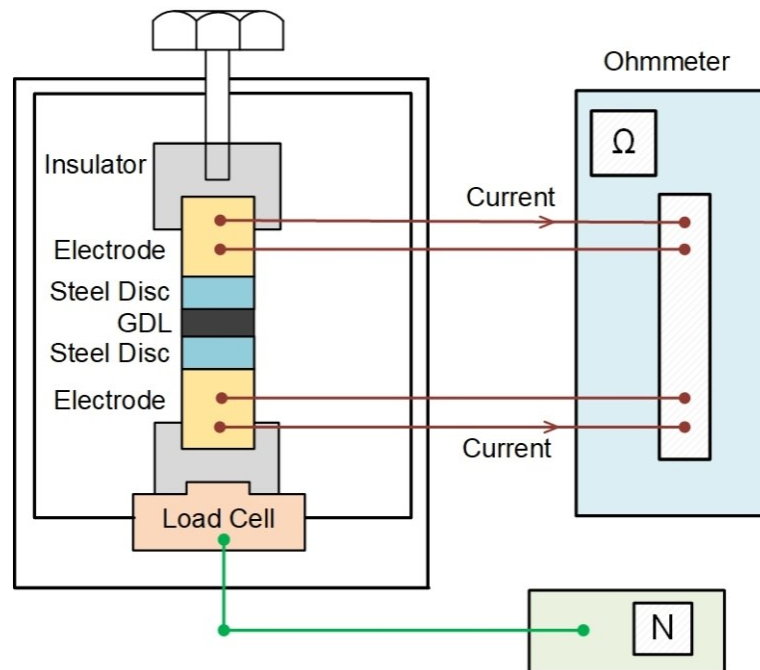


Figure 4.3: A schematic of the experimental setup employed to determine the through-plane electrical conductivity of gas diffusion layers (GDLs) [87].

4.1.3. Gas Permeability

This section presents the techniques used for the determination of gas permeability characteristics of GDLs in the in- and through-plane directions.

4.1.3.1. Through-Plane Gas Permeability

The experimental apparatus displayed in Fig. 4.4 has been conventionally used by many research groups to explore the anisotropic permeability characteristics of GDLs under different compressions [104,131]. The experimental setup is specifically designed to replicate the pore structure of the GDL inside a single cell. In this experimental apparatus, the GDL sample (generally in the shape of a disk with a diameter of 30 mm), as seen from Fig. 4.4, is sandwiched between two metal plates, which simulates the GDL situated between the flow-field plates, with variable spacing to control the compression level. The setup also allows for the measurement of pressure difference at the inlet and outlet of the cell via a differential pressure transducer, which is directly connected to a computer so that the pressure drop between the inlet and outlet of the cell can be precisely recorded. In addition, the flow rate of the air passing through the GDL sample is measured via a digital flow meter [104].

In the experiments, the test-of-interest GDL sample (cut into a circular shape with a diameter of 30 mm) is mounted between the metal plates, and the flow rate of the supplied air is changed from 100 to 500 ml/min, in 100 ml/min increments, and corresponding pressure differences are recorded once a steady-state condition is reached. All the experiments are performed with air at 75°C to simulate the operating conditions during the actual cell

operation. Under the assumption that the velocity change of the air in the setup is negligible (due to the superfine architecture of the GDL), the properties of air are assumed to be constant, and the flow inside the apparatus is assumed to be single-phase, and the Reynolds number is assumed to be significantly low.

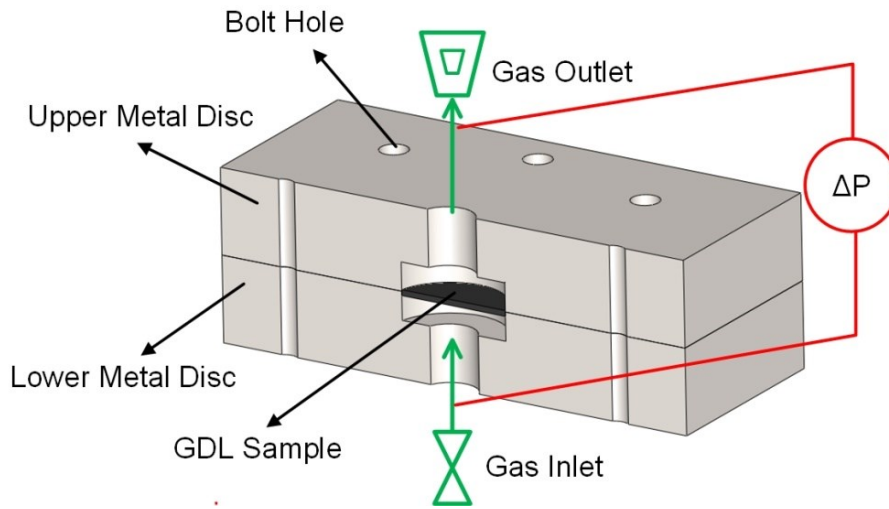


Figure 4.4: A schematic of the experimental setup employed to determine the through-plane gas permeability of gas diffusion layers (GDLs) [131].

With all these assumptions, the solution of Darcy's Law for single-phase one-dimensional compressible fluids is utilized to calculate the permeability coefficients of GDLs, as follows [131,132]:

$$\frac{P_{in}^2 - P_{out}^2}{2RLT/MW_{air}} = \frac{\mu}{K} (\dot{m}'') \quad (4.11)$$

where K is the permeability of the tested GDL sample, P_{in} is the inlet pressure of the air (Pa), P_{out} is the outlet pressure (Pa), R is the universal gas constant ($J \text{ mol}^{-1} \text{ K}^{-1}$), L is the thickness of the sample (m), T is the temperature of the

supplied air (K), MW_{air} is the molecular weight of air (kg mol^{-1}), μ is the dynamic viscosity of air (Pas), and \dot{m}'' is the mass flux across the sample ($\text{kg s}^{-1} \text{m}^{-2}$). The permeability tests are repeated seven times for each sample, and the results are presented as a range as well.

4.1.4. Surface Wettability

This section presents two most commonly used *ex-situ* characterization techniques to determine the surface wettability characteristics of GDLs.

4.1.4.1. Sessile Drop Technique

Sessile drop technique is one of the most extensively used methods for measuring the external contact angles of GDLs, and primarily involves setting a liquid, i.e., generally deionized (DI) water, droplet on the surface of a GDL, fitting a tangent to the solid/liquid/gas phase point (which overlaps with the line where the liquid droplet touches the GDL surface), and measuring the external contact angle [133].

The experimental apparatus used for this technique is comprised of a digital video camera with high resolution, software for calculating the external contact angle and surface energy, and a dispenser for generating droplets with appropriate radii. The apparatus is also connected with a sample holder (to hold the sample with different angles from 0° to 90°), which makes it usable for both static and sliding contact angle measurements. The liquid droplet volume should be as small as possible to prevent errors arising from the weight of a droplet itself, and the data should be taken before any change in the volume and shape of the droplet due to evaporation [133].

For the measurements, the sample-of-interest is situated under the dispenser, and a water droplet with a fixed volume, say 7 μl , is dropped onto it. The tangent line overlapping point, where the droplet touches the GDL surface, is fitted to the three-phase point, and the external contact angle is determined through the software. For each sample, the measurements are recorded from at least 15 different locations, and the results are presented as a range.

4.1.4.2. Wilhelmy Plate Technique

Wilhelmy plate technique, which can be applied both statically and dynamically, is another common practice for the external contact angle measurements of GDLs. The static version mainly involves inserting a GDL sample, preferably a rectangular one into a liquid to a known distance and measuring the force required for that insertion. However, for the dynamic version, the GDL sample is again vertically dipped into the liquid and then hoisted at a constant rate, and the force needed for these steps is recorded. The data obtained from the measurements are utilized to determine the surface wettability characteristics of the GDL under investigation. Wilhelmy plate technique is reported to offer more-accurate results for the external contact angle measurements of GDLs than its sessile drop counterpart, owing to the larger number of measurements [83].

4.2. In-situ Characterization of GDLs

Even though the *ex-situ* characterization techniques introduced in the previous sub-section are important for the estimation of the microstructural and physical characteristics of GDLs, *in-situ* characterization is essential for

understanding the behavior of GDLs under actual operating conditions [83]. In principle, *in-situ* characterization techniques require the placement of the MEAs containing GDLs with certain characteristics inside the cell and enable a comprehensive performance investigation under actual operating conditions. The following subsections therefore focus on the electrochemical performance assessment of GDLs (MPS + MPL) as the commonly used *in-situ* characterization techniques.

4.2.1. PEM Fuel Cell Performance Analysis

The electrochemical assessment of GDLs (MPSs + MPLs) in a single fuel cell provides practical insights into the viability of the materials, i.e., graphene, used for the constituents, such as MPS and MPL, under actual operating conditions [98].

In order to investigate these constituents' cell performance, firstly, an MEA based on the test-of-interest cell constituents is manufactured by following a fabrication procedure that involves several consequent steps, such as catalyst ink preparation, catalyst ink deposition, and sandwiching the constituents as an assembly. Firstly, the catalyst ink is prepared by ultrasonically blending Pt-C (i.e., 68 wt.%, TKK) with perfluorosulfonic acid, deionized (DI) water, and 2-propanol for 1 h at room temperature. The resulting ink is directly sprayed onto each surface of the membrane (i.e., Nafion[®] 211) until a certain platinum loading, say 0.5 mg/cm² (a cathode loading of 0.4 mg/cm² and anode loading of 0.1 mg/cm²), is achieved. Then, the test-of-interest anode double-layer GDL (i.e., Avcarb GDS 3250) is placed on the anode side, while the test-of-interest cathode double-layer GDL is placed on the cathode side.

On completion of the MEA manufacturing, the performance of the MEA manufactured is determined by obtaining the steady-state current voltage curves (I-V) via fuel cell test stations under very different operating conditions; for example, under varied air and hydrogen relative humidities, pressures of hydrogen and air, cell temperatures, and air and hydrogen flow rates. The schematic of a typical fuel cell test station together with the auxiliary equipment is presented in Fig. 4.5.

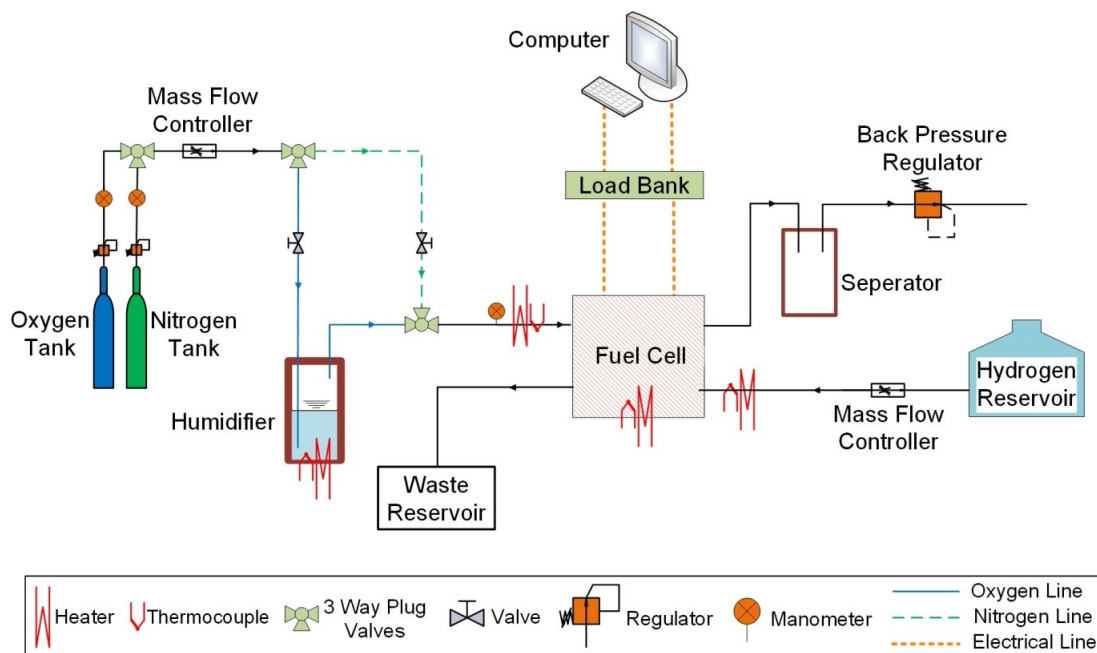


Figure 4.5: A schematic of the fuel cell test station and its components.

The primary component of the fuel cell test station is the cell with a certain electrode geometric area, say 45 cm^2 . On completion of leakage testing, the MEA is first assembled into the cell and activated. To generate the polarization curve, each voltage value at the corresponding current density is recorded potentiostatically from open-circuit voltage (OCV) to $\sim 0.02 \text{ V}$, in 0.10

V decrements. The voltage values are recorded once a steady-state condition is reached, which typically requires 4 to 6 min. For better accuracy, in general, each polarization curve represents the average of three polarization curves obtained from the measurements performed on three consecutive days under the above-mentioned operating conditions.

4.2.2. Electrochemical analysis

4.2.2.1. Cyclic Voltammetry (CV)

Cyclic voltammetry (CV) is an electrochemical analysis widely used to determine the electrochemical surface areas (ECSAs) of the MEAs assembled with the test-of-interest GDLs. The *in-situ* CV analysis is performed via a commercial fuel cell test station, equipped with a frequency response analyzer. The measurements are carried out by supplying nitrogen and hydrogen to the cathode (working electrode) and anode (the reference and also the counter electrode) of the single cell. The applied potential is swept from 0.10 to 0.80 V, at a scanning rate of 0.05 V/s. For better accuracy, CV measurements of each MEA are recorded after 20 sequential cycles. The ECSA for each MEA is determined according to the coulombic charge for hydrogen adsorption and desorption shown below:

$$ECSA = \frac{Q_{ads/des}}{Q_{ref} \cdot m_{Pt}} \quad (4.12)$$

where Q_{ref} and $Q_{ads/des}$ represent the adequate charge for oxidizing a monolayer of hydrogen on the surface of the platinum nanoparticles and total charge of the hydrogen adsorption/desorption area, respectively, while m_{Pt} is the platinum loading on the electrode [134].

Platinum utilization can also be calculated by using the CV data and the size of the platinum nanoparticles to demonstrate the potential impact of the individual cell components on catalyst utilization. In general, high-resolution transmission electron microscopy (HRTEM) images of the platinum nanoparticles are utilized to determine the size of the platinum nanoparticles used in the electrodes of the MEAs. The surface averaged particle size (d_s) of the platinum nanoparticles is calculated in a manner similar to that suggested in [135], using the following correlation:

$$d_s = \frac{\sum_{i=1}^n n_i d_i^3}{\sum_{i=1}^n n_i d_i^2} \quad (4.13)$$

where n_i is the number of platinum nanoparticles with a diameter of d_i . The d_s is determined by capturing at least 50 different particles from randomly selected regions. Platinum utilization for the each MEA is estimated from the ratio of the MEA over the geometric surface area (GSA) of the platinum nanoparticles, as follows [136]:

$$\text{Pt utilization (\%)} = \frac{\text{ECSA} \left(\frac{\text{m}^2}{\text{g}_{\text{Pt}}} \right)}{\text{GSA} \left(\frac{\text{m}^2}{\text{g}_{\text{Pt}}} \right)} \times 100 \quad (4.14)$$

The GSA of the platinum nanoparticles can be calculated by using the previously determined d_s and the density of platinum ($21.4 \times 10^6 \text{ g/m}^3$) [137]:

$$\text{GSA (m}^2/\text{g}_{\text{Pt}}) = \frac{6}{\rho_{\text{Pt}} d_s} \quad (4.15)$$

From Eq. (4.13) and (4.15), platinum utilization for the MEAs can be found.

Chapter 5

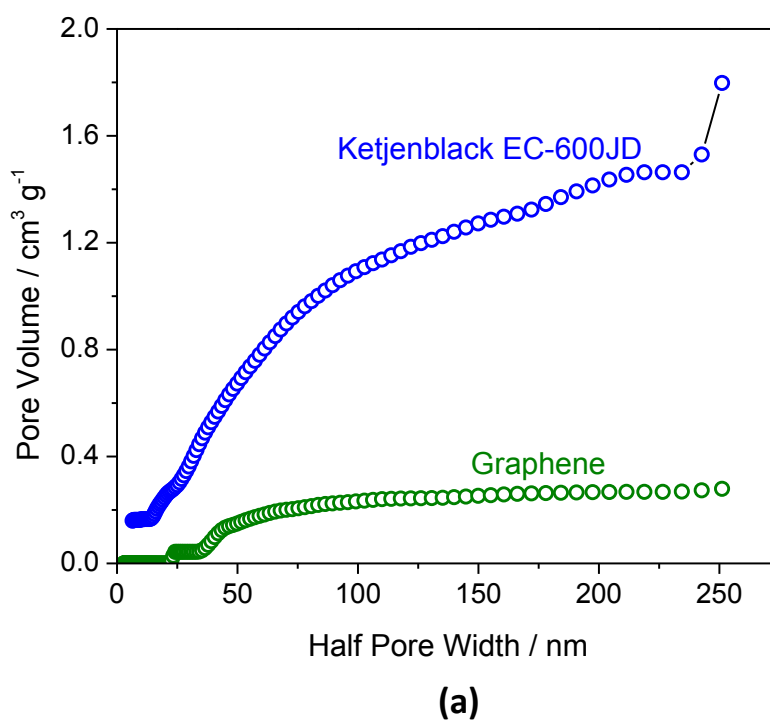
Results and Discussion

In this chapter, graphene is experimentally investigated as an alternative MPL material, and its suitability for PEM fuel cells is assessed through morphological, microstructural, physical and electrochemical characterization, and performance testing in a single and scaled-up fuel cell. Comparison studies are conducted with the MPL made of a conventional and frequently employed material, Ketjenblack. The observations obtained from the morphological, microstructural, physical, and electrochemical characterizations are utilized to explain the cell performances recorded for both the MPLs. The results obtained from the comparison studies are used to explain the main superiorities of the graphene-based MPL over the conventional MPLs.

5.1. Physical analysis of carbon powders

Brunauer-Emmett-Teller (BET) surface areas and pore-size distributions of graphene and Ketjenblack® EC-600JD powders are determined through

nitrogen physisorption analyses at -196°C by using a Quantachrome Autosorb-1 analyser. Prior to analyses, degassing is carried out at 130°C to remove any remaining moisture. These nitrogen adsorption and desorption measurements indicate that the surface areas of graphene and Ketjenblack[®] EC-600JD powders are $305.5\text{ m}^2/\text{g}$ and $1255.1\text{ m}^2/\text{g}$, respectively; clearly the BET surface area for Ketjenblack[®] EC-600JD powder is almost four times larger than that for the graphene, due to the tremendous difference in their structure. This dissimilarity is also clear on the difference in their pore volume and pore size distributions, as presented in Fig. 5.1.



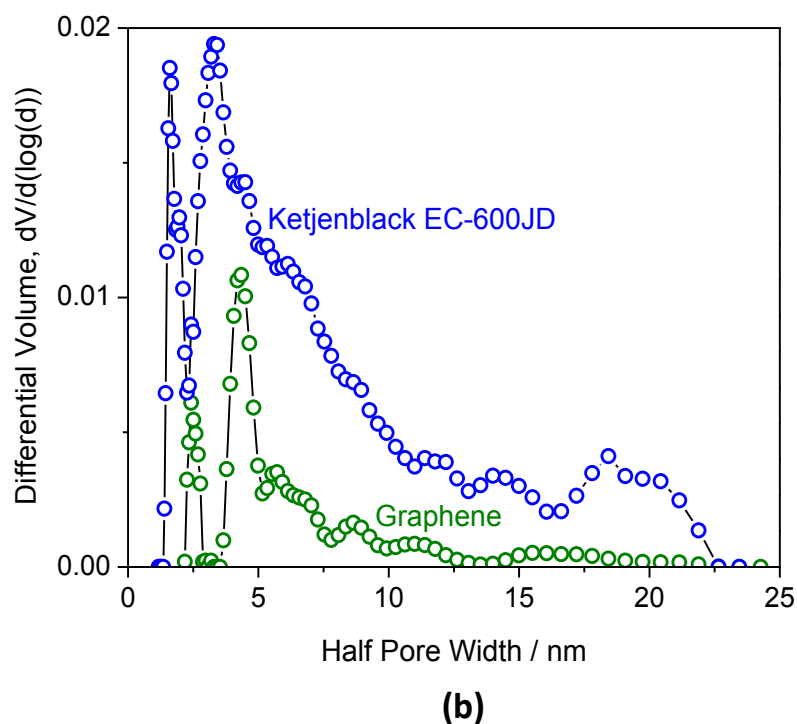


Figure 5.1: Pore size distribution of graphene and Ketjenblack[®] EC-600JD powders: (a) Cumulative pore volume distributions and (b) Differential pore volume distributions.

Ketjenblack[®] EC-600JD seems to be abundant with all pore sizes, with two special peaks: the first peak is located at a half pore width of 1.6 nm and the second one with a wider distribution has an average half pore width of 3.4 nm. These two peaks confirm the availability of higher micro- and meso-pore volumes, along with the relatively small volume of macropores. It can also be noted from Fig. 1(a) and Fig. 1(b) that graphene has a relatively small cumulative pore volume compared to Ketjenblack[®] EC-600JD, with special peaks at half pore widths of about 2.3 and 4.0 nm, indicating the higher mesoporosity of graphene.

5.2. Morphological and microstructural analyses of double-layer GDLs

5.2.1. Scanning electron microscopy analysis

The morphology and configuration of the double-layer GDLs and MPS (EP 40 Raw GDL, without MPL) are characterized through SEM analysis, and the micrographs of the surface and cross-sectional views of the MPS and double-layer GDLs are presented in Fig. 5.2.

As shown in Fig. 5.2(a) and Fig. 5.2(b), the MPS is made of cylindrical carbon fibres arranged or stacked randomly in the in- and through-plane directions, suggesting that the physical characteristics of the MPS, i.e., electrical and thermal conductivity, are anisotropic in the in- and through-plane directions. Further, the MPS possesses macro-scale open pores with sizes up to several-tens of micrometers (as clearly seen from Fig. 5.2(a)), indicating clearly that such an open space would substantially boost the electrical and thermal resistances between the interfaces of the CL/GDL and FFP/GDL [139]. The GDL with the graphene MPL (double-layer GDL), however, exhibits more uniform surface characteristics, with no visible surface crack but along with a small amount of graphene/PTFE agglomeration (see Fig. 5.2(c), inset). The graphene flakes build up a horizontally stacked and well-connected network, which is expected to provide good support for the mechanically weak CL, minimize the interfacial resistances, and improve catalyst utilization by preventing catalyst migration into the macropores of the MPS [52]. Further, the graphene MPL presents no clear boundary with the

MPS, and it is not simply deposited onto the surface of the MPS but, rather, penetrates partially into it (see Fig. 5.2(d)).

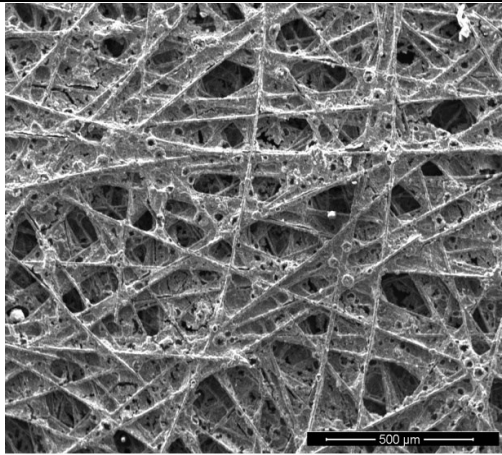
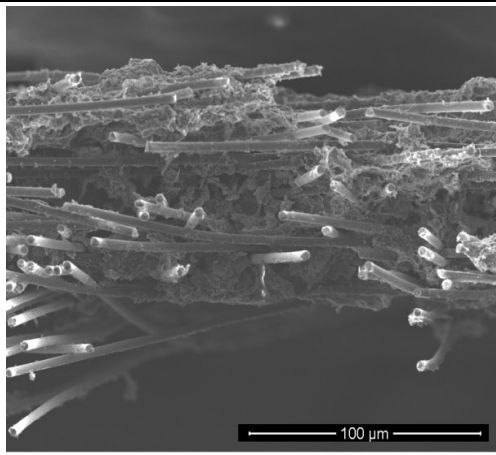
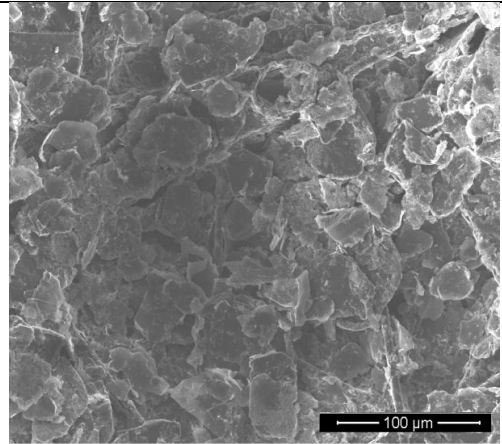
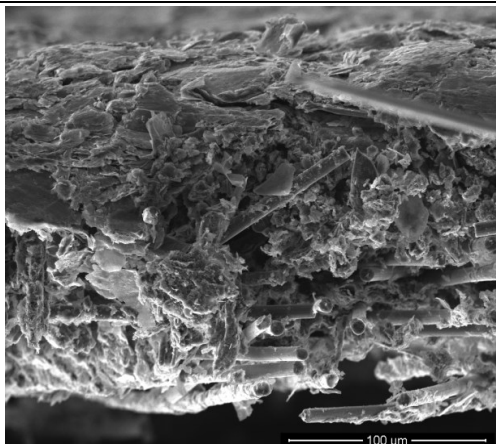
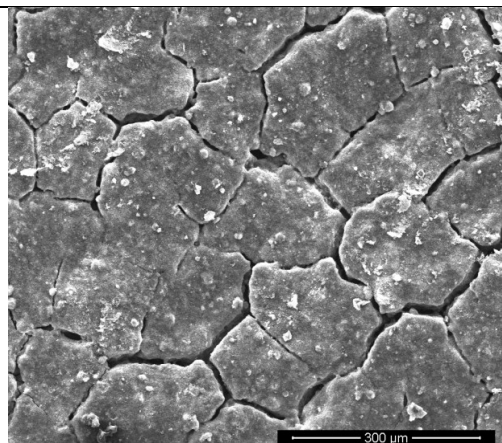
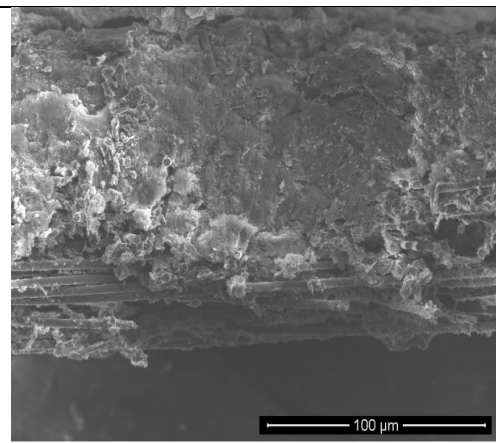
	Surface Morphology	Cross-sectional Morphology
Macroporous Substrate	 <p>(a)</p>	 <p>(b)</p>
Double-layer GDL based on graphene MPL	 <p>(c)</p>	 <p>(d)</p>
Double-layer GDL based on Ketjenblack EC-600JD MPL	 <p>(e)</p>	 <p>(f)</p>

Figure 5.2: Scanning electron microscopy (SEM) images of gas diffusion layers (GDLs): (a) top view of the macroporous substrate (MPS) (EP 40 Raw GDL, without microporous layer (MPL)), the image showing the macro-scale pores and interconnected network built up by the carbon fibers; (b) cross-sectional view of the MPS (EP 40 Raw GDL, without MPL); (c) top view of the double-layer GDL based on graphene MPL, the image showing the firmly and horizontally packaged graphene flakes; (d) cross-sectional view of the double-layer GDL based on graphene MPL, the image showing the graphene flakes penetrated into the MPS (EP 40 Raw GDL); (e) top view of the double-layer GDL based on Ketjenblack EC-600JD MPL, the image showing the interconnected and macro-scale surface cracks; (f) cross-sectional view of the double-layer GDL based on Ketjenblack EC-600JD MPL, the image showing the highly compact and composite-like cross-sectional morphology.

The MPL containing Ketjenblack® EC-600JD has a compact carbon structure, together with connected macro-crack networks; the cracks in the range of 10-20 μm wide (see Fig. 5.2(e)), and the crack networks resemble the Rayleigh-Bénard cell [140]. Compared with the graphene MPL, the Ketjenblack-MPL penetrates substantially into the MPS and forms an almost composite-like structure (see Fig. 5.2(f)). As a matter of fact, the full intrusion of the MPL materials into the MPS is expected to help achieve more isotropic physical and structural characteristics, i.e., more similar electrical and thermal conductivity, in both the in- and through-plane directions [139].

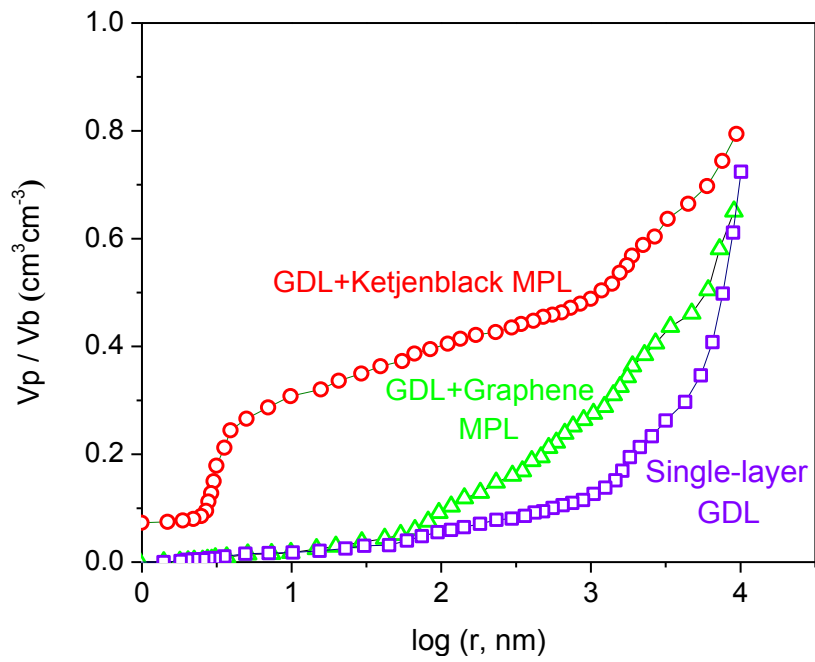
5.2.2. Porosimetry analysis

The pore characteristics obtained from the porosimetry analyses are given in both Fig. 5.3 and Table 5.1. To simplify the identification of the structural

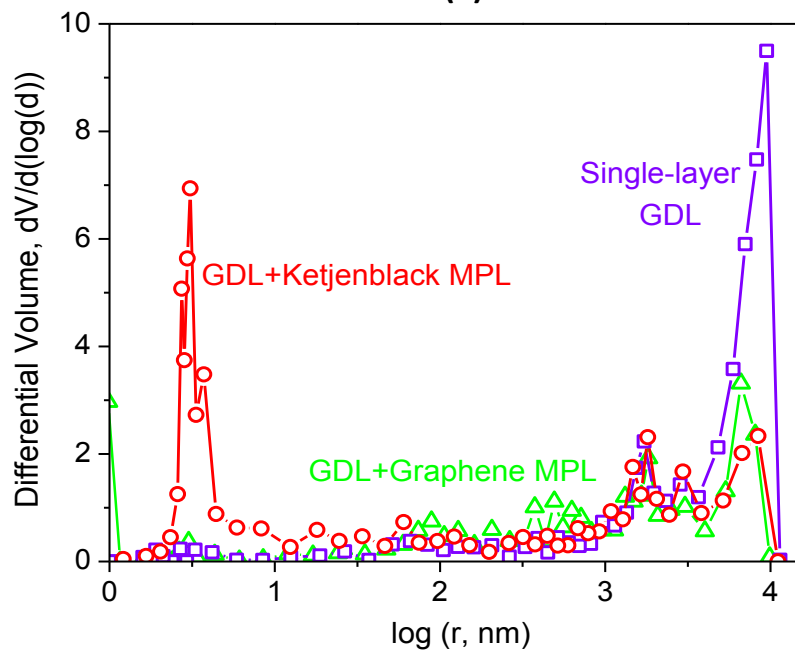
characteristics in different pore-size ranges and for the ease of discussion, the pores within the both the MPS and double-layer GDLs are classified into three categories: micropores with a pore diameter smaller than 0.07 μm , mesopores with a pore diameter range of 0.07-5 μm , and macropores with a pore diameter larger than 5 μm [141,142]. The present pore classification is based on the mechanism of the gas diffusion in the pore region: Knudsen diffusion dominates in the micropores, while bulk diffusion prevails in the macropores, whereas both Knudsen and bulk diffusion are present in the mesopores – such an approach is consistent with the practice in the fuel cell literature; for example, see [22,143,144].

As might be expected, the pore characteristics of the double-layer GDLs and those of the MPS are substantially different. For comparison, micro-, meso- and macro-pore volumes of the characterized samples are determined. For the MPS, approximately, 4% of the pore volume is in the micro-pore range, 31% is in the meso-pore range, and 38% is in the macro-pore range. Formation of the pores in the micro- and meso-pore ranges in the MPS could reasonably result from the small agglomerates of hydrophobic agent, whereas macropores are probably formed by the carbon fibres (see Fig. 5.2(a) and Fig. 5.2(b)). For the double-layer GDL with the graphene MPL, approximately, 6% of the pore volume is in the micro-pore range, 40% is in the meso-pore range, and 19% is in the macro-pore range. Compared with the MPS, the double-layer GDL with the graphene MPL contains more micro- and meso-pore volume, typically associated with the spaces formed by the graphene/hydrophobic agent agglomerates within the MPL, while the reduced volume of macropores may be attributable to the remaining pore space within the MPS (see Fig. 5.2(d)).

For the double-layer GDL with the Ketjenblack MPL, approximately, 37% of the pore volume is in the micro-pore range, 29% is in the meso-pore range, and 13% is in the macro-pore range. The significant increase in the micro-pore volume could be related to the spaces formed at the interfaces of the hydrophobic agent/Ketjenblack[®] EC-600JD powder/carbon fibers. It is noteworthy that when the MPL is made of Ketjenblack[®] EC-600JD powder, rather than graphene, the resulting micro-pore volume becomes significantly higher, likely related to the spherical and relatively small particles of Ketjenblack[®] EC-600JD (a primary particle size of 34 nm [144]), compared to graphene (30- μ m nominal particle size [145]). Herein, the micro- and macro-pore volume of the double-layer GDL with the Ketjenblack MPL could probably be formed by the spaces at the interfaces of carbon particle/hydrophobic agent/carbon fibers. Namely, the smaller the particle size of the carbon powder, the more micropores are formed. In addition, because of the smaller particle size of Ketjenblack[®] EC-600JD, the more open space within the MPS is filled (see Fig. 5.2(f)), which confirms the lower macro-pore volume (13%) of the double-layer GDL with the Ketjenblack MPL.



(a)



(b)

Figure 5.3: (a) Cumulative and (b) Differential pore size distribution in the macroporous substrate (MPS) (EP 40 Raw GDL, without microporous layer (MPL)) and double-layer GDLs based on either graphene or Ketjenblack MPL.

V_p denotes the pore volume; V_b represents the bulk volume; d is the pore diameter in nm; and r is the pore radius in nm.

Furthermore, as seen from Table 5.1, the thickness of the graphene MPL is only about 13-17 μm , which is distinctively small compared to that of the Ketjenblack MPL (97-103 μm), because as mentioned earlier, the nominal particle size for graphene is almost thousand times larger than that for Ketjenblack[®] EC-600JD, confirming the perceivable influence of carbon powder type on the physical characteristics achieved. Similarly, the physical characteristics of the carbon powders employed in the MPLs dramatically affect the overall pore characteristics of the double-layer GDLs (e.g., porosity, mean pore size, total surface area, and total pore volume). For instance, the porosity of the MPS (74%) slightly increases with the deposition of Ketjenblack MPL (79%), whereas it decreases with that of graphene MPL (65%).

Further, deposition of graphene MPL onto the MPS has no significant impact on the mean pore size, since the mean pore sizes of the MPS and double-layer GDLs are 162.4 and 190.5 nm, respectively; likely due to relatively less intrusion of the graphene MPL into the MPS, indicating the presence of macropores remaining within the MPS (see Fig. 5.2(d)). As mentioned, the graphene MPL presents a partial penetration into the MPS; thereby, the macropores pre-existing within the MPS still remain after MPL deposition, and thus still keeping the double-layer GDL's mean pore size close that of the MPS. This finding can also be corroborated by the small difference between the micro-pore volumes of the double-layer GDLs and MPS.

GDL type	MPL carbon powder type	MPL carbon loading (mg/cm ²)	MPL PTFE content (%)	MPL thickness (μm)	Bulk density (g/cm ³)	Porosity (%)	Mean pore size (nm)	Total surface area (cm ²)*	Total pore volume (cm ³)*
MPS	---	0	0	0	0.221	73	191	20691	0.099
Double-layer GDL	Graphene	2.0	20.0	13-17	0.303	65	162	25183	0.102
Double-layer GDL	Ketjenblack	2.0	20.0	97-103	0.228	79	22	344123	0.189

*Total surface area and pore volume values were obtained from two pieces of sample.

Table 5.1: Pore characteristics of the macroporous substrate (MPS, Avcarb EP 40, without MPL) and double-layer GDLs based on either graphene or Ketjenblack MPL.

5.3. Physical analysis of double-layer GDLs

5.3.1. Air permeability

The through-plane air permeability of a double-layer GDL depends markedly on its physical properties, such as porosity, mean pore diameter, and pore volume distribution [22]. In principle, an increase in the porosity, mean pore diameter, and macro-pore volume leads to a substantial enhancement in the through-plane air permeability [102]. The air permeabilities of the double-layer GDLs either with the graphene MPL or Ketjenblack MPL are presented in Table 5.2.

It is seen that with respect to the double-layer GDL with the Ketjenblack MPL, the one based on graphene MPL possesses substantially smaller air permeability (almost 20-30 times), which is a clear sign of presence of more resistance to air flow. This finding is also consistent with the pore characteristics obtained for the double-layer GDLs. As shown in Table 5.1, the double-layer GDL with graphene MPL has a relatively lower porosity (65%) than the one with the Ketjenblack MPL (79%), indicating the existence of more resistance to air flow. Further, the reduced air permeability with the deposition of graphene could also be associated with the graphene MPL's morphological structure, in which graphene flakes are horizontally and densely packaged (due to the two-dimensional structure of graphene), as noticed in Fig. 5.2(c) earlier. Such compact and stacked graphene flakes, positioned in the direction perpendicular to the air flow, could be one of the key contributors of the lower air permeability, because the presence of these flakes promotes considerable resistance to the air flow by forming tortuous air pathways.

In contrast, the double-layer GDL with the Ketjenblack MPL shows noticeably high air permeability (see Table 5.2), attributable to the presence of the macro-scale surface cracks (see Fig. 5.2(e)), forming relatively less tortuous air pathways.

5.3.2. Surface Wettability

The hydrophilic/hydrophobic characteristics of the double-layer GDLs are investigated via static contact angle measurements. As shown in Fig. 5.4, the double-layer GDL with the graphene MPL has a substantially higher static contact angle ($140\pm 3^\circ$), compared to that of the one with the Ketjenblack MPL ($116\pm 5^\circ$) (see also Table 5.2).

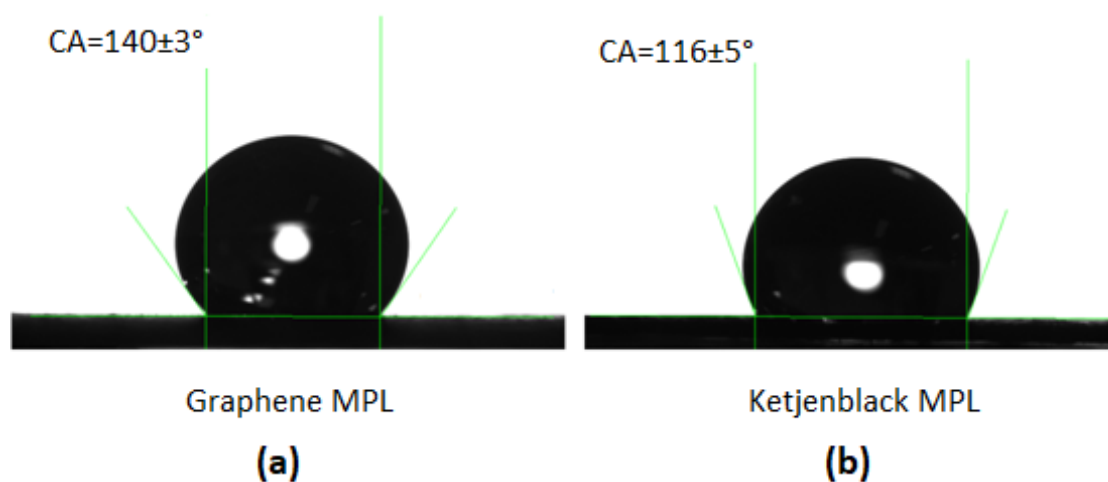


Figure 5.4: Static contact angles measured from the surfaces of (a) graphene microporous layer (MPL) and (b) Ketjenblack MPL.

It is interesting that although the micro-pore volume of the double-layer GDL with the graphene MPL (6%) is relatively low, compared to that of the one with the Ketjenblack MPL (37%), it exhibits a more-hydrophobic

behaviour. According to the Young-Laplace equation, the capillarity of a double-layer GDL is a strong function of micro-pore volume [146]. Herein, however, it seems that the physical properties of graphene and Ketjenblack® EC-600JD powders and surface characteristics of the double-layer GDLs are much more dominant. As already emphasized, the respective morphological characteristics of the graphene and Ketjenblack MPLs are quite dissimilar. Within the graphene MPL, the graphene flakes are horizontally stacked, promoting the formation of a relatively smooth surface (without any crack), and thus such as MPL allows water droplets to stay on its surface longer without any compromise in their spherical geometries. However, the water droplets dropped onto the surface of Ketjenblack MPL are prone to penetrate into the MPL, rather than remain on the surface, which is a clear indicator of the presence of the pathways for water removal, suggesting that this type of MPL will function better for water removal under high-humidity cell operation. This finding is also consistent with the SEM observations (see Fig. 5.2(e)).

In addition, the Ketjenblack MPL shows a greater variance in static contact angle ($116\pm 5^\circ$), compared to its graphene-based counterpart ($140\pm 3^\circ$). This variance could be attributable to the intrinsic surface characteristics (i.e., roughness and heterogeneity) of the Ketjenblack MPL (see Fig. 5.2(e)), since greatly varying hydrophobic/hydrophilic surface characteristics are observed depending on the position of the water droplets. In contrast, the double-layer GDL with the graphene MPL possesses more uniform wettability characteristics, along with a greater capability of retaining water on its surface, perhaps, due to the presence of fewer pathways for water removal, particularly within the regions near the surface, indicating that this type of

MPL will function better for water retention in low-humidity fuel cell operation.

5.3.3. In-plane electrical resistivity

As seen in Table 5.2, the double-layer GDL with the graphene MPL shows noticeably less resistivity (less than two times) to electron transport, compared to the one with the Ketjenblack MPL, in the in-plane direction. The in-plane electrical resistivity characteristics of the double-layer GDLs are significantly affected by the intrinsic particle properties of the employed graphene and Ketjenblack[®] EC-600JD powders and the interfaces between the agglomerated particles [147]. It is well established that graphene, by its very nature, possesses an unprecedentedly high single-particle conductivity ($\sim 10^8$ S/m), compared to Ketjenblack[®] EC-600JD ($\sim 10^3$ S/m), as reported in [147]. However, its electrical conductivity decreases substantially (up to 6 orders of magnitude), whereas that of Ketjenblack[®] EC-600JD decreases slightly (by a factor of 2), as the particles are in contact with each other as the bulk powder [147]. Even though graphene experiences a dramatic drop in its electrical conductivity when its particles are in contact with each other as the bulk powder, in this study, its capability of electron conduction within an MPL is found to be still as much as two times higher than that of Ketjenblack[®] EC-600JD, potentially attributable to the intrinsically high single-particle conductivity of graphene and the well-connected and more-direct network built up by the graphene flakes – this is quite desirable for effective electron transport.

Specifications of the double-layer GDLs							
GDL type	MPL carbon powder type	MPL carbon loading (mg/cm ²)	MPL PTFE content (%)	MPL thickness (μm)	Static contact angle (°)	In-plane electrical resistivity (mΩ cm)	Through-plane air permeability (m ²)
Double-layer GDL	Graphene	2.0	20.0	13-17	137-143	19.7 - 22.9	(2.93-3.25) × 10 ⁻¹⁴
Double-layer GDL	Ketjenblack	2.0	20.0	97-103	111-121	26.9 - 31.5	(4.22-9.88) × 10 ⁻¹³

Table 5.2: Physical characteristics of the double-layer GDLs based on either graphene or Ketjenblack MPL.

5.4. Electrochemical analysis of double-layer GDLs

5.4.1. Cyclic Voltammetry

To determine the ECSAs of the MEAs manufactured either with the graphene MPL or Ketjenblack MPL, *in-situ* CV is carried out under the same conditions: a cell temperature of 75°C, a back pressure of 35 kPag, and nitrogen and hydrogen relative humidities of 100%. The ECSA for each MEA is determined according to the columbic charge for hydrogen adsorption and desorption by using the equation given in Eq. (4.12).

Fig. 5.5 shows the cyclic voltammograms (CVs) for the hydrogen adsorption/desorption of the MEAs either with the graphene MPL or Ketjenblack MPL. It is seen that both the voltammograms yield the common graph shape for hydrogen adsorption and desorption peaks on platinum nanoparticles. Further, both the voltammograms capture virtually equal areas in the adsorption and desorption regions, potentially ascribed to the similarity in the MEA manufacturing process, since both the MEAs are manufactured from the same catalyst and ionomer made with the same ink specifications. However, the ECSA calculated for the MEA with the graphene MPL and Ketjenblack MPL are 80 m²/g and 79 m²/g, respectively; the ECSA for the former is slightly higher than that for the latter. Because the method of catalyst-coated membrane (CCM) is applied in the fabrication of both the MEAs, the effect of catalyst penetration into the double-layer GDLs may be assumed to be negligible and cannot explain the difference between the ECSAs. The root causes of the higher ECSA calculated for the MEA assembled with the graphene MPL could be relatively faster electron transport and a higher degree of surface contact between the graphene MPL and CCL. As

mentioned previously, the electrical conductivity of the graphene MPL is almost twice that of the Ketjenblack MPL; potentially accelerating hydrogen desorption reaction by providing comparatively faster electron transport. The graphene MPL also presents a quite uniform and unique morphology, in which graphene flakes are horizontally and firmly packaged (see Fig. 5.2(c)), probably offering a smooth layer (thus a relatively higher degree of surface contact), improving catalyst activity.

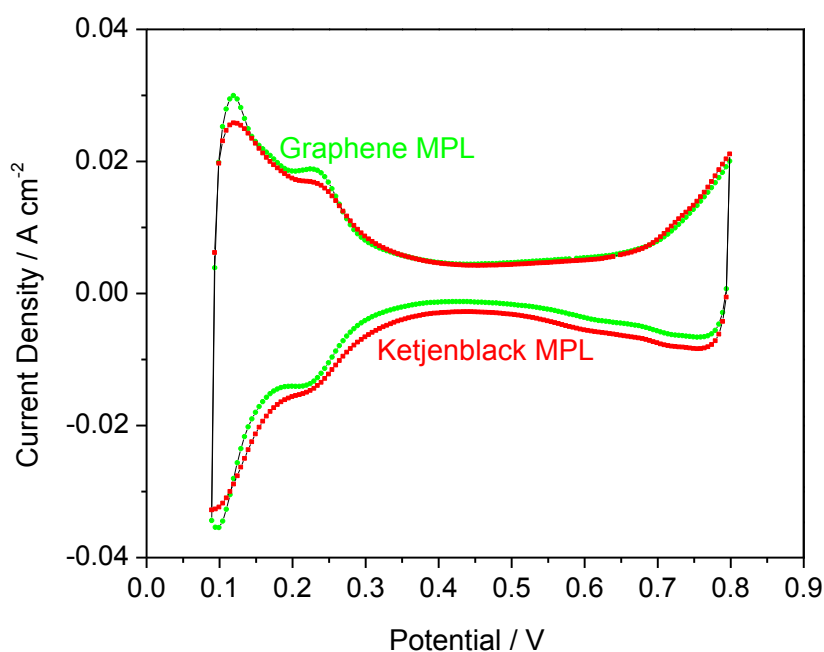


Figure 5.5: Cyclic voltammograms (CVs) for the membrane-electrode assemblies (MEAs) based on either graphene microporous layer (MPL) or Ketjenblack MPL. Operating temperature: 75°C; nitrogen and hydrogen back pressures: 35 kPag; and nitrogen and hydrogen relative humidity of 100%.

Platinum utilization for the each MEA is also calculated to understand the potential impact of the employed MPL on catalyst utilization by using the CV

data and the size of the Pt nanoparticles. As noted, platinum utilization for the each MEA is estimated from the ratio of the ECSA over the theoretical geometric surface area (ECSA calculated) of the platinum nanoparticles. It is found that the platinum utilization for the graphene MPL and Ketjenblack MPL are 84% and 83%, respectively; suggesting clearly that the characteristics of the MPL has a mentionable impact on catalyst activity and platinum utilization.

5.5. Single-cell performance analyses of double-layer GDLs

The electrochemical assessment of the double-layer GDLs in a single cell provides practical insights into the viability of the materials (i.e., graphene) for the constituents (i.e., MPL) under actual operating conditions [98]. Thus, the steady-state current-voltage curves (I-V) of the double-layer GDLs based on either graphene MPL or Ketjenblack MPL are obtained in a scaled-up single cell with an electrode geometric area of 45 cm² under the same operating conditions: varied air and hydrogen relative humidities (40% RH, 70%RH, and 100%RH), varied pressures (35 kPag, 100 kPag, and 150 kPag), a constant temperature of 75°C, and constant anode and cathode flow rates of 4.45 and 9.00 l/min, respectively.

Fig. 5.6(a) and Fig. 5.6(b) display the variation in the polarization curves of the double-layer GDLs constructed with the graphene MPL and Ketjenblack MPL with altering air and hydrogen relative humidities (40% RH, 70% RH, and 100% RH). The performance characteristics of the double-layer GDLs, as evident from Fig. 5.6 demonstrate great variations, specifically in ohmic and mass transport polarization dominant regions, with varying humidification level of the air and hydrogen streams. Hence, the level of humidification in

the air and hydrogen streams dramatically affects the internal cell resistance and mass transport [149]. Obviously, under low-humidity operation (40% RH), the graphene MPL exhibits superior performance with a peak power density of 0.62 W/cm² than the Ketjenblack MPL (0.40 W/cm²), which corresponds to a performance improvement of ~53%.

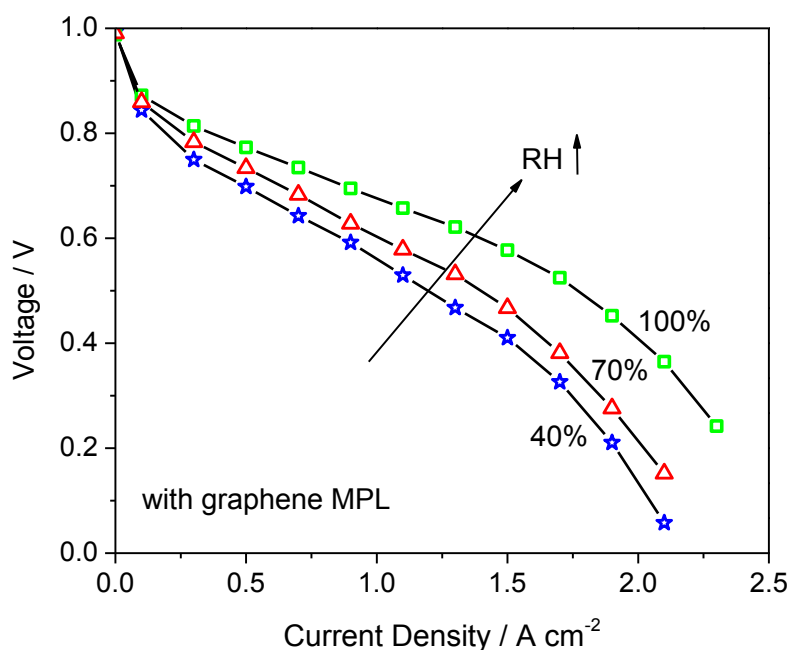
The superior performance of the graphene MPL under low-humidity operation could likely to its morphology. As previously discussed, graphene MPL basically consists of densely and horizontally packaged graphene flakes with no visible crack (see Fig. 5.2(c)). Such a dense and continuous layer seems to create a significant resistance to the water removal from the interface of membrane/CL, thus maintaining a more effective balance between two reverse running water transport mechanisms, electro-osmotic drag and back diffusion. A more effective balance between these mechanisms potentially induces retaining water within the three-phase boundary, thus eliminating the performance deterioration arising from drying out of the membrane.

In contrast, the Ketjenblack MPL seems leading to severe membrane dehydration under low-humidity operation, stemming mainly from its cracked morphology (see Fig. 5.2(e)) through which by-product water can simply be transported away from the CL/membrane interface by the pressure caused by membrane swelling [150]. In this case, there is no effective balance between electro-osmotic drag and back-diffusion, and thus the membrane is no more capable of maintaining a desirable hydration level for effective proton conduction.

However, when the humidification level increased from 40% RH to 70% RH, the peak power densities obtained for both the graphene and Ketjenblack

MPLs also increase from 0.62 W/cm^2 to 0.70 W/cm^2 and 0.40 W/cm^2 to 0.67 W/cm^2 (see Fig. 5.7), respectively; a finding likely induced by further enhancement in the membrane hydration level. Herein, it is noteworthy that the increase in the peak power density of the Ketjenblack MPL is quite high ($\sim 66.6\%$), compared to the one based on graphene ($\sim 13.9\%$), consistent with the previous discussion.

For further increase of the humidification level, the Ketjenblack MPL presents a continuous improvement; more specifically, its peak power density increases from 0.67 W/cm^2 to 0.89 W/cm^2 , equivalent to an improvement of $\sim 32.7\%$. The graphene MPL also exhibits an enhancement in performance, with a peak power density of $\sim 23.6\%$, but still remains smaller compared to the performance enhancement of the Ketjenblack MPL (see Fig. 5.7). Herein, under high-humidity operation (i.e., 100% RH), the graphene MPL seems to have limitations in reference to water removal, leading to blockage of electrochemically active regions and deteriorating overall cell performance.



(a)

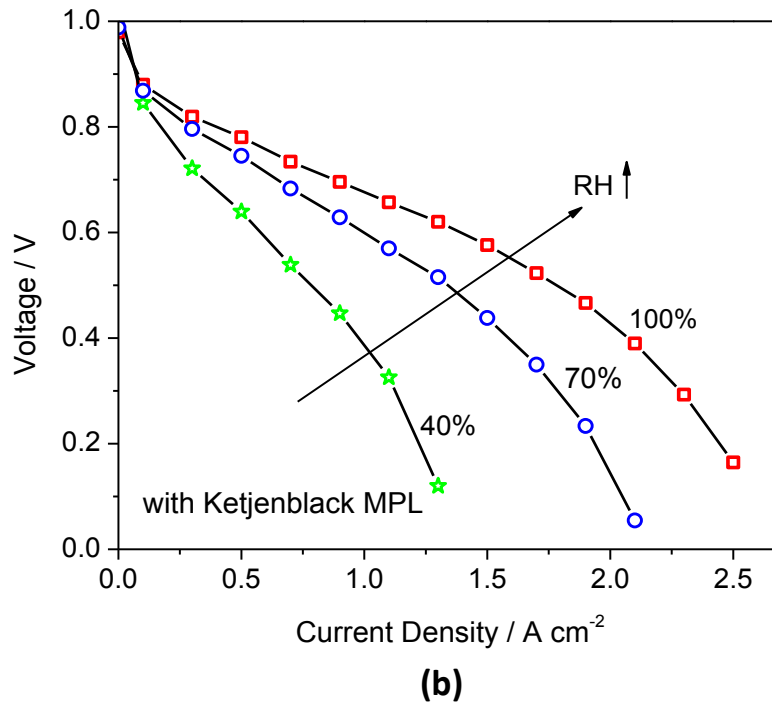


Figure 5.6: Polarization curves obtained from the membrane-electrode assemblies (MEAs) either with the (a) graphene MPL or (b) Ketjenblack MPL under various relative humidities (RHs) of air and hydrogen streams. Operating temperature: 75°C, hydrogen and air back pressures: 35 kPag, and hydrogen and air flow rates: 4.45 and 9.00 l/min.

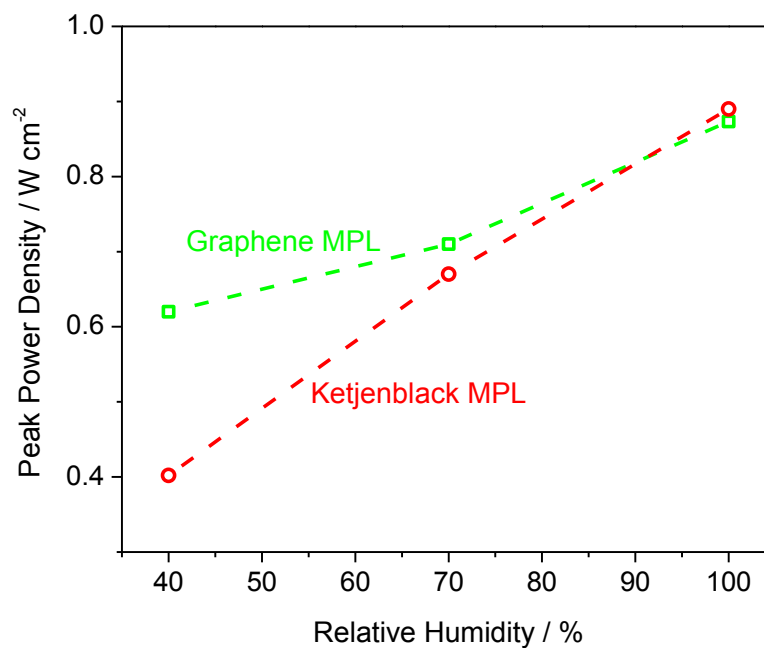
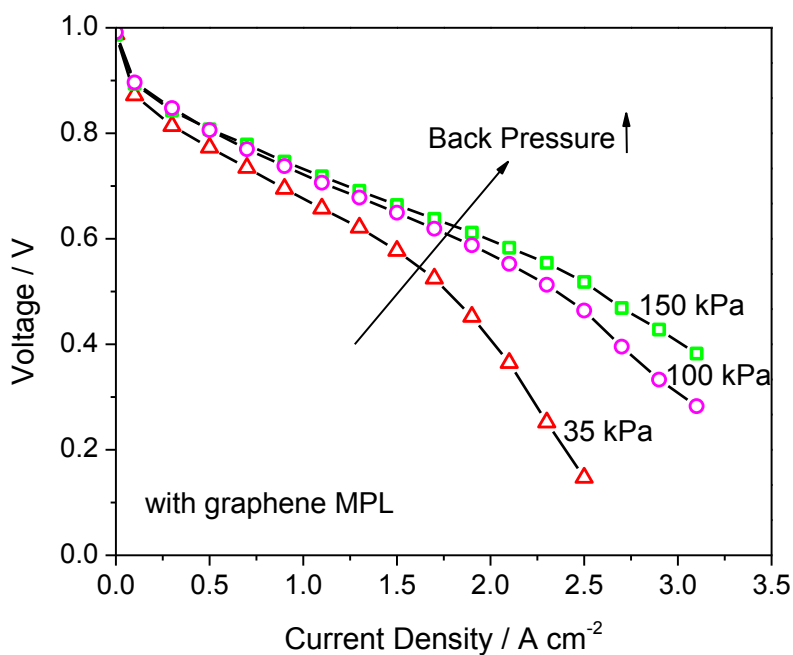


Figure 5.7: Peak power densities obtained from the membrane-electrode assemblies (MEAs) either with the graphene microporous layer (MPL) or Ketjenblack MPL under various relative humidities (RHs) of air and hydrogen streams. Operating temperature: 75°C, hydrogen and air back pressures: 35 kPag, and hydrogen and air flow rates: 4.45 and 9.00 l/min.

Fig. 5.8(a) and Fig. 5.8(b) present the change in the polarization curves of the double-layer GDLs assembled either with the graphene MPL and Ketjenblack MPL with varying back pressures of air and hydrogen streams. It is clear that cell performances of both the double-layer GDLs demonstrate significant improvements, especially in the ohmic and mass transport polarization dominant regions of the polarization curves, with the increase in pressures of the gas streams. The increased pressure is also found to have a slight influence on the OCVs recorded for the cells. The relatively low OCVs and performance characteristics achieved under comparatively low-pressure operation (35 kPag) could be mainly ascribed to the water flooding and reactant starvation. In particular, under low-pressure operation, the reactants may not be homogeneously distributed over their respective electrochemical reaction region, likely ascribed to two well-established phenomena [151]. The first being that under low-pressure operation, in contrast to the high-pressure operation, high amount of water is required to provide saturation of the air and hydrogen streams, facilitating the accumulation of excessive amount of water within the three-phase boundary, decreasing catalyst utilization and exacerbating activation overpotential. The second one, however, is the relatively lower partial pressures of the reactants along the flow channels [152]. The compound effect of lower reactant partial pressure and excessive water accumulation potentially inhibits the effective mass transport to the

three-phase boundary through the void regions of the double-layer GDLs, increasing the activation overpotential and thus deteriorating cell performance. The combination of these two effects leads to performance limitations, specifically for the MPLs having advanced water retaining capability together with relatively low porosity and air permeability, i.e., the graphene MPL, rather than those having comparatively high air permeability, porosity, and water expelling characteristics, i.e., the Ketjenblack MPL (see also Table 5.1 and Table 5.2). More specifically, the graphene MPL demonstrate a greater performance enhancement (a peak power density improvement of ~32.3%), compared to the Ketjenblack MPL (~27.5%). The relatively more performance improvement obtained for the graphene MPL confirms that the relatively lower porosity and air permeability and more condensed morphology of the graphene MPL induces slight deterioration in performance, specifically under low-pressure (35 kPag) and high humidity (100% RH) operation.



(a)

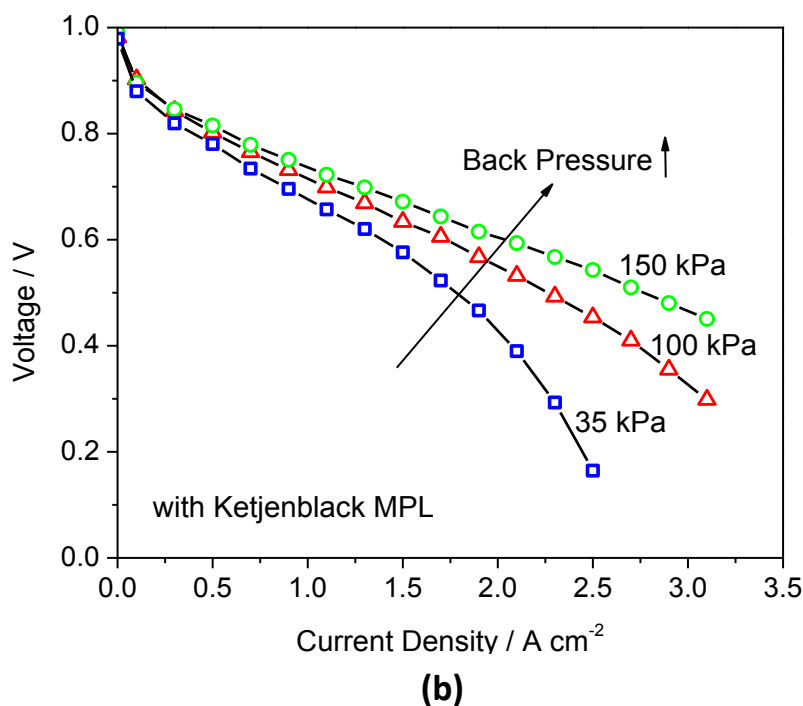


Figure 5.8: Polarization curve obtained from the membrane-electrode assemblies (MEAs) either with the (a) graphene microporous layer (MPL) or (b) Ketjenblack MPL under various back pressures of air and hydrogen streams. Operating temperature: 75°C, relative humidities (RHs) of air and hydrogen streams: 100%, and flow rates of hydrogen and air streams: 4.45 and 9.00 l/min.

Nevertheless, for both the graphene and Ketjenblack MPLs, high-pressure operation seems to minimize the performance limitations associated with the water flooding and reactant starvation (see Fig. 5.9), since it is a condition requiring less water for the saturation of gas streams [152], contributing effective humidification of the three-phase boundary without excessive water accumulation. Aside from these benefits, high-pressure operation may also improve the electrochemical reaction kinetics by allowing supply of the reactants to the three-phase boundary with a relatively higher concentration,

which is particularly desirable for a faster oxygen reduction occurring at the cathode [151].

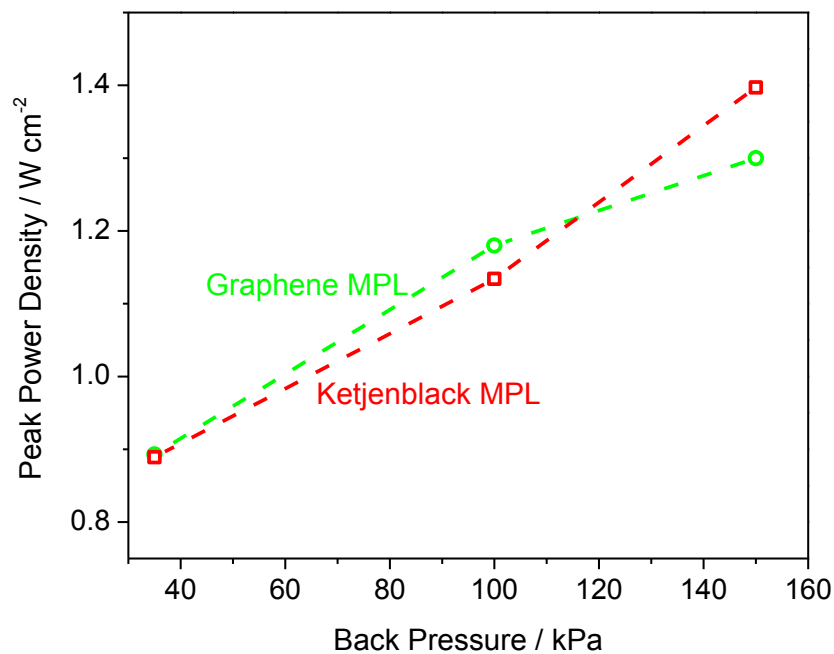


Figure 5.9: Peak power densities obtained from the membrane-electrode assemblies (MEAs) either with the graphene microporous layer (MPL) or Ketjenblack MPL under various back pressures of air and hydrogen air streams. Operating temperature: 75°C, air and hydrogen relative humidities of 100%, and hydrogen and air flow rates of 4.45 and 9.00 l/min.

Chapter 6

Conclusions and Recommendations

6.1. Conclusions

In this thesis research, a novel application of graphene as a microporous layer (MPL) material for proton exchange membrane (PEM) fuel cells is investigated. The motivation of investigating graphene as an alternative MPL material originates from graphene's unique characteristics, such as excellent charge mobility (and hence extremely high single-particle electrical conductivity), high thermal conductivity, adequate mechanical properties (i.e., high elasticity and mechanical stiffness). Besides these features, graphene flakes are prone to build up a well-packaged smooth layer, which could act as a pressure valve and facilitate water preservation, in particular under low-humidity conditions. In the scope of this thesis, graphene is investigated as an

alternative MPL material by following the methodology summarized as follows.

To gain a comprehensive understanding of the physical characteristics (i.e., Brunauer-Emmett-Teller (BET)) surface areas and pore size distributions) of the graphene powder investigated in this study, nitrogen physisorption analyses are conducted. Thereafter, a graphene-based MPL (graphene MPL) is spray-deposited onto the MPS (i.e., Avcarb EP40 carbon paper), and the resulting double-layer GDL (after MPL is deposited on) is extensively characterized to reveal its many under-explored morphological, structural, physical, and electrochemical characteristics. For electrochemical assessment of the double-layer GDL in a single PEM fuel cell, the membrane-electrode assembly (MEA) based on the graphene MPL is fabricated by the method of catalyst coated membrane (CCM). In the MEA, the anode double-layer GDL is kept constant as the commercially available carbon paper (Avcarb GDS 3250, with MPL), while the cathode GDL is employed as the graphene MPL based double-layer GDL – namely, the double-layer GDL based on graphene MPL is investigated for the cathode side. Single cell performance characteristics of the graphene MPL is also investigated for the first time in a scaled-up cell (with an electrode geometric area of 45 cm²) under different back pressures and relative humidities of air and hydrogen streams. To determine the impact of graphene MPL on the electrochemical surfaces areas (ECSAs) and platinum utilization of the membrane-electrode assemblies (MEAs), in-situ cyclic voltammetry (CV) analysis is performed via a commercial fuel cell test station, equipped with a frequency response analyzer. For comparison purposes, all these analyses are also performed for the double-layer GDL constructed with the MPL made of commercial carbon

powder, Ketjenblack® EC-600JD, and this MPL is identified as Ketjenblack MPL in this thesis.

In summary, even though the graphene MPL takes up a relatively small fraction of the overall thickness of the double-layer GDL (~10%), it has a disproportionately important influence on cell performance, owing to its favorable morphological characteristics. The graphene MPL, in which graphene flakes are horizontally and densely packaged, presents almost two times less electrical resistivity (or electron transport capability), compared to the Ketjenblack MPL. This higher electrical conductivity is potentially due to graphene's extremely high single-particle conductivity as well as bulk conductivity when its particles are in direct contact as a powder. Owing to the two-dimensional structure of graphene flakes, they tend to build up a well-connected network as they are deposited onto the MPS surface. Such a unique morphology leads to formation of relatively fewer water pathways, contributing considerably to MPL's advanced water retaining capability. With the application of the graphene MPL, mentionable improvements in both the ECSAs and catalyst utilization are noted.

Owing to all these desirable characteristics, substantial performance superiorities (up to a peak power density superiority of ~53) over the Ketjenblack MPL are achieved, particularly when the cell is operated under low- and intermediate-humidity conditions. In accordance with these findings, it may be understood that deposition of graphene MPL onto the MPS emerges many favorable characteristics that thoroughly boost cell performance, in particular under low- and intermediate-humidity operation. In brief, the methodology followed in this thesis is believed to be conducive to

facilitating alleviation of performance limitations, i.e., severe performance deteriorations under low- and intermediate-humidity operation, resulting mainly from the use of conventional carbon-based nanomaterials in the fabrication of MPLs.

6.2. Recommendations

The criticality of MPL, as a key constituent that play primary roles in operation by substantially affecting mass, heat, and electricity transport, as well as in overall technology cost by offering an opportunity to eliminate the use of an external humidifier, has become clearer. The effectiveness of an MPL in all these potential attributes depends to a large extent on its morphological, microstructural, physical and electrochemical characteristics; which are all in turn a strong function of its material and design specifications. Thus, the properties of selected material and design are of paramount importance. The greatest contribution of this thesis is to investigate graphene extensively as an alternative MPL material, and to report its performance-enhancing features over a wide range of cell operation when it is employed in MPLs. This is particularly useful for improving cell performance, especially under low- and intermediate humidity conditions. However, graphene is a yet-to-be-developed class of material, so its absolute viability as an alternative MPL material for fuel cells has not been proven yet. Thus, future work to further evaluate graphene's suitability for MPLs can be summarized as follows.

1. Optimization of design parameters of graphene-based MPLs (such as type and loading of graphene, type and loading of hydrophobic agent loading, parameters, conditions, and specifications of MPL ink preparation and drying and sintering processes).

2. To make the optimization of the graphene-based MPLs cost-effective, modeling and simulation studies should be conducted, because there is currently a significant room for modeling and/or simulation studies focusing on graphene-based MPLs. On completion of optimization of design parameters, further investigation into the morphological, microstructural, physical, and electrochemical characterization of the optimized MPLs should be performed.

3. Short- and long-term performance characteristics of the graphene-based MPLs should be conducted, and the obtained characteristics should be compared with the future targets established by the United States Department of Energy (DOE).

4. Cell performances of the graphene-based MPLs have been investigated in the open literature, particularly for small-size cells (i.e., with an electrode geometric active area of 5 cm²), and there is currently a room for large-cell performance investigation.

5. Cell performances of the graphene-based MPLs should also be confirmed for stack-level applications – this requires stack-level performance investigations.

References

- [1] Gür TM. Comprehensive review of methane conversion in solid oxide fuel cells: Prospects for efficient electricity generation from natural gas. *Progress in Energy and Combustion Science* 2016;54:1–64. doi:10.1016/j.pecs.2015.10.004.
- [2] Adnan Ozden, Ibrahim E. Alaefour, Samaneh Shahgaldi, Xianguo Li, C. Ozgur Colpan and Feridun Hamdullahpur, Chapter 2.28 - Gas Diffusion Layers for PEM Fuel Cells: Ex- and In-Situ Characterization, In *Exergetic, Energetic and Environmental Dimensions* 2018, Pages 695-727. <https://doi.org/10.1016/B978-0-12-813734-5.00040-8>.
- [3] Bajpai P, Dash V. Hybrid renewable energy systems for power generation in stand-alone applications: A review. *Renewable and Sustainable Energy Reviews* 2012;16:2926–2639. doi:10.1016/j.rser.2012.02.009.
- [4] Luo Y, Jiao K. Cold start of proton exchange membrane fuel cell. *Progress in Energy and Combustion Science* 2018;64:29–61. doi:10.1016/j.pecs.2017.10.003.
- [5] Wang Y, Chen KS, Mishler J, Cho SC, Adroher XC. A review of polymer electrolyte membrane fuel cells: Technology, applications, and needs on fundamental research. *Applied Energy* 2011;88:981–1007. doi:10.1016/j.apenergy.2010.09.030.
- [6] Lanzini A, Madi H, Chiodo V, Papurello D, Maisano S, Santarelli M, Vanherle J. Dealing with fuel contaminants in biogas-fed solid oxide fuel cell (SOFC) and molten carbonate fuel cell (MCFC) plants: Degradation of catalytic and electro-catalytic active surfaces and related

- gas purification methods. *Progress in Energy and Combustion Science* 2017;61:150–88. doi:10.1016/j.pecs.2017.04.002.
- [7] Jiao K, Li X. Water transport in polymer electrolyte membrane fuel cells. *Progress in Energy and Combustion Science* 2011;37:221–91. doi:10.1016/j.pecs.2010.06.002.
- [8] Ozden A, Shahgaldi S, Li X, Hamdullahpur F. A graphene-based microporous layer for proton exchange membrane fuel cells: Characterization and performance comparison. *Renewable Energy* 2018;126:485–94. doi:10.1016/j.renene.2018.03.065.
- [9] Wu H. Mathematical Modeling of Transient Transport Phenomena in PEM Fuel Cells. Phd Thesis, University of Waterloo, 2009:188.
- [10] Zamel N, Li X. Effective transport properties for polymer electrolyte membrane fuel cells - With a focus on the gas diffusion layer. *Progress in Energy and Combustion Science* 2013;39:111–46. doi:10.1016/j.pecs.2012.07.002.
- [11] Tsushima S, Hirai S. In situ diagnostics for water transport in proton exchange membrane fuel cells. *Progress in Energy and Combustion Science* 2011;37:204–20. doi:10.1016/j.pecs.2010.06.001.
- [12] Zhao TS, Xu C, Chen R, Yang WW. Mass transport phenomena in direct methanol fuel cells. *Progress in Energy and Combustion Science* 2009;35:275–92. doi:10.1016/j.pecs.2009.01.001.
- [13] Zamel N, Li X. Effect of contaminants on polymer electrolyte membrane fuel cells. *Progress in Energy and Combustion Science* 2011;37:292–329. doi:10.1016/j.pecs.2010.06.003.
- [14] Ozden A, Ercelik M, Devrim Y, Colpan CO, Hamdullahpur F. Evaluation of sulfonated polysulfone/zirconium hydrogen phosphate composite membranes for direct methanol fuel cells. *Electrochimica Acta* 2017;256:196–210. doi:10.1016/j.electacta.2017.10.002.
- [15] Jeon DH, Kim KN, Baek SM, Nam JH. The effect of relative humidity of the cathode on the performance and the uniformity of PEM fuel cells. *International Journal of Hydrogen Energy* 2011;36:12499–511. doi:10.1016/j.ijhydene.2011.06.136.

- [16] Yablecki J, Nabovati a., Bazylak a. Modeling the Effective Thermal Conductivity of an Anisotropic Gas Diffusion Layer in a Polymer Electrolyte Membrane Fuel Cell. *Journal of The Electrochemical Society* 2012;159:B647. doi:10.1149/2.013206jes.
- [17] Sadeghifar H, Djilali N, Bahrami M. Effect of Polytetrafluoroethylene (PTFE) and micro porous layer (MPL) on thermal conductivity of fuel cell gas diffusion layers: Modeling and experiments. *Journal of Power Sources* 2014;248:632–41. doi:10.1016/j.jpowsour.2013.09.136.
- [18] Ozden A, Ercelik M, Ozdemir Y, Devrim Y, Colpan CO. Enhancement of direct methanol fuel cell performance through the inclusion of zirconium phosphate. *International Journal of Hydrogen Energy* 2017;1–17. doi:10.1016/j.ijhydene.2017.01.188.
- [19] Carton JG, Lawlor V, Olabi AG, Hochenauer C, Zauner G. Water droplet accumulation and motion in PEM (Proton Exchange Membrane) fuel cell mini-channels. *Energy* 2012;39:63–73. doi:10.1016/j.energy.2011.10.023.
- [20] Rezaei Niya SM, Hoorfar M. Study of proton exchange membrane fuel cells using electrochemical impedance spectroscopy technique - A review. *Journal of Power Sources* 2013;240:281–93. doi:10.1016/j.jpowsour.2013.04.011.
- [21] Li X. *Principles of fuel cells*. Taylor & Francis; 2005.
- [22] Tseng C-J, Lo S-K. Effects of microstructure characteristics of gas diffusion layer and microporous layer on the performance of PEMFC. *Energy Conversion and Management* 2010;51:677–84. doi:10.1016/j.enconman.2009.11.011.
- [23] Jiao K, Park J, Li X. Experimental investigations on liquid water removal from the gas diffusion layer by reactant flow in a PEM fuel cell. *Applied Energy* 2010;87:2770–7. doi:10.1016/j.apenergy.2009.04.041.
- [24] Thomas YRJ, Benayad A, Schroder M, Morin A, Pauchet J. New Method for Super Hydrophobic Treatment of Gas Diffusion Layers for Proton Exchange Membrane Fuel Cells Using Electrochemical Reduction of Diazonium Salts. *ACS Applied Material Interfaces* 2015;7:15068–77. doi:10.1021/acsami.5b04428.

- [25] Zamel N. Transport Properties of the Gas Diffusion Layer of PEM Fuel Cells. Phd Thesis, University of Waterloo, 2011.
- [26] He G, Yamazaki Y, Abudula A. A three-dimensional analysis of the effect of anisotropic gas diffusion layer(GDL) thermal conductivity on the heat transfer and two-phase behavior in a proton exchange membrane fuel cell (PEMFC). *Journal of Power Sources* 2010;195:1551–60. doi:10.1016/j.jpowsour.2009.09.059.
- [27] Vikram A, Chowdhury PR, Phillips RK, Hoorfar M. Measurement of effective bulk and contact resistance of gas diffusion layer under inhomogeneous compression - Part I: Electrical conductivity. *Journal of Power Sources* 2016;320:274–85. doi:10.1016/j.jpowsour.2016.04.110.
- [28] Roy Chowdhury P, Vikram A, Phillips RK, Hoorfar M. Measurement of effective bulk and contact resistance of gas diffusion layer under inhomogeneous compression - Part II: Thermal conductivity. *Journal of Power Sources* 2016;320:222–30. doi:10.1016/j.jpowsour.2016.04.112.
- [29] Park S, Lee JW, Popov BN. Effect of PTFE content in microporous layer on water management in PEM fuel cells. *Journal of Power Sources* 2008;177:457–63. doi:10.1016/j.jpowsour.2007.11.055.
- [30] Tsai JC, Lin CK. Effect of PTFE content in gas diffusion layer based on Nafion®/PTFE membrane for low humidity proton exchange membrane fuel cell. *Journal of the Taiwan Institute of Chemical Engineers* 2011;42:945–51. doi:10.1016/j.jtice.2011.05.008.
- [31] Park S, Lee JW, Popov BN. A review of gas diffusion layer in PEM fuel cells: Materials and designs. *International Journal of Hydrogen Energy* 2012;37:5850–65. doi:10.1016/j.ijhydene.2011.12.148.
- [32] Oedegaard A, Hebling C, Schmitz A, Møller-Holst S, Tunold R. Influence of diffusion layer properties on low temperature DMFC. *Journal of Power Sources* 2004;127:187–96. doi:10.1016/j.jpowsour.2003.09.015.
- [33] Sarkar J, Bhattacharyya S. Operating characteristics of transcritical CO₂ heat pump for simultaneous water cooling and heating. *Archives Thermodynamics* 2012;33:23–40. doi:10.1002/er.

- [34] Chen R, Zhao TS. A novel electrode architecture for passive direct methanol fuel cells. *Electrochemistry Communications* 2007;9:718–24. doi:10.1016/j.elecom.2006.11.004.
- [35] Frey T, Linardi M. Effects of membrane electrode assembly preparation on the polymer electrolyte membrane fuel cell performance. *Electrochimica Acta* 2004;50:99–105. doi:10.1016/j.electacta.2004.07.017.
- [36] Wang Y, Wang CY, Chen KS. Elucidating differences between carbon paper and carbon cloth in polymer electrolyte fuel cells. *Electrochimica Acta* 2007;52:3965–75. doi:10.1016/j.electacta.2006.11.012.
- [37] Morgan JM, Datta R. Understanding the gas diffusion layer in proton exchange membrane fuel cells. I. How its structural characteristics affect diffusion and performance. *Journal of Power Sources* 2014;251:269–78. doi:10.1016/j.jpowsour.2013.09.090.
- [38] Lopicque F, Belhadj M, Bonnet C, Pauchet J, Thomas Y. A critical review on gas diffusion micro and macroporous layers degradations for improved membrane fuel cell durability. *Journal of Power Sources* 2016;336:40–53. doi:10.1016/j.jpowsour.2016.10.037.
- [39] Unsworth G. Measurement and Characterization of Heat and Mass Diffusion in PEMFC Porous Media. MASC thesis, University of Waterloo, 2012.
- [40] Park S, Popov BN. Effect of cathode GDL characteristics on mass transport in PEM fuel cells. *Fuel* 2009;88:2068–73. doi:10.1016/j.fuel.2009.06.020.
- [41] Sadeghifar H, Djilali N, Bahrami M. Thermal conductivity of a graphite bipolar plate (BPP) and its thermal contact resistance with fuel cell gas diffusion layers: Effect of compression, PTFE, micro porous layer (MPL), BPP out-of-flatness and cyclic load. *Journal of Power Sources* 2015;273:96–104. doi:10.1016/j.jpowsour.2014.09.062.
- [42] Su H, Pasupathi S, Bladergroen B, Linkov V, Pollet BG. Optimization of gas diffusion electrode for polybenzimidazole-based high temperature proton exchange membrane fuel cell: Evaluation of polymer binders in catalyst layer. *International Journal of Hydrogen Energy* 2013;38:11370–8. doi:10.1016/j.ijhydene.2013.06.107.

- [43] Park SB, Park Y Il. Fabrication of gas diffusion layer (GDL) containing microporous layer using fluorinated ethylene propylene (FEP) for proton exchange membrane fuel cell (PEMFC). *International Journal of Precision Engineering and Manufacturing* 2012;13:1145–51. doi:10.1007/s12541-012-0152-x.
- [44] Öztürk A, Fıçıcılar B, Eroğlu İ, Bayrakçeken Yurtcan A. Facilitation of water management in low Pt loaded PEM fuel cell by creating hydrophobic microporous layer with PTFE, FEP and PDMS polymers: Effect of polymer and carbon amounts. *International Journal of Hydrogen Energy* 2017;42:21226–49. doi:10.1016/j.ijhydene.2017.06.202.
- [45] Latorrata S, Balzarotti R, Gallo Stampino P, Cristiani C, Dotelli G, Guilizzoni M. Design of properties and performances of innovative gas diffusion media for polymer electrolyte membrane fuel cells. *Progress in Organic Coatings* 2015;78:517–25. doi:10.1016/j.porgcoat.2014.05.028.
- [46] Gola M, Sansotera M, Navarrini W, Bianchi CL, Gallo Stampino P, Latorrata S, Dotelli G. Perfluoropolyether-functionalized gas diffusion layers for proton exchange membrane fuel cells. *Journal of Power Sources* 2014;258:351–5. doi:10.1016/j.jpowsour.2014.02.025.
- [47] Rofaiel A, Ellis JS, Challa PR, Bazylak A. Heterogeneous through-plane distributions of polytetrafluoroethylene in polymer electrolyte membrane fuel cell gas diffusion layers. *Journal of Power Sources* 2012;201:219–25. doi:10.1016/j.jpowsour.2011.11.005.
- [48] Mathias M, Roth J, Fleming J LW. Diffusion media materials and characterization. *Handbook of Fuel Cells-Fundamentals, Technology and Applications*, Edited by Wolf Vielstich, Hubert A. Gasteiger, Arnold Lamm. Volume 3: Fuel Cell Technology and Applications. John Wiley & Sons, Ltd, 2003.
- [49] Liu X, Guo H, Ye F, Ma CF. Water flooding and pressure drop characteristics in flow channels of proton exchange membrane fuel cells. *Electrochimica Acta* 2007;52:3607–14. doi:10.1016/j.electacta.2006.10.030.
- [50] Li H, Tang Y, Wang Z, Shi Z, Wu S, Song D, Zhang J, Fatih K, Zhang J, Wang H, Liu Z, Abouatallah R, Mazza A. A review of water flooding issues in the proton exchange membrane fuel cell. *Journal of Power Sources* 2008;178:103–17. doi:10.1016/j.jpowsour.2007.12.068.

- [51] Ozden A, Shahgaldi S, Zhao J, Li X, Hamdullahpur F. Assessment of graphene as an alternative microporous layer material for proton exchange membrane fuel cells. *Fuel* 2018;215:726–34. doi:10.1016/j.fuel.2017.11.109.
- [52] Zamel N, Becker J, Wiegmann A. Estimating the thermal conductivity and diffusion coefficient of the microporous layer of polymer electrolyte membrane fuel cells. *Journal of Power Sources* 2012;207:70–80. doi:10.1016/j.jpowsour.2012.02.003.
- [53] Pasaogullari U, Wang CY. Two-phase transport and the role of microporous layer in polymer electrolyte fuel cells. *Electrochimica Acta* 2004;49:4359–69. doi:10.1016/j.electacta.2004.04.027.
- [54] Ferreira RB, Falcão DS, Oliveira VB, Pinto A. MFR. Experimental study on the membrane electrode assembly of a proton exchange membrane fuel cell: effects of microporous layer, membrane thickness and gas diffusion layer hydrophobic treatment. *Electrochimica Acta* 2017;224:337–45. doi:http://dx.doi.org/10.1016/j.electacta.2016.12.074.
- [55] Kim T, Lee S, Park H. A study of water transport as a function of the micro-porous layer arrangement in PEMFCs. *International Journal of Hydrogen Energy* 2010;35:8631–43. doi:10.1016/j.ijhydene.2010.05.123.
- [56] Chun JH, Park KT, Jo DH, Kim SG, Kim SH. Numerical modeling and experimental study of the influence of GDL properties on performance in a PEMFC. *International Journal of Hydrogen Energy* 2011;36:1837–45. doi:10.1016/j.ijhydene.2010.01.036.
- [57] Chen HH, Chang MH. Effect of cathode microporous layer composition on proton exchange membrane fuel cell performance under different air inlet relative humidity. *Journal of Power Sources* 2013;232:306–9. doi:10.1016/j.jpowsour.2013.01.079.
- [58] El-Kharouf A, Mason TJ, Brett DJL, Pollet BG. Ex-situ characterisation of gas diffusion layers for proton exchange membrane fuel cells. *Journal of Power Sources* 2012;218:393–404. doi:10.1016/j.jpowsour.2012.06.099.
- [59] Yan W-M, Wu D-K, Wang X-D, Ong A-L, Lee D-J, Su A. Optimal microporous layer for proton exchange membrane fuel cell. *Journal of Power Sources* 2010;195:5731–4. doi:10.1016/j.jpowsour.2010.03.041.

- [60] Lobato J, Cañizares P, Rodrigo M A, Úbeda D, Pinar FJ, Linares JJ. Optimisation of the microporous layer for a polybenzimidazole-based high temperature pemfc - Effect of carbon content. *Fuel Cells* 2010;10:770–7. doi:10.1002/face.200900175.
- [61] Gharibi H, Javaheri M, Mirzaie RA. The synergy between multi-wall carbon nanotubes and Vulcan XC72R in microporous layers. *International Journal of Hydrogen Energy* 2010;35:9241–51. doi:10.1016/j.ijhydene.2009.08.092.
- [62] Owejan JP, Owejan JE, Gu W, Trabold T A, Tighe TW, Mathias MF. Water Transport Mechanisms in PEMFC Gas Diffusion Layers. *Journal of The Electrochemical Society* 2010;157:B1456. doi:10.1149/1.3468615.
- [63] Jung G-B, Tzeng W-J, Jao T-C, Liu Y-H, Yeh C-C. Investigation of porous carbon and carbon nanotube layer for proton exchange membrane fuel cells. *Applied Energy* 2013;101:457–64. doi:10.1016/j.apenergy.2012.08.045.
- [64] Orogbemi OM, Ingham DB, Ismail MS, Hughes KJ, Ma L, Pourkashanian M. Through-plane gas permeability of gas diffusion layers and microporous layer: Effects of carbon loading and sintering. *Journal of The Energy Institute* 2016. doi:10.1016/j.joei.2016.11.008.
- [65] Abdelkareem MA, Tsujiguchi T, Nakagawa N. Effect of black catalyst ionomer content on the performance of passive DMFC. *Journal of Power Sources* 2010;195:6287–93. doi:10.1016/j.jpowsour.2010.04.070.
- [66] Hunsom M, Piumsomboon P, Pruksathorn K, Tantavichet N, Endoo S, Charutavai K, Poochinda K. Novel application of Hicon Black in PEMFC microporous sublayer: Effects of composition and subsequent membrane selection. *Renewable Energy* 2011;36:369–73. doi:10.1016/j.renene.2010.07.002.
- [67] Kitahara T, Nakajima H, Inamoto M, Shinto K. Triple microporous layer coated gas diffusion layer for performance enhancement of polymer electrolyte fuel cells under both low and high humidity conditions. *Journal of Power Sources* 2014;248:1256–63. doi:10.1016/j.jpowsour.2013.10.066.
- [68] Oh H, Park J, Min K, Lee E, Jyoung JY. Effects of pore size gradient in the substrate of a gas diffusion layer on the performance of a proton

- exchange membrane fuel cell. *Applied Energy* 2015;149:186–93. doi:10.1016/j.apenergy.2015.03.072.
- [69] Ca P, Plaza J, Andr M. Microporous layer based on SiC for high temperature proton exchange membrane fuel cells. *Journal of Power* 2015;288:288–95. doi:10.1016/j.jpowsour.2015.04.102.
- [70] Park S, Shao Y, Wan H, Rieke PC, Viswanathan V V., Towne SA, Saraf LV, Liu J, Lin Y, Wang Y. Design of graphene sheets-supported Pt catalyst layer in PEM fuel cells. *Electrochemistry Communications* 2011;13:258–61. doi:10.1016/j.elecom.2010.12.028.
- [71] Zhou SY, Gweon G-H, Fedorov AV, First PN, de Heer WA, Lee D-H, Guinea F, CastroNeto AH, Lanzara A. Substrate-induced bandgap opening in epitaxial graphene. *Nature Materials* 2007;6:916–916. doi:10.1038/nmat2056.
- [72] Najafabadi AT, Leeuwner MJ, Wilkinson DP, Gyenge EL. Electrochemically Produced Graphene for Microporous Layers in Fuel Cells. *ChemSusChem* 2016;9:1689–97. doi:10.1002/cssc.201600351.
- [73] Novoselov KS, Fal'ko VI, Colombo L, Gellert PR, Schwab MG, Kim K. A roadmap for graphene. *Nature* 2012;490:192–200. doi:10.1038/nature11458.
- [74] A.K. Geim, K.S. Novoselov. The rise of graphene. *Nature Materials* 2015;149:183–91.
- [75] Marinkas A, Arena F, Mitzel J, Prinz GM, Heinzl A, Peinecke V, Natter H. Graphene as catalyst support: The influences of carbon additives and catalyst preparation methods on the performance of PEM fuel cells. *Carbon* 2013;58:139–50. doi:10.1016/j.carbon.2013.02.043.
- [76] Mu S, Chen X, Sun R, Liu X, Wu H, He D, Cheng K. Nano-size boron carbide intercalated graphene as high performance catalyst supports and electrodes for PEM fuel cells. *Carbon* 2016;103:449–56. doi:10.1016/j.carbon.2016.03.044.
- [77] Xu JB, Zhao TS. Mesoporous carbon with uniquely combined electrochemical and mass transport characteristics for polymer electrolyte membrane fuel cells. *RSC Advances* 2013;3:16–24. doi:10.1039/C2RA22279E.

- [78] Dai W, Wang H, Yuan X-Z, Martin JJ, Yang D, Qiao J, Ma J. A review on water balance in the membrane electrode assembly of proton exchange membrane fuel cells. *International Journal of Hydrogen Energy* 2009;34:9461–78. doi:10.1016/j.ijhydene.2009.09.017.
- [79] Nam JH, Lee KJ, Hwang GS, Kim CJ, Kaviany M. Microporous layer for water morphology control in PEMFC. *International Journal of Heat Mass Transfer* 2009;52:2779–91. doi:10.1016/j.ijheatmasstransfer.2009.01.002.
- [80] Lee J, Hinebaugh J, Bazylak A. Synchrotron X-ray radiographic investigations of liquid water transport behavior in a PEMFC with MPL-coated GDLs. *Journal of Power Sources* 2013;227:123–30. doi:10.1016/j.jpowsour.2012.11.006.
- [81] Mason TJ, Millichamp J, Neville TP, El-Kharouf A, Pollet BG, Brett DJL. Effect of clamping pressure on ohmic resistance and compression of gas diffusion layers for polymer electrolyte fuel cells. *Journal of Power Sources* 2012;219:52–9. doi:10.1016/j.jpowsour.2012.07.021.
- [82] Netwall CJ, Gould BD, Rodgers JA, Nasello NJ, Swider-Lyons KE. Decreasing contact resistance in proton-exchange membrane fuel cells with metal bipolar plates. *Journal of Power Sources* 2013;227:137–44. doi:10.1016/j.jpowsour.2012.11.012.
- [83] Arvay A, Yli-Rantala E, Liu CH, Peng XH, Koski P, Cindrella L, Kauranen P, Wilde PM, Kannan AM. Characterization techniques for gas diffusion layers for proton exchange membrane fuel cells - A review. *Journal of Power Sources* 2012;213:317–37. doi:10.1016/j.jpowsour.2012.04.026.
- [84] Nam J, Chippar P, Kim W, Ju H. Numerical analysis of gas crossover effects in polymer electrolyte fuel cells (PEFCs). *Applied Energy* 2010;87:3699–709. doi:10.1016/j.apenergy.2010.05.023.
- [85] Perng SW, Wu HW. Non-isothermal transport phenomenon and cell performance of a cathodic PEM fuel cell with a baffle plate in a tapered channel. *Applied Energy* 2011;88:52–67. doi:10.1016/j.apenergy.2010.07.006.
- [86] Perng SW, Wu HW. Effect of the prominent catalyst layer surface on reactant gas transport and cell performance at the cathodic side of a

- PEMFC. *Applied Energy* 2010;87:1386–99. doi:10.1016/j.apenergy.2009.08.006.
- [87] Ismail MS, Damjanovic T, Ingham DB, Pourkashanian M, Westwood A. Effect of polytetrafluoroethylene-treatment and microporous layer-coating on the electrical conductivity of gas diffusion layers used in proton exchange membrane fuel cells. *Journal of Power Sources* 2010;195:2700–8. doi:10.1016/j.jpowsour.2009.11.069.
- [88] Ismail MS, Borman D, Damjanovic T, Ingham DB, Pourkashanian M. On the through-plane permeability of microporous layer-coated gas diffusion layers used in proton exchange membrane fuel cells. *Int J Hydrogen Energy* 2011;36:10392–402. doi:10.1016/j.ijhydene.2010.09.012.
- [89] Ismail MS, Hughes KJ, Ingham DB, Ma L, Pourkashanian M. Effects of anisotropic permeability and electrical conductivity of gas diffusion layers on the performance of proton exchange membrane fuel cells. *Applied Energy* 2012;95:50–63. doi:10.1016/j.apenergy.2012.02.003.
- [90] Kleemann J, Finsterwalder F, Tillmetz W. Characterisation of mechanical behaviour and coupled electrical properties of polymer electrolyte membrane fuel cell gas diffusion layers. *Journal of Power Sources* 2009;190:92–102. doi:10.1016/j.jpowsour.2008.09.026.
- [91] Chang WR, Hwang JJ, Weng FB, Chan SH. Effect of clamping pressure on the performance of a PEM fuel cell. *Journal of Power Sources* 2007;166:149–54. doi:10.1016/j.jpowsour.2007.01.015.
- [92] Cindrella L, Kannan AM, Lin JF, Saminathan K, Ho Y, Lin CW, Wertz J. Gas diffusion layer for proton exchange membrane fuel cells-A review. *Journal of Power Sources* 2009;194:146–60. doi:10.1016/j.jpowsour.2009.04.005.
- [93] Ahmed DH, Sung HJ, Bae J. Effect of GDL permeability on water and thermal management in PEMFCs-II. Clamping force. *International Journal of Hydrogen Energy* 2008;33:3786–800. doi:10.1016/j.ijhydene.2008.04.023.
- [94] Parry V, Appert E, Joud JC. Characterisation of wettability in gas diffusion layer in proton exchange membrane fuel cells. *Applied Surface Science* 2010;256:2474–8. doi:10.1016/j.apsusc.2009.10.091.

- [95] Antonacci P, Chevalier S, Lee J, Ge N, Hinebaugh J, Yip R, Tabuchi Y, Kotaka T, Bazylak A. Balancing mass transport resistance and membrane resistance when tailoring microporous layer thickness for polymer electrolyte membrane fuel cells operating at high current densities. *Electrochimica Acta* 2016;188:888–97. doi:10.1016/j.electacta.2015.11.115.
- [96] Das PK, Li X, Liu Z-S. Analysis of liquid water transport in cathode catalyst layer of PEM fuel cells. *International Journal of Hydrogen Energy* 2010;35:2403–16. doi:10.1016/j.ijhydene.2009.12.160.
- [97] Jiao K, Li X. Effect of surface dynamic wettability in proton exchange membrane fuel cells. *International Journal of Hydrogen Energy* 2010;35:9095–103. doi:10.1016/j.ijhydene.2010.05.027.
- [98] Wang Y, Al Shakhshir S, Li X. Development and impact of sandwich wettability structure for gas distribution media on PEM fuel cell performance. *Applied Energy* 2011;88:2168–75. doi:10.1016/j.apenergy.2010.12.054.
- [99] Furmidge CGL. Studies at phase interfaces. I. The sliding of liquid drops on solid surfaces and a theory for spray retention. *Journal of Colloid Science* 1962;17:309–24. doi:10.1016/0095-8522(62)90011-9.
- [100] Guo ZG, Liu WM. Sticky superhydrophobic surface. *Applied Physics Letters* 2007;90. doi:10.1063/1.2745251.
- [101] Gurau V, Bluemle MJ, De Castro ES, Tsou Y-M, Mann Jr JA, Zawodzinski Jr TA. Characterization of transport properties in gas diffusion layers for proton exchange membrane fuel cells: 1. Wettability (internal contact angle to water and surface energy of GDL fibers). *Journal of Power Sources* 2006;160:1156–62. doi:http://dx.doi.org/10.1016/j.jpowsour.2006.03.016.
- [102] Kitahara T, Konomi T, Nakajima H. Microporous layer coated gas diffusion layers for enhanced performance of polymer electrolyte fuel cells. *Journal of Power Sources* 2010;195:2202–11. doi:10.1016/j.jpowsour.2009.10.089.
- [103] Tamayol A, Bahrami M. In-plane gas permeability of proton exchange membrane fuel cell gas diffusion layers. *Journal of Power Sources* 2011;196:3559–64. doi:10.1016/j.jpowsour.2010.11.109.

- [104] Tamayol A, McGregor F, Bahrami M. Single phase through-plane permeability of carbon paper gas diffusion layers. *Journal of Power Sources* 2012;204:94–9. doi:10.1016/j.jpowsour.2011.11.084.
- [105] Morgan JM, Datta R. Understanding the gas diffusion layer in proton exchange membrane fuel cells. I. How its structural characteristics affect diffusion and performance. *Journal of Power Sources* 2014;251:269–78. doi:10.1016/j.jpowsour.2013.09.090.
- [106] Fishman Z, Bazylak A. Heterogeneous Through-Plane Porosity Distributions for Treated PEMFC GDLs. II. Effect of MPL Cracks. *Journal of The Electrochemical Society* 2011;158:B846. doi:10.1149/1.3594636.
- [107] Kandlikar SG, Garofalo ML, Lu Z. Water management in a PEMFC: Water transport mechanism and material degradation in gas diffusion layers. *Fuel Cells* 2011;11:814–23. doi:10.1002/fuce.201000172.
- [108] Chun JH, Park KT, Jo DH, Lee JY, Kim SG, Park SH, Lee ES, Jyoung Jy-Y, Kim SH. Development of a novel hydrophobic/hydrophilic double micro porous layer for use in a cathode gas diffusion layer in PEMFC. *International Journal of Hydrogen Energy* 2011;36:8422–8. doi:10.1016/j.ijhydene.2011.04.038.
- [109] Orogbemi OM, Ingham DB, Ismail MS, Hughes KJ, Ma L, Pourkashanian M. The effects of the composition of microporous layers on the permeability of gas diffusion layers used in polymer electrolyte fuel cells. *International Journal of Hydrogen Energy* 2016;41:21345–51. doi:10.1016/j.ijhydene.2016.09.160.
- [110] Oono Y, Sounai A, Hori M. Influence of the phosphoric acid-doping level in a polybenzimidazole membrane on the cell performance of high-temperature proton exchange membrane fuel cells. *Journal of Power Sources* 2009;189:943–9. doi:10.1016/j.jpowsour.2008.12.115.
- [111] Passalacqua E, Squadrito G, Lufrano F, Patti A, Giorgi L. Effects of the diffusion layer characteristics on the performance of polymer electrolyte fuel cell electrodes. *Journal of Applied Electrochemistry* 2001;31:449–54. doi:10.1023/A:1017547112282.
- [112] Wu R, Zhu X, Liao Q, Wang H, Ding YD, Li J, Ye Ding-ding. A pore network study on water distribution in bi-layer gas diffusion media: Effects of inlet boundary condition and micro-porous layer properties.

- International Journal of Hydrogen Energy 2010;35:9134–43. doi:10.1016/j.ijhydene.2010.06.051.
- [113] Chang HM, Lin CW, Chang MH, Shiu HR, Chang WC, Tsau FH. Optimization of polytetrafluoroethylene content in cathode gas diffusion layer by the evaluation of compression effect on the performance of a proton exchange membrane fuel cell. *Journal of Power Sources* 2011;196:3773–80. doi:10.1016/j.jpowsour.2010.12.090.
- [114] Pasaogullari U, Wang CY. Liquid Water Transport in Gas Diffusion Layer of Polymer Electrolyte Fuel Cells. *Journal of the Electrochemical Society* 2004;151:A399. doi:10.1149/1.1646148.
- [115] Su H, Sita C, Pasupathi S. The Effect of Gas Diffusion Layer PTFE Content on The Performance of High Temperature Proton Exchange Membrane Fuel Cell. *International Journal of Electrochemical Science* 2016;11:2919–26. doi:10.20964/110402919.
- [116] Van Nguyen T, Ahosseini A, Wang X, Yarlagadda V, Kwong A, Weber AZ, Deevanhxay P, Tsushima S, Hirai S. Hydrophobic Gas-Diffusion Media for Polymer-Electrolyte Fuel Cells by Direct Fluorination. *Journal of The Electrochemical Society* 2015;162:F1451–60. doi:10.1149/2.0411514jes.
- [117] Tang H, Wang S, Pan M, Yuan R. Porosity-graded micro-porous layers for polymer electrolyte membrane fuel cells. *Journal of Power Sources* 2007;166:41–6. doi:10.1016/j.jpowsour.2007.01.021.
- [118] Chun JH, Park KT, Jo DH, Lee JY, Kim SG, Lee ES, Jyoung Jy-Young, Kim SH. Determination of the pore size distribution of micro porous layer in PEMFC using pore forming agents under various drying conditions. *International Journal of Hydrogen Energy* 2010;35:11148–53. doi:10.1016/j.ijhydene.2010.07.056.
- [119] Velayutham G, Kaushik J, Rajalakshmi N, Dhathathreyan KS. Effect of PTFE Content in Gas Diffusion Media and Microlayer on the Performance of PEMFC Tested under Ambient Pressure. *Fuel Cells* 2007:314–8. doi:10.1002/fuce.200600032.
- [120] Gostick JT, Ioannidis MA, Fowler MW, Pritzker MD. Direct measurement of the capillary pressure characteristics of water-air-gas diffusion layer systems for PEM fuel cells. *Electrochemistry Communications* 2008;10:1520–3. doi:10.1016/j.elecom.2008.08.008.

- [121] Harkness IR, Hussain N, Smith L, Sharman JDB. The use of a novel water porosimeter to predict the water handling behaviour of gas diffusion media used in polymer electrolyte fuel cells. *Journal of Power Sources* 2009;193:122–9. doi:10.1016/j.jpowsour.2008.11.055.
- [122] Mathur RB, Maheshwari PH, Dhama TL, Tandon RP. Characteristics of the carbon paper heat-treated to different temperatures and its influence on the performance of PEM fuel cell. *Electrochimica Acta* 2007;52:4809–17. doi:10.1016/j.electacta.2007.01.041.
- [123] Senthil Velan V, Velayutham G, Rajalakshmi N, Dhathathreyan KS. Influence of compressive stress on the pore structure of carbon cloth based gas diffusion layer investigated by capillary flow porometry. *International Journal of Hydrogen Energy* 2014;39:1752–9. doi:10.1016/j.ijhydene.2013.11.038.
- [124] Fairweather JD, Cheung P, St-Pierre J, Schwartz DT. A microfluidic approach for measuring capillary pressure in PEMFC gas diffusion layers. *Electrochemistry Communications* 2007;9:2340–5. doi:10.1016/j.elecom.2007.06.042.
- [125] Litster S, Sinton D, Djilali N. Ex situ visualization of liquid water transport in PEM fuel cell gas diffusion layers. *Journal of Power Sources* 2006;154:95–105. doi:10.1016/j.jpowsour.2005.03.199.
- [126] Williams M V., Begg E, Bonville L, Kunz HR, Fenton JM. Characterization of Gas Diffusion Layers for PEMFC. *Journal of the Electrochemical Society* 2004;151:A1173. doi:10.1149/1.1764779.
- [127] Jena A, Gupta K. Advances in pore structure evaluation by porometry. *Chemical Engineering Technology* 2010;33:1241–50. doi:10.1002/ceat.201000119.
- [128] Smits FM. Measurement of Sheet Resistivity Sheet Resistivities with the Four-Point Probe. *Bell System Technology Journal* 1958:711–8.
- [129] PEM Fuel Cells: theory and practice, 2nd Edition, Elsevier, Waltham, MA, 2012.
- [130] Wilde PM, Mändle M, Murata M, Berg N. Structural and physical properties of GDL and GDL/BPP combinations and their influence on PEMFC performance. *Fuel Cells* 2004;4:180–4. doi:10.1002/fuce.200400022.

- [131] Gostick JT, Fowler MW, Pritzker MD, Ioannidis MA, Behra LM. In-plane and through-plane gas permeability of carbon fiber electrode backing layers. *Journal of Power Sources* 2006;162:228–38. doi:10.1016/j.jpowsour.2006.06.096.
- [132] Zhao J, Shahgaldi S, Alaefour I, Xu Q, Li X. Gas permeability of catalyzed electrodes in polymer electrolyte membrane fuel cells. *Applied Energy* 2018;209:203–10. doi:10.1016/j.apenergy.2017.10.087.
- [133] Christoph R, Siegenthaler H. In situ. *Situ* 2010;33:433–46. doi:10.1038/nm.2294.
- [134] Shahgaldi S, Alaefour I, Unsworth G, Li X. Development of a low temperature decal transfer method for the fabrication of proton exchange membrane fuel cells. *International Journal of Hydrogen Energy* 2017;42:11813–22. doi:10.1016/j.ijhydene.2017.02.127.
- [135] Dubau L, Castanheira L, Berthomé G, Maillard F. An identical-location transmission electron microscopy study on the degradation of Pt/C nanoparticles under oxidizing, reducing and neutral atmosphere. *Electrochimica Acta* 2013;110:273–81. doi:10.1016/j.electacta.2013.03.184.
- [136] Song S, Wang Y, Shen PK. Pulse-microwave assisted polyol synthesis of highly dispersed high loading Pt/C electrocatalyst for oxygen reduction reaction. *Journal of Power Sources* 2007;170:46–9. doi:10.1016/j.jpowsour.2007.04.012.
- [137] You DJ, Kwon K, Joo SH, Kim JH, Kim JM, Pak C, Chang H. Carbon-supported ultra-high loading Pt nanoparticle catalyst by controlled overgrowth of Pt: Improvement of Pt utilization leads to enhanced direct methanol fuel cell performance. *International Journal of Hydrogen Energy* 2012;37:6880–5. doi:10.1016/j.ijhydene.2012.01.103.
- [138] Liang H, Su H, Pollet BG, Linkov V, Pasupathi S. Membrane electrode assembly with enhanced platinum utilization for high temperature proton exchange membrane fuel cell prepared by catalyst coating membrane method. *Journal of Power Sources* 2014;266:107–13. doi:10.1016/j.jpowsour.2014.05.014.
- [139] Han M, Xu JH, Chan SH, Jiang SP. Characterization of gas diffusion layers for PEMFC. *Electrochimica Acta* 2008;53:5361–7. doi:10.1016/j.electacta.2008.02.057.

- [140] Eslamian M, Ahmed M, El-Dosoky MF, Saghir MZ. Effect of thermophoresis on natural convection in a Rayleigh-Benard cell filled with a nanofluid. *International Journal of Heat and Mass Transfer* 2015;81:142–56. doi:10.1016/j.ijheatmasstransfer.2014.10.001.
- [141] Rouquerol J, Avnir D, Fairbridge CW, Everett DH., Haynes JH, Pernicone N, Ramsay JDF, Sing KSW, Unger KK. Recommendations for the characterization of porous solids. *Pure Applied Chemistry* 1994;66:1739–58.
- [142] Zdravkov BD, Čermák JJ, Šefara M, Janků J. Pore classification in the characterization of porous materials: A perspective. *Central European Journal of Chemistry* 2007;5:385–95. doi:10.2478/s11532-007-0017-9.
- [143] Park J, Oh H, Il Y, Min K, Lee E, Jyoung J. Effect of the pore size variation in the substrate of the gas diffusion layer on water management and fuel cell performance. *Applied Energy* 2016;171:200–12. doi:10.1016/j.apenergy.2016.02.132.
- [144] Cho SM, Yom JH, Hwang SW, Seong IW, Kim J, Cho SH, Yoon WY. Morphology control of lithium peroxide using Pd₃Co as an additive in aprotic Li-O₂ batteries. *Journal of Power Sources* 2017;342:427–34. doi:10.1016/j.jpowsour.2016.12.076.
- [145] Stankovich S, Dikin DA, Piner RD, Kohlhaas KA, Kleinhammes A, Jia Y, Wu Y, Nguyen ST, Ruoff RS. Synthesis of graphene-based nanosheets via chemical reduction of exfoliated graphite oxide. *Carbon* 2007;45:1558–65. doi:10.1016/j.carbon.2007.02.034.
- [146] Wang X, Zhang H, Zhang J, Xu H, Zhu X, Chen J, Yi B. A bi-functional micro-porous layer with composite carbon black for PEM fuel cells. *Journal of Power Sources* 2006;162:474–9. doi:10.1016/j.jpowsour.2006.06.064.
- [147] Marinho B, Ghislandi M, Tkalya E, Koning CE, de With G. Electrical conductivity of compacts of graphene, multi-wall carbon nanotubes, carbon black, and graphite powder. *Powder Technology* 2012;221:351–8. doi:10.1016/j.powtec.2012.01.024.
- [148] Tavakoli B, Roshandel R. The effect of fuel cell operational conditions on the water content distribution in the polymer electrolyte membrane. *Renewable Energy* 2011;36:3319–31. doi:10.1016/j.renene.2011.05.003.

- [149] Lee J, Chevalier S, Banerjee R, Antonacci P, Ge N, Yip R, Kotaka T, Tabuchi Y, Bazylak A. Investigating the effects of gas diffusion layer substrate thickness on polymer electrolyte membrane fuel cell performance via synchrotron X-ray radiography. *Electrochimica Acta* 2017;236:161–70. doi:10.1016/j.electacta.2017.03.162.
- [150] Tiss F, Chouikh R, Guizani A. A numerical investigation of the effects of membrane swelling in polymer electrolyte fuel cells. *Energy Conversion and Management* 2013;67:318–24. doi:10.1016/j.enconman.2012.12.006.
- [151] Zhang J, Song C, Zhang J, Baker R, Zhang L. Understanding the effects of backpressure on PEM fuel cell reactions and performance. *Journal of Electroanalytical Chemistry* 2013;688:130–6. doi:10.1016/j.jelechem.2012.09.033.
- [152] Su A, Ferng YM, Shih JC. CFD investigating the effects of different operating conditions on the performance and the characteristics of a high-temperature PEMFC. *Energy* 2010;35:16–27. doi:10.1016/j.energy.2009.08.033.